Alma Mater Studiorum – Università di Bologna

Dipartimento di Fisica e Astronomia
Corso di Laurea magistrale in Astrofisica e Cosmologia

Image simulations of highly magnified clumpy galaxies

Tesi di Laurea Magistrale

Presentata da:
Irene Mini

Relatore:
Chiar.mo Prof. **Lauro Moscardini**
Correlatori:
Dott. **Massimo Meneghetti**
Dott. **Pietro Bergamini**

Anno accademico **2021/2022**

Abstract

Strong gravitational lensing is a fundamental tool for studying the high-redshift Universe since the magnification it produces enables it to reach spatial resolutions that would otherwise be unattainable. Background sources placed in proximity to the caustics of a galaxy cluster lead to such a high degree of magnification, that they allow for the observation of regions as small as stellar clusters. This is a crucial process to comprehend the mechanisms responsible for galaxy formation and evolution in the early Universe.

In this Thesis, we develop a python-based pipeline aimed at simulating observations of high-redshift clumpy galaxies with three different instruments: HST/ACS, JWST/NIRCAM and Euclid/VIS. These sources are modeled by combining the host galaxy and stellar clumps as multiple luminous components. Each of them is defined using elliptical Sérsic surface brightness profiles. We place these sources near the caustics of five different galaxy clusters in order to generate highly magnified gravitational arcs.

This tool is highly flexible, allowing us to change the parameters in order to simulate very diverse sources under different observing conditions. Our simulator, hence, enables us to directly compare the performance of past, present, and future instruments when dealing with sub-kpc substructures.

The second part of this work shows two applications of our simulator. Firstly, we focus on the issue of identifying stellar clumps in strongly lensed galaxies. In order to complete this task we rely on the recently developed modeling code `GravityFM`. We define a procedure to increase the contrast of the visible stellar clumps in images simulated with the abovementioned instruments and we attempt a statistical comparison of the detections. Secondly, we show how the images generated with our pipeline can be combined with other simulators, such as `SimCADO` image simulator for E-ELT/MICADO, which also includes the support from the Adaptive Optics system MORFEO.

Sommario

Il lensing gravitazionale forte è uno strumento fondamentale per studiare l'Universo ad alto redshift, in quanto l'amplificazione che esso produce consente di raggiungere risoluzioni spaziali altrimenti irraggiungibili. Le sorgenti di background che si trovano in prossimità delle caustiche di un ammasso di galassie subiscono un così alto livello di amplificazione da consentire l'osservazione persino di oggetti con dimensioni tipiche degli ammassi stellari. Rivelare oggetti di questo tipo è di cruciale importanza, in quanto aiuta a fare chiarezza sui meccanismi responsabili della formazione ed evoluzione delle galassie primordiali.

In questa Tesi, realizziamo un software, scritto in Python, volto a simulare osservazioni di galassie ad alto redshift ricche di clumps stellari, ricorrendo a tre diversi strumenti: HST/ACS, JWST/NIRCAM e Euclid/VIS. Queste sorgenti vengono modellizzate combinando assieme la galassia ospite e i clumps stellari, trattandoli come componenti luminosi distinti, dove ogni oggetto è definito tramite un profilo di brillanza superficiale di Sérsic. Le sorgenti vengono, poi, posizionate in prossimità delle caustiche di ben cinque ammassi differenti, così da produrre archi gravitazionali fortemente amplificati.

Questo software è, inoltre, altamente flessibile, in quanto è possibile variare i parametri che caratterizzano la simulazione in modo tale da simulare differenti tipi di sorgenti in condizioni altamente diversificate. Il nostro simulatore consente, quindi, di confrontare in modo diretto la performance di vari strumenti, sia passati, che presenti, che futuri, quando questi si trovano ad osservare strutture con lunghezze scala sub-kpc.

La seconda parte di questo lavoro mostra, come esempi, due possibili applicazioni del nostro software. In primo luogo, affrontiamo il problema di come identificare i clumps stellari in sorgenti fortemente amplificate. A tale scopo, sfruttiamo il recente codice di forward modeling `GravityFM`, grazie al quale definiamo una procedura per aumentare la visibilità dei clumps nelle immagini simulate con i tre telescopi sopracitati, per poi effettuare un'analisi statistica delle detection. In secondo luogo, mostriamo come le immagini generate con il nostro simulatore possano essere combinate con altri software, come `SimCADO`, che in particolare simula osservazioni condotte con E-ELT/MICADO in combinazione con il sistema di Ottica Adattiva MORFEO.

Contents

Chapter 1

Gravitational Lensing

According to Einstein's Theory of Relativity, masses producing a gravitational field can shape the geometry of space-time and, hence, deflect light rays (37). The deflection of light by massive bodies is referred to as *Gravitational Lensing*. A gravitational lens occurs when a mass distribution is large enough to deflect and magnify the light from a source located in its background. This makes Gravitational Lensing a compelling tool to study the distribution of matter in the Universe, allowing us to reach its deepest and darkest components.

1.1 Deflection of light

In order to study the deflection of light, we make some assumptions: we consider only time-scales and regions where the expansion of the Universe is not significant and a weak-field limit, which is furthermore a realistic requirement, as in the majority of astrophysical scenarios lenses are characterized by a small gravitational potential, namely $\Phi \ll c^2$. Then, we assume the perturbed region is described in terms of an effective refractive index, whose expression can be found through the Minkowski metric as

$$n = \frac{c}{c'} \sim 1 - \frac{2\phi}{c^2}, \tag{1.1.1}$$

where c' is the photon effective speed in the gravitational field. Using the Fermat's principle and integrating over the unperturbed light path, we finally obtain that the deflection angle is determined by the component of the gradient of Φ perpendicular to the photon propagation direction:

$$\vec{\alpha} = \frac{2}{c^2} \int_{-\infty}^{+\infty} \vec{\nabla}_{\perp} \Phi dz. \tag{1.1.2}$$

A more realistic situation with a three-dimensional distribution of matter leads to a more complex expression, in which a two-dimensional vector $\vec{\xi}$ appears. It describes the separation between the ray and the optical axis on the lens plane (Figure 1.1):

$$\vec{\alpha}(\vec{\xi}) = \frac{4G}{c^2} \int \frac{(\vec{\xi} - \vec{\xi'})\Sigma(\vec{\xi'})}{\mid \vec{\xi} - \vec{\xi'} \mid^2} d^2\xi', \tag{1.1.3}$$

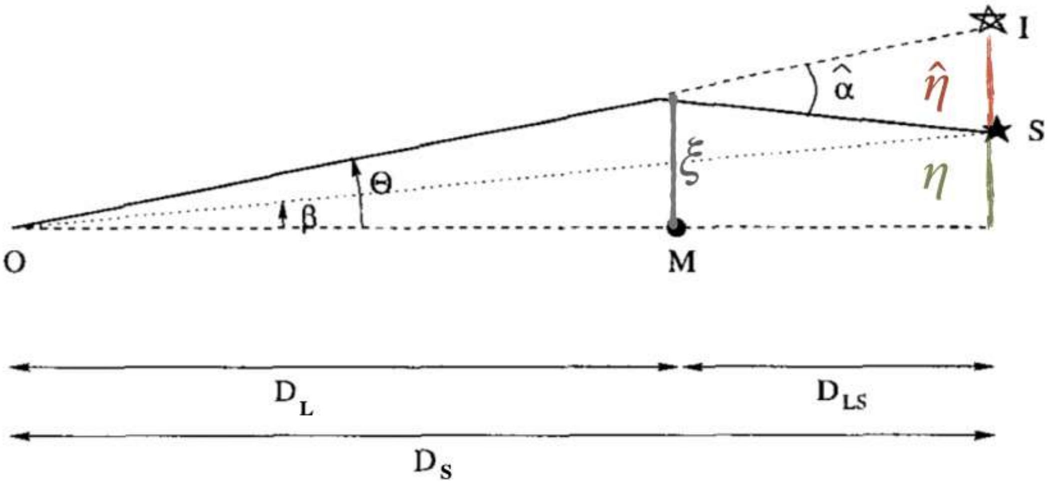

Figure 1.1: Lensed system geometry.

where we have applied the so-called thin screen approximation and assumed the deflection occurs in the lens plane. In fact, a typical lensing system includes a three-dimensional source and lens, but since the sizes of lenses and sources are much smaller than the distances involved in any gravitational lensing effect, these three dimensional objects can be replaced by the planar mass and light distributions. Hence, a three-dimensional mass distribution becomes two-dimensional: $\Sigma(\overrightarrow{\xi}) = \int \rho(\overrightarrow{\xi}, z)dz$, where $\Sigma(\overrightarrow{\xi})$ and $\rho(\overrightarrow{\xi}, z)$ are the surface and volumetric densities.

1.2 Lens Equation

We should imagine a simplistic situation like the one represented in Figure 1.1, where we can identify the observer, the source plane, and the lens plane. It is important to notice that the light propagating from the source S to the observer O goes through three distinct regions: in the first one, light crosses an unperturbed spacetime, travelling from the source to a point close to the lens L; then, near the lens, the light is deflected by an angle $\overrightarrow{\hat{\alpha}}$; finally light travels again through an unperturbed spacetime.

The lens equation allows to establish a relation between the intrinsic source position ($\overrightarrow{\beta}$) and the apparent one ($\overrightarrow{\theta}$), also known as image position. Referring to Figure 1.1, we obtain

$$D_S \overrightarrow{\theta} = D_S \overrightarrow{\beta} + D_{LS} \overrightarrow{\hat{\alpha}}(\overrightarrow{\theta}), \tag{1.2.1}$$

where D_S is the angular diameter distance between the source and the observer, D_L the angular diameter distance between the lens and the observer and D_{LS} the angular diameter distance between the lens and the source. The vector $\overrightarrow{\hat{\alpha}}$ represents the deflection angle of light. Setting the reduced deflection angle as

$$\overrightarrow{\alpha}(\overrightarrow{\theta}) \equiv \frac{D_{LS}}{D_S} \overrightarrow{\hat{\alpha}}(\overrightarrow{\theta}), \tag{1.2.2}$$

we finally obtain the lens equation

$$\vec{\beta} = \vec{\theta} - \vec{\alpha}(\vec{\theta}), \tag{1.2.3}$$

which allows us to determine the intrinsic source position, if the image position and the deflection angle are known.

Conversely, solving the lens equation for the unknown $\vec{\theta}$, we can calculate the image positions of a source at $\vec{\beta}$ lensed by a lens with deflection field $\vec{\alpha}(\vec{\theta})$. Inverting the lens equation to compute the image positions is often complicated (due to the complex form that $\vec{\alpha}(\vec{\theta})$ can assume) and requires using numerical methods.

1.3 Lensing potential and convergence

Let us consider the projection of the Newtonian gravitational potential $\Phi(\vec{\theta})$ on the lens plane. If appropriately scaled, this can lead to the so called *effective lensing potential*, which characterizes the lens mass distribution:

$$\hat{\Psi}(\vec{\theta}) = \frac{D_{LS}}{D_L D_S}\frac{2}{c^2}\int \Phi(D_L\vec{\theta}, z)\, dz. \tag{1.3.1}$$

It can be shown that the reduced deflection angle is the gradient of the effective lensing potential:

$$\vec{\nabla}_\theta \hat{\Psi}(\vec{\theta}) = \vec{\alpha}(\vec{\theta}). \tag{1.3.2}$$

Another convenient property involves the *convergence* $\kappa(\vec{\theta})$, defined through the surface density $\Sigma(\vec{\theta})$ as

$$\kappa(\vec{\theta}) \equiv \frac{\Sigma(\vec{\theta})}{\Sigma_{cr}}, \tag{1.3.3}$$

where $\Sigma_{cr} = \frac{c^2}{4\pi G}\frac{D_S}{D_L D_{LS}}$ is the critical surface density, namely the characteristic density to distinguish between strong and weak gravitational lensing regions. Since the spacetime curvature is more pronounced near the lens centre, in case of good alignment between observer, lens and source, the effect of gravitational lensing will be more evident: we talk about *strong* lenses. On the other hand, if the alignment does not guarantee a significant light deflection, the effect is called *weak*. From the convergence, we can obtain the following equation

$$\Delta_\theta \hat{\Psi}(\vec{\theta}) = 2\kappa(\vec{\theta}), \tag{1.3.4}$$

which states that the laplacian of the lensing potential is twice the convergence.

From these definitions, it appears that lensing quantities such as the lensing potential (Eq. 1.3.1), the deflection angle (Eq. 1.2.2) and the convergence (Eq. 1.3.3) strongly depend on a combination of the angular diameter distances D_{LS}, D_L and D_S. The distance ratio $\frac{D_{LS}D_L}{D_S}$, called *Lensing Distance*, in turn depends on the source and lens redshift. In particular, Figure 1.2 shows how the Lensing Distance varies with the source (Figure 1.2a) or lens (Figure 1.2b) redshift: it increases with the source redshift and peaks when the lens is at an intermediate distance between the source and the observer. Obviously, the larger the lensing distance is, the stronger lensing effects are generated. From Figure 1.2b we can also see that the peak moves to larger distances as the source distance increases.

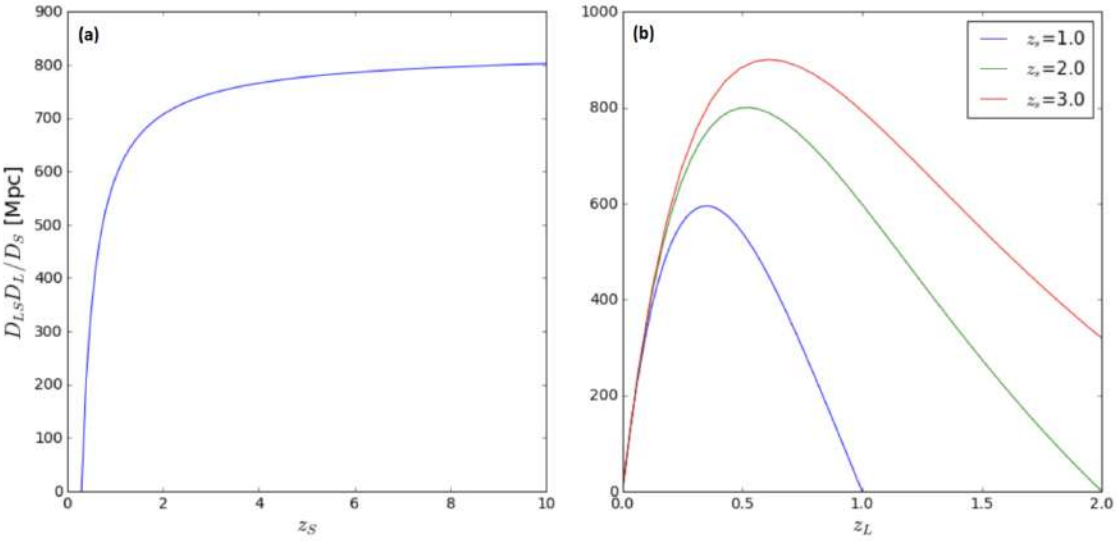

Figure 1.2: (a) Variation of the lensing distance as a function of the source redshift; (b) variation of the lensing distance as a function of the lens redshift when the source distance increases.

1.4 First-order lens mapping

If we assume the angular scale on which the deflection angle varies is significantly larger than the source size, the lens mapping between the lens and the source plane described by the lens equation can be linearized.

On the source plane we can identify two points $\overrightarrow{\beta}$ and $\overrightarrow{\beta'} = \overrightarrow{\beta} + d\overrightarrow{\beta}$. Mapping the distance between them on the lens plane, we define a linear mapping between the two planes, described by the inverse of the *lensing Jacobian matrix*:

$$A \equiv \frac{d\overrightarrow{\beta}}{d\overrightarrow{\theta}} = \left(\delta_{ij} - \frac{\partial^2 \hat{\Psi}}{\partial\theta_i \partial\theta_j}\right). \tag{1.4.1}$$

It is a symmetric second-rank tensor, which can be written as the sum of an isotropic and an anisotropic part:

$$A_{iso,ij} = \frac{1}{2}\mathrm{TrA}\delta_{ij} = (1-\kappa)\delta_{ij}, \tag{1.4.2}$$

$$A_{aniso,ij} = A_{ij} - \frac{1}{2}\mathrm{TrA}\delta_{ij} = \begin{pmatrix} -\frac{1}{2}(\hat{\Psi}_{11} - \hat{\Psi}_{22}) & -\hat{\Psi}_{12} \\ -\hat{\Psi}_{12} & \frac{1}{2}(\hat{\Psi}_{11} - \hat{\Psi}_{22}) \end{pmatrix}. \tag{1.4.3}$$

From Eq. 1.4.3 we can define the *shear* Γ, which is a symmetric, trace-less, 2x2 tensor, whose form is described by two components, namely:

$$\gamma_1 = \frac{1}{2}(\hat{\Psi}_{11} - \hat{\Psi}_{22}), \tag{1.4.4}$$

$$\gamma_2 = \hat{\Psi}_{12}. \tag{1.4.5}$$

We can define the shear module as $\gamma = \sqrt{\gamma_1^2 + \gamma_2^2}$ and the shear eigenvalues are $\pm\gamma$. Therefore, we can rewrite Γ through an angle ϕ which represents the direction of the eigenvector corresponding to the positive eigenvalue:

$$\Gamma = \gamma \begin{pmatrix} \cos(2\phi) & \sin(2\phi) \\ \sin(2\phi) & -\cos(2\phi) \end{pmatrix}. \tag{1.4.6}$$

Considering both the expressions of A_{iso} and A_{aniso}, the lensing Jacobian matrix becomes

$$A = (1-\kappa) \begin{pmatrix} 1 & 0 \\ 0 & 1 \end{pmatrix} - \gamma \begin{pmatrix} \cos(2\phi) & \sin(2\phi) \\ \sin(2\phi) & -\cos(2\phi) \end{pmatrix}. \tag{1.4.7}$$

From this expression we can state the lensing Jacobian matrix is made of two parts. The first part, depending on the convergence, describes an isotropic transformation of the source image, which is hence expanded or contracted by the same factor in all directions, while the second one, depending on the shear, represents an anisotropic transformation, distorting the image in a specific direction, given by the angle ϕ. More precisely, the image size is increased compared to the source in the direction of the eigenvectors of A with eigenvalue γ, and decreased in the perpendicular direction. The amounts of these magnifications and de-magnifications are given by the inverse of the tangential and radial eigenvalues of A, namely λ_t and λ_r:

$$\lambda_t = 1 - \kappa - \gamma \qquad\qquad \lambda_r = 1 - \kappa + \gamma. \tag{1.4.8}$$

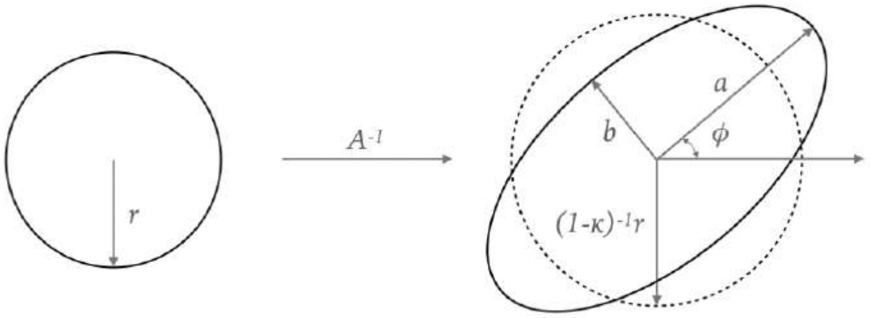

Figure 1.3: Distortion effects on a circular source caused by convergence and shear.

As an example, a circular source with radius r will be distorted as shown in Figure 1.3. Due to the convergence term, it is mapped onto a larger (or smaller) circle, whose radius is $r/(1-\kappa)$. Due to the shear term, the circle is further elongated in the direction given by the angle ϕ and contracted in the perpendicular direction to form an ellipse. The major and minor axes of the ellipse are given by

$$a = \frac{r}{\lambda_r} \qquad\qquad b = \frac{r}{\lambda_t}. \tag{1.4.9}$$

1.5 Magnification

Gravitational lensing guarantees the conservation of surface brightness, as it does not involve photon creation or absorption (Liouville Theorem), but changes the solid angle the source subtends and, consequently, focuses the photons we receive from the source itself on a smaller area. The *magnification* μ quantifies this change. Let us consider a circular source with area S, which is distorted by gravitational lensing into an elliptical image with area I, we can define the magnification as follows:

$$\mu \equiv \frac{I}{S} = \frac{1}{\mathrm{detA}}, \tag{1.5.1}$$

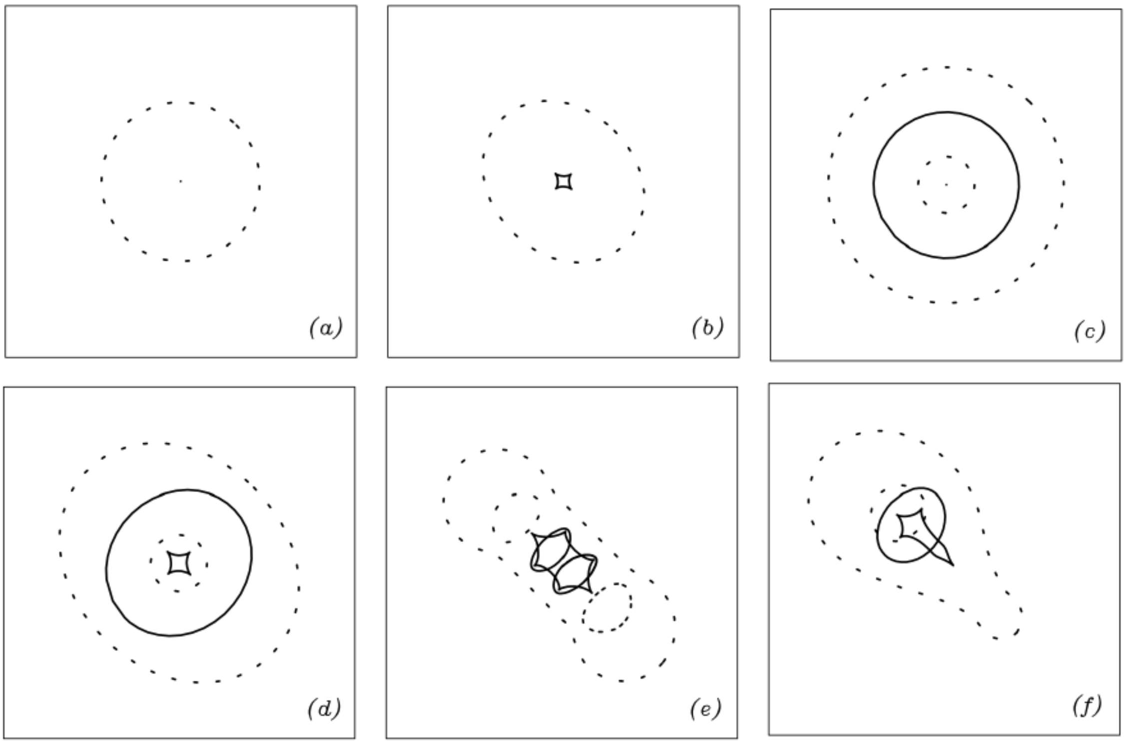

Figure 1.4: Caustics (solid) and critical lines (dashed) for different mass models: (a) a singular isothermal circular mass distribution generates only the critical lines, in particular the radial critical line is the central point and the tangential critical line is the circle; (b) a singular isothermal elliptical lens produces a tangential caustic which is an astroid and the corresponding tangential critical line; (c) a circular and (d) an elliptical mass distribution with an inner slope shallower than the isothermal mass distribution generate both the critical lines and the caustics; a bimodal mass distribution with two clumps of equal (e) or unequal (f) mass produces more complex critical lines and caustics (26).

where we have used Eq. 1.4.9 to calculate the area $I = \pi ab$. The total magnification is the product of the tangential and radial magnification $\mu = \mu_t \cdot \mu_r$, where $\mu_t = \frac{1}{\lambda_t}$ and $\mu_r = \frac{1}{\lambda_r}$.

Both convergence and shear are functions of the position on the lens plane $\vec{\theta}$, and so does also the Jacobian matrix. The points on the lens plane in which the eigenvalues of the Jacobian are zero form the *critical lines*. Along these lines the magnification diverges. If we map them onto the source plane using the lens equation we obtain the *caustics*. Critical lines are hence defined on the lens plane and the caustics on the source plane. The shape of caustics and critical lines varies with the mass distribution of the lens. Figure 1.4 shows some examples for different simple mass distributions.

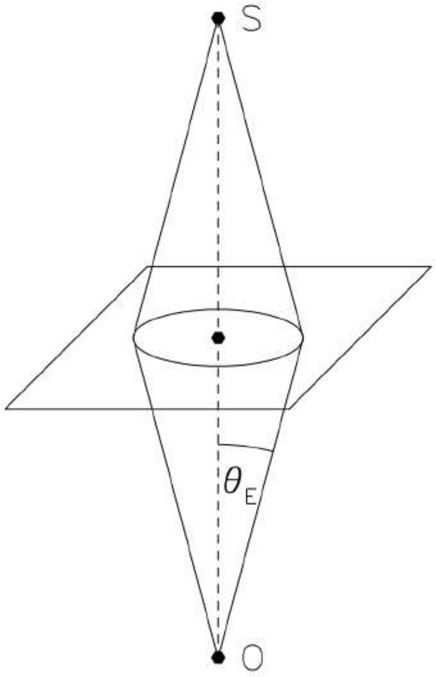

Figure 1.5: The outline of an Einstein ring: a source exactly behind the centre of an axially symmetric lens generates a ring with angular size θ_E (37).

If the source is located near a caustic, the corresponding images near a critical line will be characterized by a strong amplification and intense tangential or radial deformation. Clearly, the number of images varies with the source position in the lens system. If a circular lens is exactly along the observer's line of sight to a source, we observe a configuration called the *Einstein ring* (Figure 1.5), formed by the multiple images merged into a ring-like structure, centered on the lens. The size of an Einstein ring is given by the *Einstein radius* as

$$\theta_E = \sqrt{\frac{4GM(\theta)}{c^2}\frac{D_{LS}}{D_L D_S}}. \tag{1.5.2}$$

The concept of Einstein radius can be extended also to non circular lenses. Given a lens with a tangential critical line of area A_t, we define the Einstein radius as $\theta_E = \sqrt{\frac{A_t}{\pi}}$.

It is worth mentioning the strong dependence of the Einstein radius on the angular diameter distances and, hence, on the source and lens redshift (Figure 1.2).

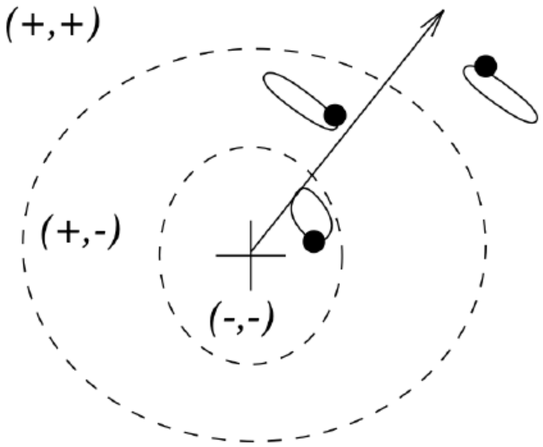

Figure 1.6: The dashed lines are the critical lines for an elliptical mass distribution: they split the image plane in regions with different image parities. Every time one crosses a critical line there is the change in sign of one of the eigenvalues of the Jacobian matrix and the parity of the image changes (26).

1.6 Multiple images

Light travelling in a gravitational potential also experiences a time delay relative to propagation in vacuum, made up of two different components: the first one is geometrical, due to the different paths followed by deflected light rays to reach the observer, and the second one is gravitational,

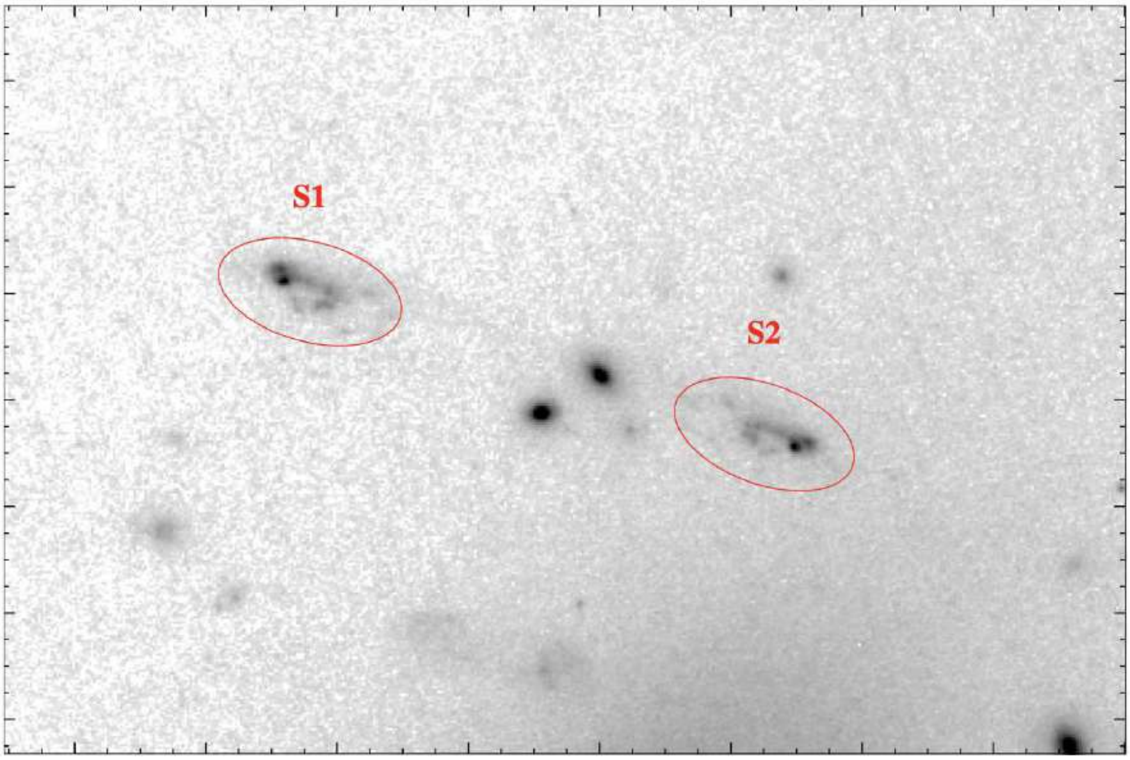

Figure 1.7: The lensed pair S1-S2 in AC114 is a classic example of inverted parity: this hook-like galaxy at $z = 1.867$ shows a clear change in parity (26).

due to the different effective speed of light in presence of a gravitational field. We can demonstrate that the function describing the total time delay as a function of the image position for a given source and lens is a surface, known as *time delay surface*, whose stationary points correspond to the multiple images.

The image multiplicity is then strongly related to the time delay surface and the shape of the time delay surface itself near the stationary points also provides hints on the shape of the images and on their *parity.* The parity of an image is related to the sign of the magnification: both a *positive* and *negative* magnification with absolute value > 1 lead to an amplification, but while a positive magnification produces an image whose orientation is the same as the one of the unlensed source, a negative magnification leads to an image whose parity is inverted. Every time one crosses a critical line there is the change in sign of one of the eigenvalues of the Jacobian matrix and the parity of the image changes (Figure 1.6). Therefore, the parities of images formed on the two sides of a critical lines are inverted (Figure 1.7).
In particular, we can identify three different type of images:

- in the minima the eigenvalues of A are both positive, hence $\det A > 0$ and $\mathrm{Tr} A > 0$, which leads to a positive magnification;
- in the saddle points the eigenvalues have opposite signs, thus $\det A < 0$, which leads to a negative magnification;
- in the maxima the eigenvalues are both negative, hence $\det A > 0$ and $\mathrm{Tr} A < 0$.

As an example let us consider an axially symmetric lens. Figure 1.8(1) represents the time delay surface corresponding to the Einstein ring. Here, we can see a symmetric scenario, with minima points located in a ring-like image and a maximum at the centre. This ring corresponds to the tangential critical line of the lens. But as soon as the source moves, the shape of the surface changes. Figures 1.8(2),(3) and (4) show these different configurations. As the source moves along the θ_1 axis the surface symmetry breaks. Firstly, a minimum point becomes a saddle point (2). Then, the saddle and the maximum point approach each other and when the two images merge, the time delay surface becomes radially flat (3) and the radial critical line forms. Lastly (4), we can see on the lens plane only one image, corresponding to the minimum of the time delay surface. Therefore, the image multiplicity depends on the relative position of lens and source. Every time the source crosses a caustic, a couple of different images merges in a single and elongated *gravitational arc.* When this happens the time delay function is flat and $\det A = 0$, that is infinite magnification. An axially symmetric lens can produce up to three multiple images.

Another example concerns elliptical potentials. The corresponding time delay surface can have up to five stationary points. Figure 1.9 shows the critical lines (a) and the caustics (b) of the lens. The blue dots represent the different source positions and Figure 1.10 shows the corresponding time delay surfaces. When the source is at $\overrightarrow{\beta} = 0$ (dot 1 in Figure 1.9b) the configuration has five multiple images: one maximum at the lens center, two minima which are symmetric with respect to the center of the lens and two saddle points, also symmetric, as we can see from the surface in Figure 1.10(1). This is the so called *Einstein cross.* If the source moves along the θ_1 axis, the configuration changes: in particular, if it is close to both the radial and tangential caustics (dot 2), the central maximum and the saddle points merge with a minimum, producing a radially and tangentially magnified image, while the other minimum follows the source along the β_1 axis. Instead, if we consider the θ_2 axis, it is worth mentioning how the surface modifies when the source is on the radial caustic (dot 3 and Figure 1.10(3)). In this situation two minima and a saddle point follow the source, while the maximum and the other saddle point merge in a radially magnified image. When the distance increases and the source approaches the cusp of the caustic (dot 4), even the remaining two minima and saddle point merge in a tangentially magnified image

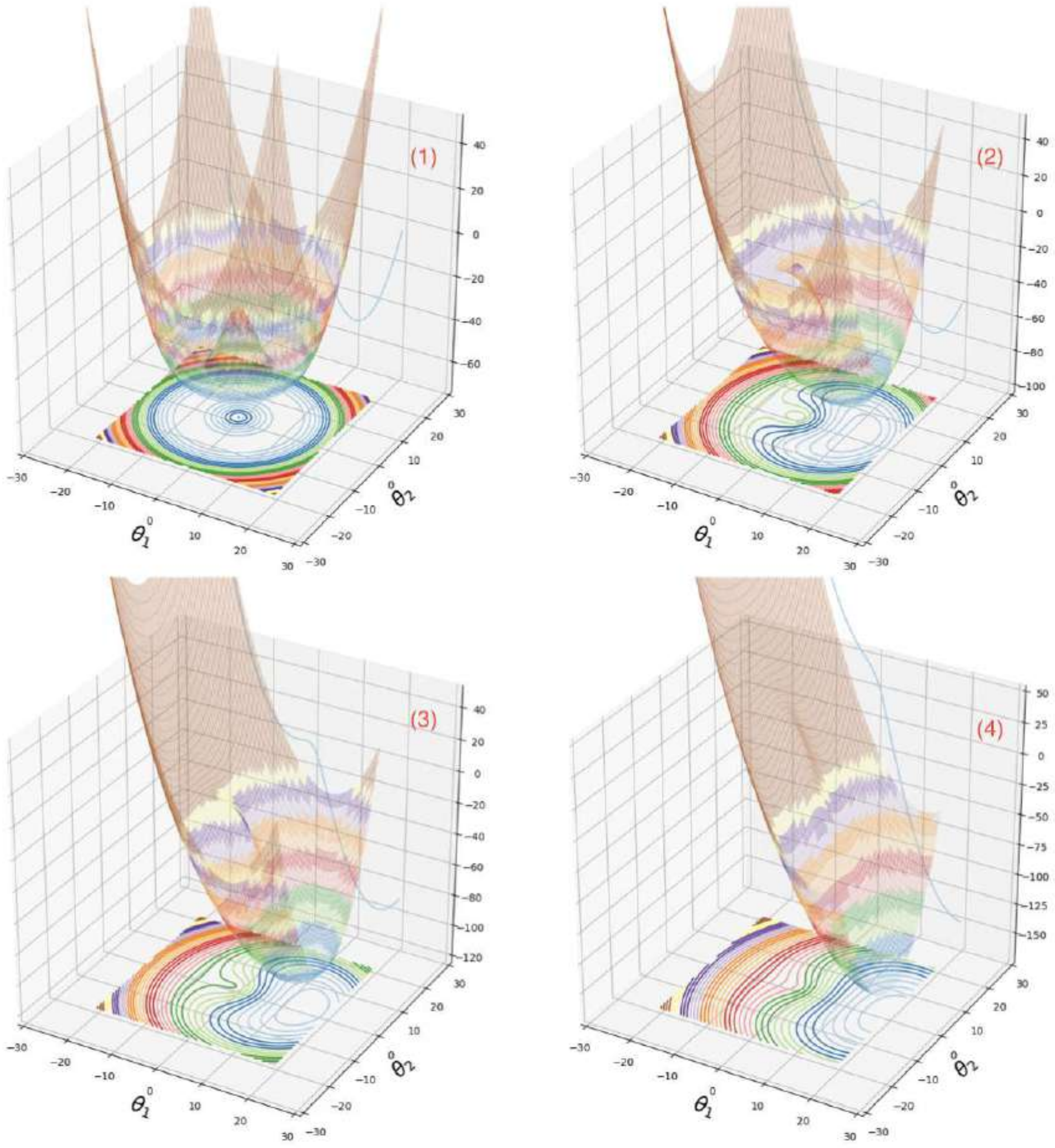

Figure 1.8: Axially symmetric lenses: time-delay surfaces corresponding to different positions of the source along the θ_1 axis. Also the projection of the surfaces on the (θ_1,θ_2) plane and the sections of the surfaces along the θ_1 axis are shown.

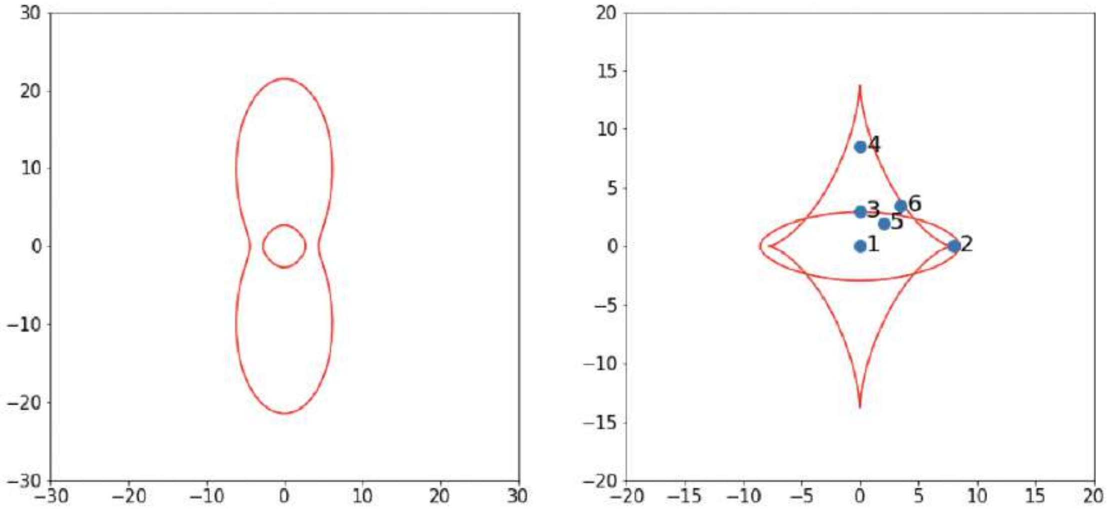

Figure 1.9: a) critical lines and (b) caustics of an elliptical potential. The blue dots represent the different source positions used to build the time delay surfaces represented in Fig 1.10.

(Figure 1.10(4)). If the source moves diagonally in the (θ_1, θ_2) plane, reaching the radial caustic (dot 5), on the surface (Figure 1.10(5)) a minimum goes in the same direction of the source, the other minimum and a saddle point approach each other, while the maximum and the other saddle point merge in radially magnified image. Finally, when the distance increases and the source reach the tangential caustic (dot 6), one of the remaining minima and the saddle point merge, forming a tangentially magnified image.

From these examples we can identify some crucial properties of image multiplicity:

- when the source crosses a caustic the number of images changes by two, because two images with different parity merge on the critical line;
- tangentially magnified images can be found near tangential critical lines and radially magnified ones near the radial critical lines;
- the more complex the mass distribution, the larger the multiplicities of images.

1.7 Second-order lens mapping

Up to now we have solved the lens equation using the first-order approximation. In this subsection we will go to the next level, studying the second-order approximation (28). This term in the lens equation can be expressed via a 2x2x2 tensor D, whose elements are the first derivatives of the Jacobian matrix elements:

$$D_{ijk} = \frac{\partial A_{ij}}{\partial \theta_k} = \frac{\partial^2 \beta_i}{\partial \theta_j \partial \theta_k}. \tag{1.7.1}$$

This tensor gives rise to asymmetrical distortions in the image, as well as a shift of the centroid

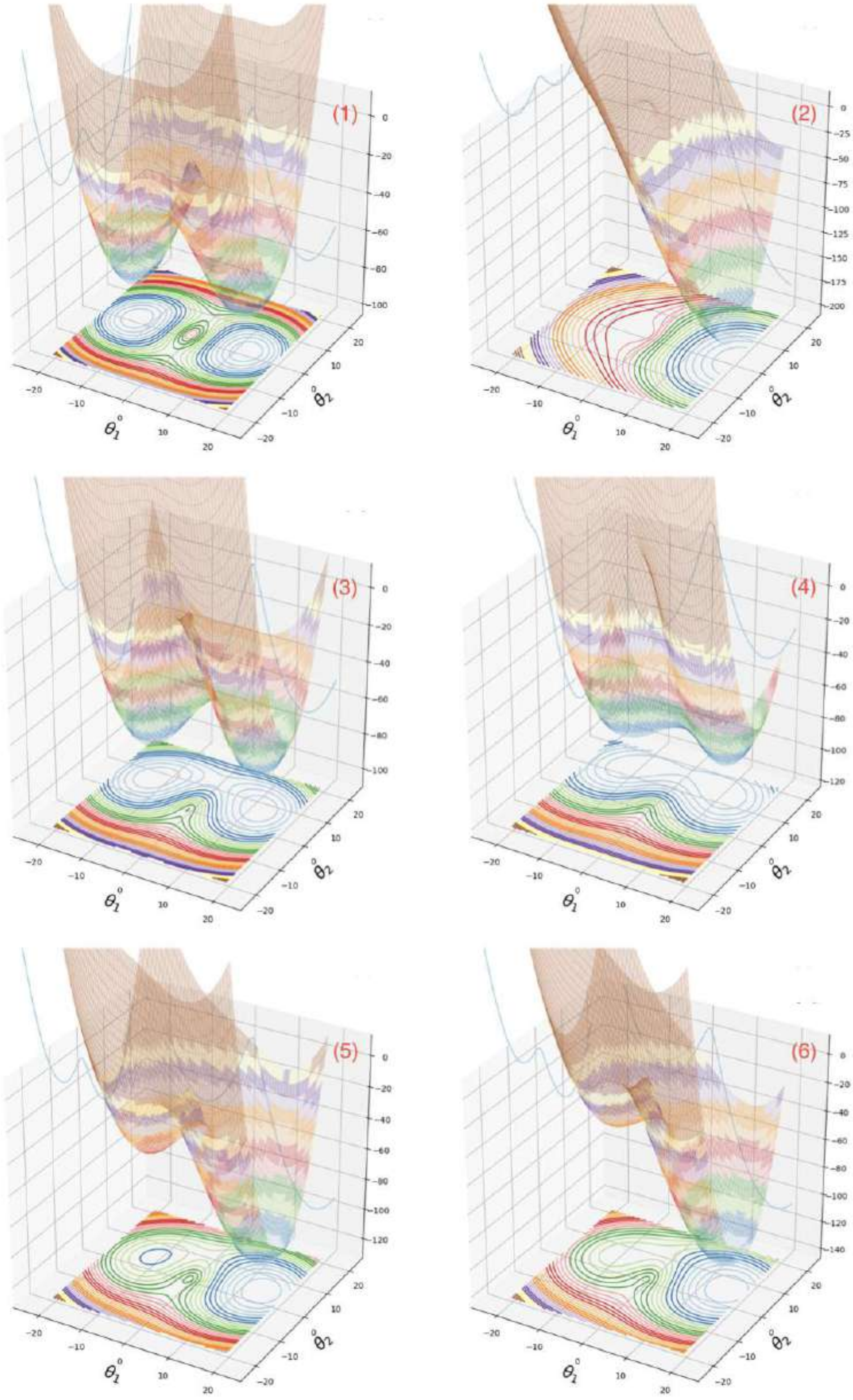

Figure 1.10: Elliptical potentials: time-delay surfaces corresponding to different positions of the source on the source plane. Also the projection of the surfaces on the (θ_1,θ_2) planes and the sections of the surfaces along the θ_1 axis are shown.

of the light distribution. It is common to resort to two operators, known as *flexions*, F and G, to rewrite the second-order term in a more compact way:

$$F = \partial\kappa = (\gamma_{1,1} + \gamma_{2,2}) + i(\gamma_{2,1} - \gamma_{1,2}) \tag{1.7.2}$$

and

$$G = \partial\gamma = (\gamma_{1,1} - \gamma_{2,2}) + i(\gamma_{2,1} + \gamma_{1,2}), \tag{1.7.3}$$

so that

$$\begin{aligned} D_{111} &= -\frac{1}{2}(3F_1 + G_1), \\ D_{222} &= -\frac{1}{2}(3F_2 - G_2), \\ D_{211} = D_{121} = D_{112} &= -\frac{1}{2}(F_2 + G_2), \\ D_{221} = D_{122} = D_{212} &= -\frac{1}{2}(F_1 - G_1). \end{aligned} \tag{1.7.4}$$

In particular, the first flexion F gives rise to a skewness in the light distribution of the lensed image and a shift in its centroid, while the second flexion G gives rise to a bending (Figure 1.11).

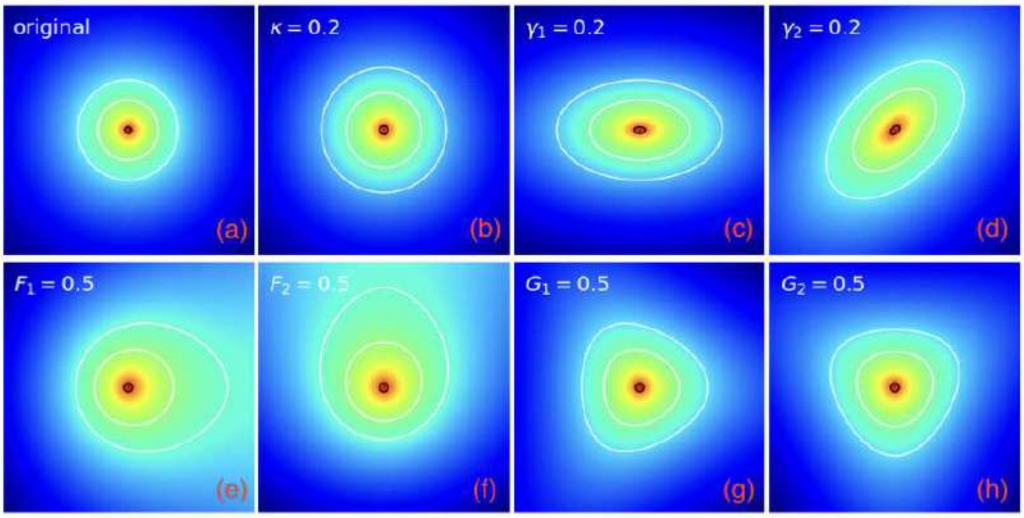

Figure 1.11: (a) Unlensed source; (b) effect of the convergence; (c) and (d) effect of the shear; (e) and (f) effect of the flexion F; (g) and (h) effect of the flexion G.

Higher-order terms in the expansion of the deflection angle field are required to properly describe the lens mapping in the regions with the highest magnifications.

Chapter 2

The high-redshift Universe through cosmic telescopes

2.1 Cosmic Telescopes

Galaxy clusters, thanks to their magnification, can be used as real cosmic telescopes to study the high-redshift Universe with spatial and spectral resolutions that otherwise would not be achievable. Sources located near the caustics of a cluster are so strongly magnified that we can resolve in their images regions as small as globular clusters, namely with intrinsic sizes $\lesssim$ 200 pc (49). These sources are particularly interesting because they can help to shed light on processes such as galaxy formation and evolution. Figure 2.1 shows the history of cosmic star formation from UV-IR rest-

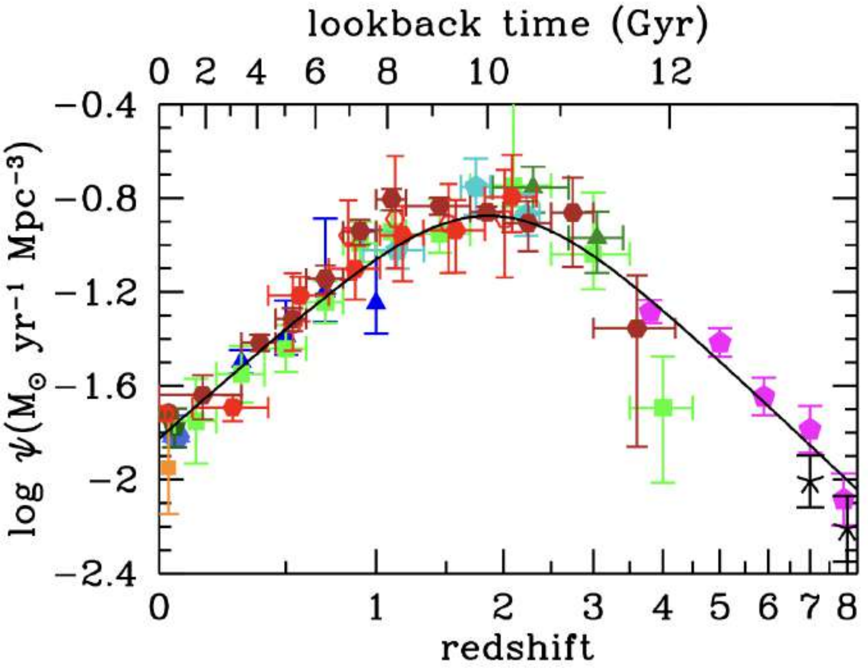

Figure 2.1: The history of cosmic star formation from UV-IR rest-frame measurements (31).

frame measurements as a function of redshift and it is clear that star formation has a peak at $z \sim 2$. Therefore, it is crucial to reach these redshifts with an accurate spatial resolution to properly study star and galaxy formation and evolution. As an example it is worth mentioning the *Sunburst Arc* (Figure 2.2), a giant tangential arc visible in the cluster PSZ1 G311.65-18.48 at $z = 0.443$. The Sunburst Arc is the lensed image of a source at $z = 2.369$, hosting a compact star formation region which is visible 12 times in the tangential arc itself (43).

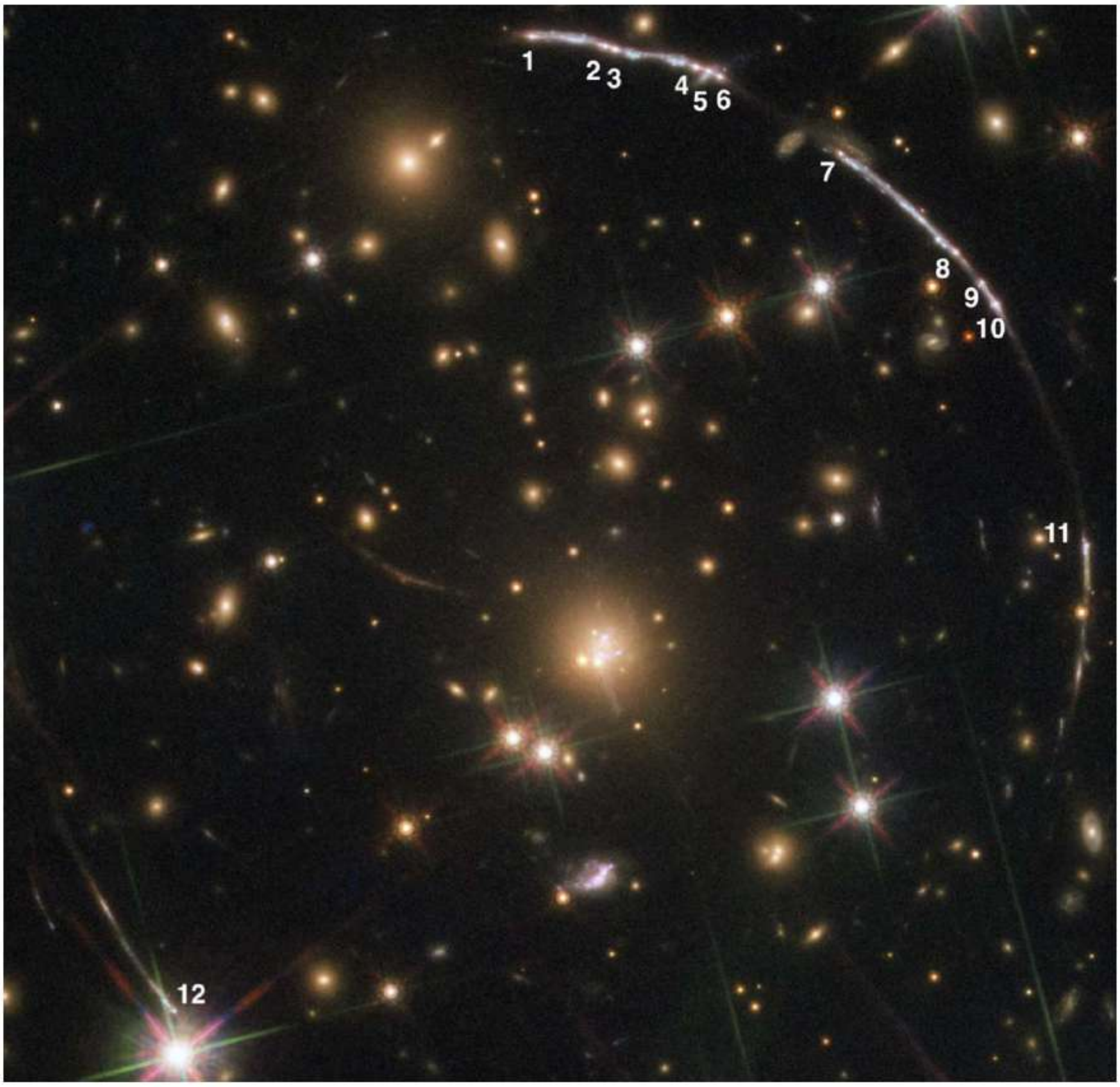

Figure 2.2: The core of the galaxy cluster PSZ1 G311.65-18.48, observed with the Hubble Space Telescope. We can see the Sunburst Arc and the white numbers correpond to the multiple images of the star formation region (43).

Moreover, very high-redshift star-forming galaxies and stellar clusters are also essential to understand the *reionization* process, which took place in the redshift interval between 5 and 15, namely when the first objects began to form. During this period of time, the neutral gas in the early Universe was ionized by the hard ultraviolet radiation emitted by the first sources. But, it is still unclear which sources could have contributed the most: the Pop III stars (the first generation of stars), a population of faint dwarf galaxies, X-ray binaries or nuclear black holes. Anyway, the gravitational lensing magnification can help to better study the most distant sources in order to solve this puzzle.

2.2 Instruments

Studies such as the ones described in the previous section make use of particular instruments, with appropriate angular resolutions. Outlined below there is a list of the main telescopes, for each of which we specify its most significant achievements. It is worth noting that, due to cosmological redshift, rest-frame UV/optical galaxies are redshifted in the near-infrared band, since the cosmological redshift is defined as

$$z = \frac{\lambda_o - \lambda_e}{\lambda_e}, \tag{2.2.1}$$

where λ_e is the wavelength of radiation emitted by the source and λ_o is the one in the position of the observer. For instance, at $z > 7$, the Lyα break ($\lambda_e = 0.12\mu$m) and the Balmer break ($\lambda_e = 0.38\mu$m) are redshifted out of the optical bands. Thus, it is possible to observe star-forming galaxies at high redshift only through telescopes whose wavelength range covers the infrared band.

2.2.1 Space Telescopes

The main advantage of using space telescopes lies in the fact that they are above the Earth's atmosphere, avoiding hence blurring effects and absorption or reflection of many wavelenghts of the electromagnetic spectrum. Just the optical and radio bands and a small portion of the infrared one can go through the atmosphere and reach the Earth.

- Hubble Space Telescope (HST-ACS/WFC3): this space telescope observes the Universe in visible, ultraviolet and infrared wavelengths. In particular, of the instruments assembled on board, the most used for gravitational lensing purposes are the ACS (*Advanced Camera for Surveys*) and WFC3 (*Wild Field Camera 3*). It is worth noting that WFC3 combines two optical/ultraviolet CCDs (WFC3/UVIS) with a near-infrared array (WFC3/IR). With a primary mirror of 2.4 m diameter, HST allows the production of high quality imaging thanks to the spatial resolution of its instruments: ACS can provide a resolution of 0.05 arcsec/pxl, while WFC3/IR and WFC3/UVIS 0.13 arcsec/pix and 0.04 arcsec/pxl, respectively. Covering the optical and NIR parts of the electromagnetic spectrum, ACS and WFC3/IR prove to be a fundamental tool to study star-forming galaxies in the high-redshift Universe. Table 2.1 reports some useful information, such as the spectral range, the field of view, the array size and the pixel scale for both cameras. Table 2.2 lists the Full Width at Half Maximum (FWHM) of some filters associated to these instruments, whose integrated system throughput is shown, for clarity, in Figure 2.3.

Instrument	Spectral range (nm)	FoV	Array size (pxl)	Pixel scale (”/pxl)
ACS	350-1050	202”x202”	4096x4096	0.05
WFC3/IR	850-1700	123”x137”	1024x1024	0.13
WFC3/UVIS	200-1000	160”x160”	4096x4096	0.04

Table 2.1: HST ACS-WFC3 main properties (2; 46).

ACS		WFC3/IR	
Filter	FWHM (”)	Filter	FWHM (”)
F435W	0.17	F105W	0.31
F606W	0.13	F125W	0.33
F814W	0.14	F140W	0.33
		F160W	0.34

Table 2.2: FWHM of some filters associated to ACS and WFC3/IR, obtained from a Gaussian fit to the PSF.

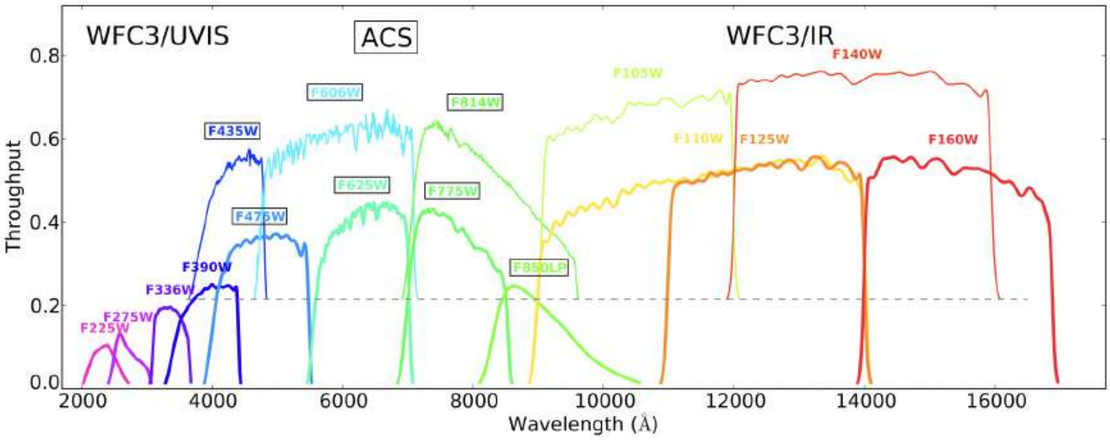

Figure 2.3: The integrated system throughput of some HST filters (42).

- Spitzer Space Telescope[1]: it was an infrared space telescope with a primary mirror of 85 cm in diameter. Its most important camera for gravitational lensing studies was IRAC (*Infrared Array Camera*). IRAC was a four-channel camera, namely made of four different infrared detectors, operating at $3.6, 4.5, 5.8$ and 8.0 μm. Compared to HST-WFC3/IR, IRAC could cover a higher wavelength range, providing the opportunity of observing star-forming galaxies at ever higher redshifts. At $z > 7$ the Balmer break ($\lambda_e = 0.38\mu$m) is redshifted directly into the IRAC wavelength range. For instance, the $z \sim 9.6$ object analyzed in (51) is detected just in the two reddest bands of HST-WFC3/IR and in the IRAC channels. This instrument properties are better described in Table 2.3.

---

[1] `https://irsa.ipac.caltech.edu/data/SPITZER/docs/irac/iracinstrumenthandbook/IRAC_Instrument_Handbook.pdf`

Instrument	Spectral range (μm)	FoV	Array size (pxl)	Pixel scale ("/pxl)
IRAC	3.6, 4.5, 5.8, 8.0	5.2'x5.2'	256x256	1.2

Table 2.3: Spitzer IRAC main properties.

Channel	1	2	3	4
FWHM (")	1.66	1.72	1.88	1.98

Table 2.4: FWHM of the filters associated to Spitzer IRAC.

The spectral response curves for the four IRAC channels are shown in Figure 2.4, while Table 2.4 lists the FWHM values obtained from a Gaussian fit to the PSF.

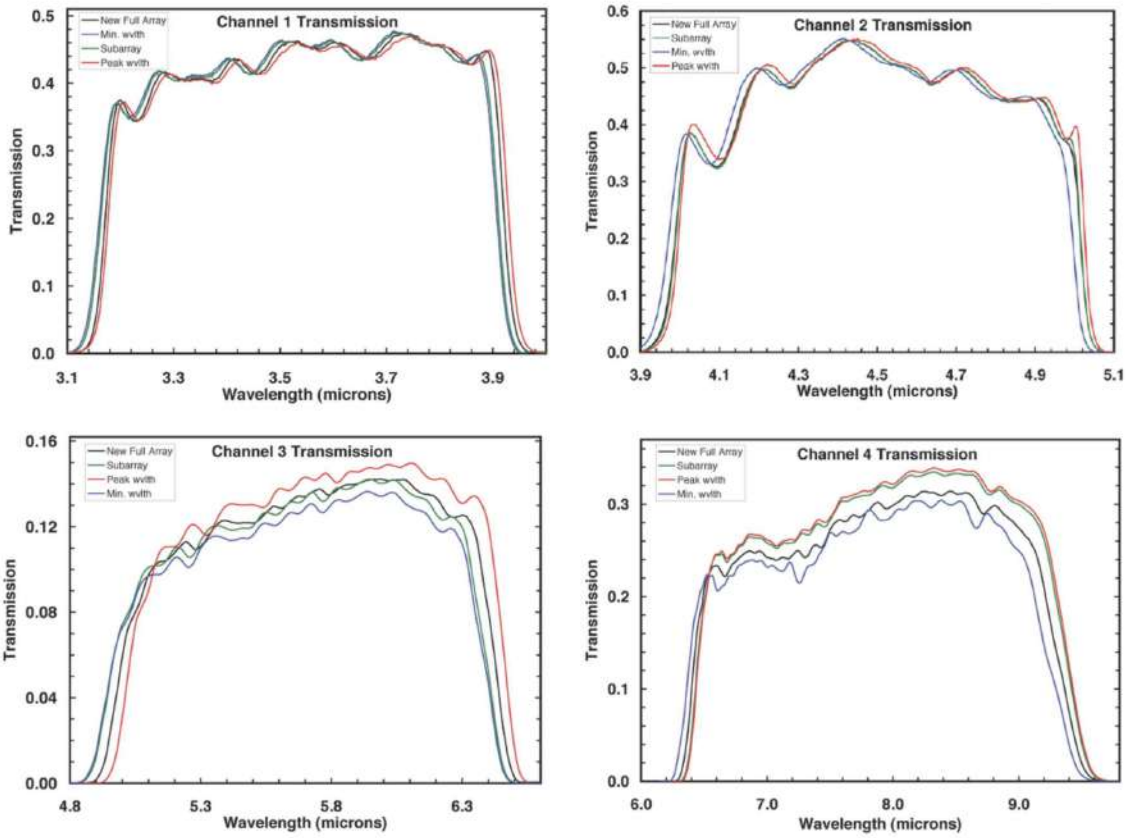

Figure 2.4: The integrated system throughput of the four IRAC channels.

- James Webb Space Telescope (JWST): this space telescope observes the Universe in infrared wavelengths with a primary mirror of 6.5 m in diameter. NIRCam[2] (*Near Infrared Camera*) is the main imaging instrument on board. It can observe simultaneously in a short wavelength channel (0.6-2.3 μm) and long wavelength channel (2.4–5.0 μm) via a dichroic beam splitting. It is worth mentioning also the instrument NIRISS[3] (*Near Infrared Imager*

---

[2] https://jwst-docs.stsci.edu/jwst-near-infrared-camera/nircam-observing-modes/nircam-imaging

[3] https://jwst-docs.stsci.edu/jwst-near-infrared-imager-and-slitless-spectrograph/niriss-observing-modes/niriss-imaging

and Slitless Spectrograph), which can be used in two observing modes, as a spectrograph or an imager. Note that NIRISS/imager works only as a parallel observing mode, but despite this it gives images of a better quality than the HST cameras. The third instrument on board is MIRI[4] (*Mid-Infrared Instrument*). It works both as a camera and a spectrograph covering the mid-infrared band. Imaging spans the wavelength range from 5.6 μm to 25.5 μm with a spatial resolution of 0.11 "/pxl, while spectroscopy consists of a low resolution mode from 5 to 14 μm and a medium resolution mode from 4.9 to 27.9 μm. Finally, NIRSpec[5] (*Near Infrared Spectrograph*) provides near-IR spectroscopy in four observing modes. NIRSpec, in fact, enables a standard single-slit spectroscopy to collect spectra of peculiar objects. But it also has an integral field unit, which combines imaging and spectroscopy in order to observe how different emitting regions vary in space. A microshutter array then allows multi-object spectroscopy and is ideal for studying high-redshift galaxies, which require very long observation times. Lastly, a Time-Series Spectroscopy allows to take spectra at regular intervals of time in order to observe how the spectrum changes in time. In particular, comparing JWST/NIRCam (Table 2.5) with HST/WFC3 (Table 2.1), it can be noticed that NIRCam/short covers a wider wavelength range with a definely better space resolution, while NIRCam/long extents over the WFC3 upper limit. In fact, NIRCam/long spans a wavelength range which is a part of the Spitzer/IRAC (Table 2.3) spectral range with an improvement in spatial resolution. The second half of IRAC spectral range is covered by JWST/MIRI, which reaches even 25.5 nm with a resolution of 0.11 "/pxl. Therefore, JWST allows us to obtain better quality images both in the near and mid-infrared bands, becoming hence crucial in the observation of the very high-redshift Universe. Finally, Table 2.6 includes the FWHM of some filters associated to NIRCam, whose integrated system throughput is shown, for clarity, in Figure 2.5.

Instrument	Spectral range (μm)	FoV	Array size (pxl)	Pixel scale ("/pxl)
NIRCam/short	0.6-2.3	2×2.2'×2.2'	8×2040x2040	0.031
NIRCam/long	2.4-5.0	2×2.2'×2.2'	2×2040x2040	0.063
NIRISS/Imager	0.8-5.0	2.2'×2.2'	2030x2030	0.065
NIRSpec	0.6-5.3	3.4'x3.6'	2x2048x2048	0.1
MIRI/Imager	4.9-28.8	74"x113"	1024×1032	0.11

Table 2.5: JWST NIRCam, NIRISS/Imager, NIRSpec and MIRI main properties.

Filter	F070W	F090W	F115W	F150W	F200W
FWHM (")	0.04	0.04	0.04	0.05	0.07

Table 2.6: FWHM of some filters associated to NIRCAM, obtained from a Gaussian fit to the PSF.

---

[4] `https://jwst-docs.stsci.edu/jwst-mid-infrared-instrument`

[5] `https://jwst-docs.stsci.edu/jwst-near-infrared-spectrograph`

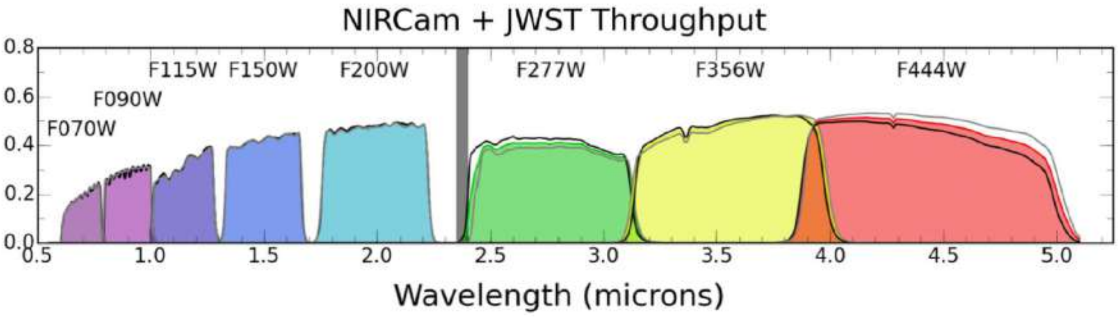

Figure 2.5: The integrated system throughput of some NIRCam filters.

2.2.2 Lensing Observing Campaigns from Space

During its operating life HST, combined with Spitzer, has undertaken several detailed observations of the innermost region of strong lensing clusters. Some surveys carried out in the last decade include:

- the Cluster Lensing and Supernova Survey with Hubble (CLASH): this survey focused on a sample of 25 massive galaxy clusters with redshifts between $z = 0.187$ and $z = 0.89$ (42). The sample was observed in 16 broadband filters, spanning from the UV to near-IR, using HST ACS and both the UVIS and IR channels of HST WFC3. These observations required over 525 orbits of HST to reach down to AB magnitude 26 in the 16 filters. The main goal of CLASH was to study the dark matter distribution in galaxy clusters using the strong lensing effect. In addition, the lens models constructed for these clusters were also used to characterize the properties of high-redshift magnified sources ($z > 7$) and to study the evolution of the galaxies inside the clusters themselves. Lastly, the depth of the survey allowed the detection of Type Ia supernovae out to redshift $z \sim 2.5$, which is fundamental to study the role of dark energy over time. This survey allowed to observe one of the galaxies with the highest redshifts, MACS0647-JD, lensed by the cluster MACS J0647+7015. It is estimated this galaxy has $z \sim 10.7$ (16; 42).

- the Hubble Frontier-Fields (HFF): this survey observed six massive galaxy clusters with redshifts between $z = 0.308$ and $z = 0.545$, namely Abell 2744, MACS J0416.1-2403, MACS J0717.5+3745, MACS J1149.5+2223, Abell S1063 and Abell 370. These observations required over 840 orbits of HST in order to reach down to AB magnitude 29 in 7 bands and over 1000 hours of Spitzer/IRAC time to obtain 3.6 and 4.5 μm imaging to depths of 26.5 and 26.0 AB magnitude. The combined observations from HST and Spitzer, together with the power of gravitational lensing, were meant to produce those which were the deepest images before the advent of JWST (30).

- the Reionization Lensing Cluster Survey (RELICS): this survey used HST and Spitzer to observe 41 galaxy clusters with redshifts between $z = 0.182$ and $z = 0.972$. Each cluster required a five-orbit HST imaging in 7 filters (the same bands used by the HFF), reaching down to 26.5 AB magnitude in the F160W. Hence, in comparison with CLASH or HFF, RELICS covered a wider area with relatively shallower imaging, in order to observe a large sample of the brightest high-redshift galaxies and to study the reionization epoch (17).

- the SLOAN Giant Arcs Survey (SGAS): this survey aimed at detecting highly magnified sources in the form of gravitational arcs. It developed from the ground-based Sloan Digital Sky Survey (SDSS): only the SDSS data containing gravitational arcs were selected and later observed with HST through follow-up. The SGAS is a fundamental starting point for studies of arc statistics (3).

(a) **(b)**

Figure 2.6: The galaxy cluster SMACS0723 observed by HST (a) and JWST (b).

2.2.3 Ground-based Telescopes

- VLT: The *Very Large Telescope* is located in the Atacama Desert in Chile and consists of four telescopes, each with a primary mirror of 8.2 m. If combined, these telescopes can achieve a very high angular resolution (0.002 arcseconds) and can be used to do interferometry (VLTI). The VLT instrumentation covers a wide wavelength range, from far UV (300 nm) to mid-infrared (24 μm), and includes instruments for both imaging and spectroscopy. In particular, it is worth mentioning the MUSE[6] (*Multi-Unit Spectroscopic Explorer*), which is a ground-based integral-field spectrograph operating in the optical wavelength range. MUSE can work in a Wide Field Mode (WFM) with a field of view of 1x1 arcmin^2 and a Narrow Field Mode (NFM) covering 7.5x7.5 arcsec^2. An adaptive optic system provides this spectrograph with a high spatial resolution: in the WFM it can reach 0.3 arcsec, while in the NFM up to 0.03 arcsec. Therefore, MUSE combines the discovery capacity of an imaging camera with the measuring efficiency of a spectrograph, together with the spatial resolution provided by the adaptive optic system. An important achievement led to the CLASH-VLT VIMOS Large

---

[6] https://www.eso.org/sci/facilities/develop/instruments/muse.html

Programme (45), where over 200 hours were spent to observe 13 southern CLASH galaxy clusters. The main aim was to obtain spectroscopic identification for about 500 members per cluster and for about 100 background lensed galaxies at $z < 7$. The final dataset contains approximately 30000 spectra and redshifts, providing material to better understand how galaxies evolve in different environments.

2.2.4 Important Results

The record-holder for the farthest galaxy known with a spectroscopic confirmation is GN-z11, at redshift $z = 10.96$, observed by HST (38). This achievement indicates that galaxy formation was already well underway 500 Myr after the Big Bang. Nevertheless, the limit of the observable Universe is determined by the Cosmic Microwave Background (CMB) at z $\sim$ 1100. Consequently, it emerges clearly we have an inherent $\sim$ 500 Myr gap, between the CMB ($z \sim 1100$) and the earliest known galaxies ($z \sim 11$), mainly due to the HST wavelength range. In fact, rest-frame UV/optical galaxies at $z > 11$ are redshifted towards wavelengths longer than 2000 nm, which HST cannot reach. However, this lack of deep and high-resolution imaging has been partially filled by JWST, which can reach wavelengths to 5000 nm. The JWST allows us not only to detect and confirm redshifts for galaxies with $z > 10$, but also to understand in detail galaxies at $3 < z < 10$. One of JWST first operating images contains the so called *Webb's First Deep Field*, centered on the galaxy cluster SMACS0723, observed also by HST in the RELICS program (Figure 2.6). By far, several

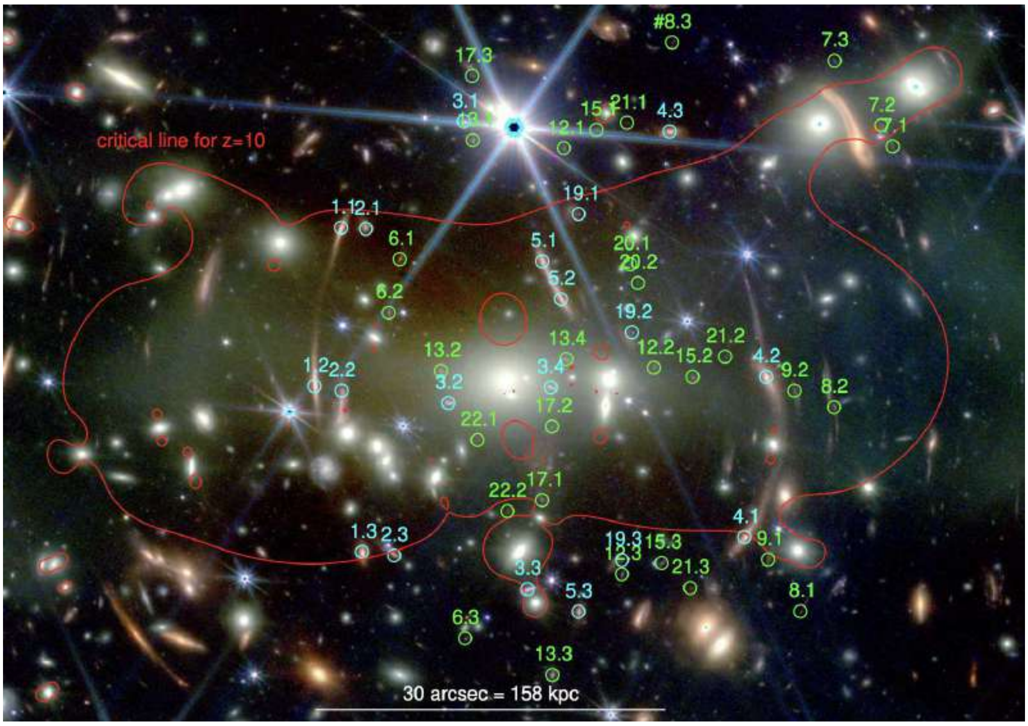

Figure 2.7: The galaxy cluster SMACS0723 observed by JWST/NIRCam. The red line is the critical line for a source at $z = 10$. The cyan circles show the positions of the multiple images found in the HST lens model, while the green circles represent the ones found with JWST (12).

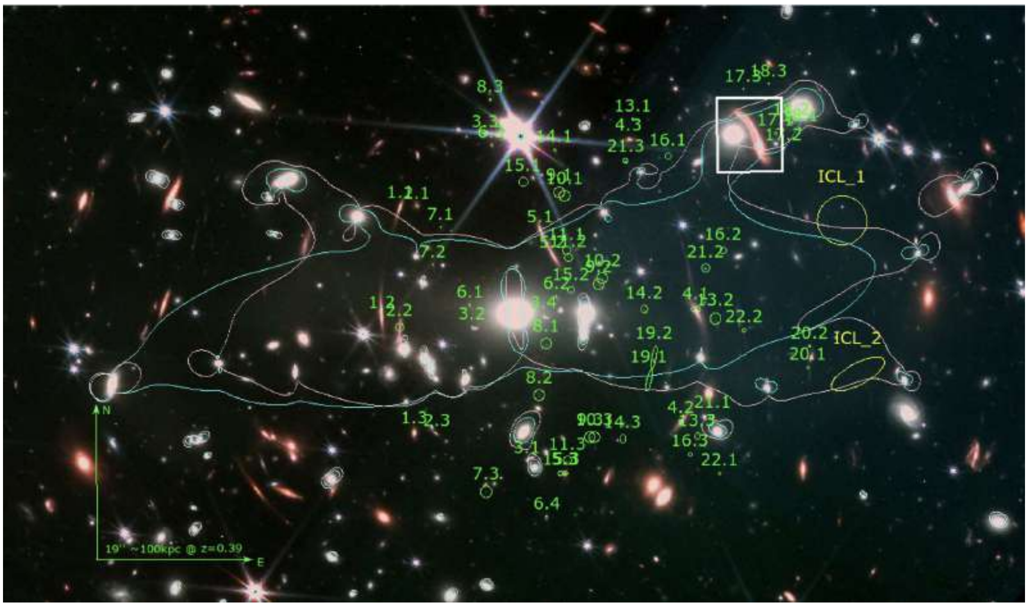

Figure 2.8: The galaxy cluster SMACS0723 observed by JWST/NIRCam. The cyan line is the critical line for a source at $z = 10$ and a single-component lens model, while the pink line corresponds to a lens model with two additional mass clumps. The green circles show the positions of the multiple images (32).

lens models of SMACS0723 has been built through both the JWST and the HST data. In (12) the lens model built through HST observations has 19 multiple images of six lensed sources, but the JWST model has 30 additional multiple images from other 11 background sources (Figure 2.7). From (32) it emerges there are 21 multiple-image systems inside MACS0723 and 16 of them have

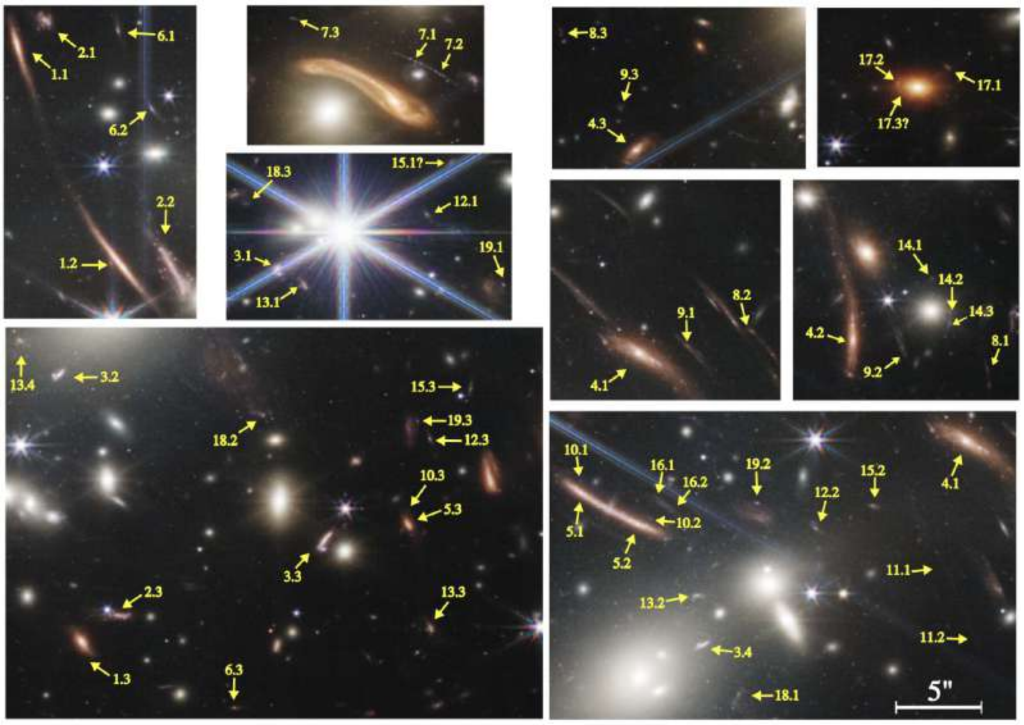

Figure 2.9: The multiple images identified in the SMACS0723 field from 19 background galaxies (39).

been discovered thanks to JWST (Figure 2.8). In (39) the JWST data seem to identify 14 new sets of multiply imaged galaxies inside the cluster for a total of 42 multiply images, while from the HST data only five sets seem to emerge (Figure 2.9). These JWST data are characterized by a level of detail that has never been seen before: we can reveal even the small substructures within these gravitational arcs, as we can see, for instance, in system 4 in Figure 2.9. Thanks to its sensitivity and angular resolution, the JWST in combination with gravitational lensing is, hence, crucial to study the high-redshift galaxies and to detect star-forming regions inside them.

2.3 Future instruments

Let us turn now our attention to future projects, listed below:

- Euclid[7]: this is a visible to near-infrared space telescope with a 1.2 m diameter. Euclid's main purpose is to study dark matter and dark energy. These goals will be reached through two primary cosmological probes, such as cosmic shear and the galaxy clustering. To achieve this, Euclid is going to observe 15000 square degrees of sky with two instruments: VIS[8] (*Visible*) and NISP[9] (*Near Infrared Spectrometer and Photometer*). It is worth noting that, while VIS is an imager with one wide visible band, NISP is an instrument composed of two channels, one photometric and one spectroscopic. About the 65% of Euclid's 6-year program will be spent in the Wide Survey, while in the remaining time it will focus on the Deep Survey, made of three deep fields: EDF-North, Chandra Deep Field-South, and EDF-South. The median image quality is expected to be 0.18 arcsecond in the VIS band (0.1 "/pixel) and 0.45 arcsecond in the near-infrared (0.3 "/pixel). Table 2.7 shows the instruments' main properties, while Table 2.8 lists the FWHM values associated to VIS and to the three filters of NISP. Figure 2.10 shows their integrated system throughput.

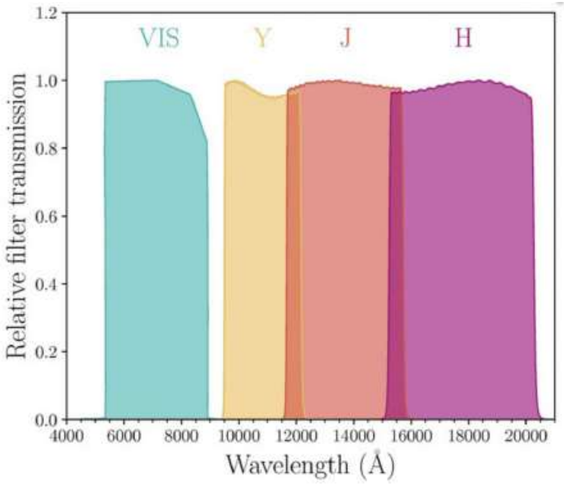

Figure 2.10: The normalized filter transmission of VIS and Y, J, H (NISP).

---

[7] https://www.euclid-ec.org/?page_id=2540

[8] https://sci.esa.int/web/euclid/-/euclid-vis-instrument

[9] https://sci.esa.int/web/euclid/-/euclid-nisp-instrument

Instrument	Spectral range (nm)	FoV	Array size	Pixel scale ("/pxl)
VIS	550-900	0.787 deg×0.709 deg	36x4096×4132	0.1
NISP/Imager	920-2000	0.763 deg×0.722 deg	16×2040×2040	0.3

Table 2.7: Euclid cameras main properties.

Instrument	VIS	NISP		
Filter	800 nm	Y	J	H
FWHM	0.19	0.33	0.33	0.35"

Table 2.8: FWHM of the filters associated to VIS and NISP, obtained from a Gaussian fit to the PSF.

- Vera C. Rubin Observatory[10]: the goal of this project is to conduct the *Legacy Survey of Space and Time* (LSST), which is supposed to cover over half the sky (18000 square degrees) in order to answer some questions about the structure and evolution of the Universe, such as probing dark energy and dark matter. This observatory will house the Simonyi Survey Telescope with its 8.4 m primary mirror and its 3200-megapixel camera. For the approximately 80% of its 10-year program, LSST will execute the Wide-Fast-Deep (WFD) survey, while in the remaining time it will observe four deep fields: ELAIS-S1, Extended Chandra Deep Field-South, XMM-LSS, and COSMOS. The Rubin's field of view is about 9.6 deg^2 and the observations will cover the u,g,r,i,z, and y photometric bands: in particular, the r-band is expected to reach a median image quality of 0.8 arcsecond. The properties of the LSST camera are reported in Table 2.9 and the integrated system throughput of its six filters is shown in Figure 2.11.

Instrument	Spectral range (nm)	FoV	Array size	Pixel scale ("/pxl)
LSST	400-1060	3.5 deg×3.5 deg	3 Gigapixel	0.2

Table 2.9: LSST camera main properties. The detector format will be circular and the fourth column contains the total number of pixels per image.

Since both Euclid and Rubin are projected to survey wide and partially overlapping sections of the sky with different angular resolutions and wavelength coverage, it sounds evident the development of an interaction between them (21). While Rubin's strategy gives priority to coverage and puts depth at the second place, Euclid does the exact opposite. Therefore, this synergy will join of Euclid's high spatial resolution in visible and near-infrared bands together with Rubin's deep optical imaging. It will offer unprecedented opportunities to study Solar Sistem Objects, resolved stellar populations, the Local Group and local galaxies out to $\sim 5-7$ Mpc and Transients, as well as galaxy evolution, galaxy clustering and the Primaeval Universe. Besides, the synergy has also an impact on gravitational lensing, in particular on lens finding (without multi-band optical imaging, Euclid alone cannot use the required color information) and on redshift estimating (since lens and

---

[10] `https://www.lsst.org/gallery/camera`

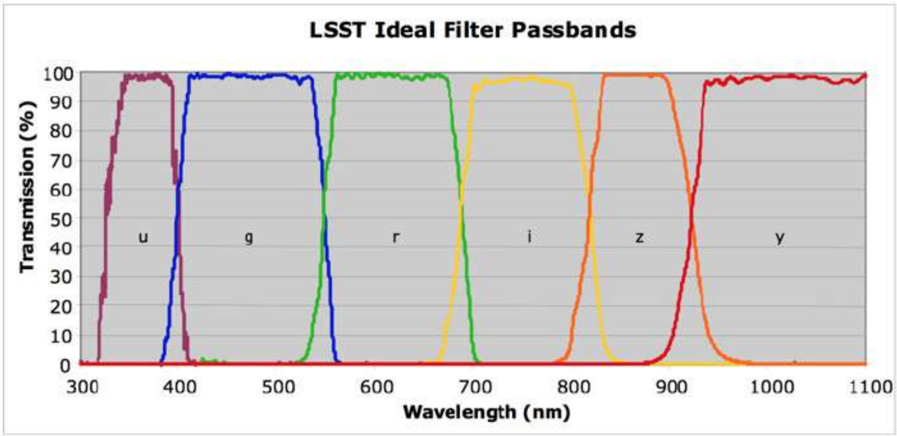

Figure 2.11: The normalized filter transmission of the LSST camera.

source usually overlap, estimating the source redshift can be extremely challenging without high resolution and multiband data).

- MAVIS[11]: this instrument is going to be installed on the Very Large Telescope (VLT). MAVIS stands for *MCAO Assisted Visible Imager and Spectrograph*. Its main quality is an adaptive optics system, MCAO (*Multi-Conjugate Adaptive Optics*), that cancels the distorting effects induced by the atmospheric turbulence in several directions. Today's adaptive optics systems provide a correction which is valid only in a small patch of sky (from a few arcsec to a few tens of arcsec, depending on the wavelength). On the other hand, MCAO will compensate the turbulence in volume, providing a corrected field of view which is from 10 to 20 times wider than to what can be produced with regular systems. Therefore, MCAO will ensure to MAVIS an angular resolution down to 18 milliarcseconds, exceeding that of HST. This feature, together with its large field of view, makes MAVIS ideal for deep field surveys, reaching an order of magnitude higher depth with respect to HST (30.4 mag vs 29.4 mag in the I band), but using 1/10th of the exposure time (10 hr vs $\sim$ 100 hr) (33). MAVIS will also be able to observe a large number of lensed sources behind those cluster lenses yet to be discovered with LSST and Euclid. Since it is an optical instrument, its work will be particularly useful in the low-redshift Universe, namely with $z < 0.5$. Table 2.10 lists the MAVIS's main properties.

Instrument	Spectral range (nm)	FoV	Array size	Pixel scale (mas/pxl)
MAVIS	370-950	30"x30"	4076x4076	7.36

Table 2.10: MAVIS camera main properties.

- E-ELT: The *European Extremely Large Telescope* is an optical/near-infrared ground-based telescope, whose main characteristic is the 39 m diameter of the primary mirror. Its main purpose is to study the first galaxies in the Universe, thanks to an adaptive optic system,

---

[11] https://mavis-ao.org/mavis/

known as MORFEO[12] (*Multiconjugate adaptive Optics Relay For ELT Observations*), which will allow other instruments, such as MICADO[13] (*Multi-AO Imaging Camera for Deep Observations*), to reach the diffraction limit of the telescope and to take high resolution images. Hence, MICADO, with the support from MORFEO, will spatially resolve star formation clumps of less than 300 pc diameter in galaxies at $z \sim 3$, reaching a spatial resolution considerably increased with respect to even JWST. It will allow to probe the high-redshift Universe and the earliest phases of galaxy formation, in addition to studying planetary systems and the Local Universe, which could also be partially resolved into individual stars. Its main properties are listed in Table 2.11.

Instrument	Spectral range (μm)	FoV	Array size	Pixel scale (mas/pxl)
MICADO	0.8–2.4	50.5”x50.5”	9x4096x4096	4

Table 2.11: MICADO main properties.

The high angular resolution achieved with adaptive optic systems such as the ones described for VLT and E-ELT could enable follow-up observations of those sources previously discovered in wide surveys. Besides, MAVIS and E-ELT are also expected to work in synergy, as they reach comparable angular resolution in the optical and in the infrared bands respectively.

Figure 2.12 shows how a simulated source would appear when observed by HST, ELT, JWST and MAVIS.

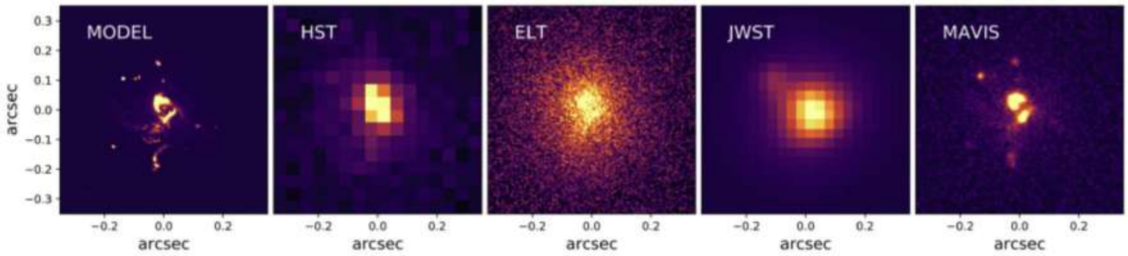

Figure 2.12: Comparison of how a $z = 5$ source (a) would appear when observed for a fixed exposure time (1h) by the HST (b), the ELT's MICADO (c), the JWST's NIRCam (d) and the VLT's MAVIS (e).

This Thesis explores how future instruments, such as Euclid and MICADO, will enable us to study highly amplified sources in order to answer to the main scientific problems previously discussed. The following chapters will describe how this research could be conducted through the use of image simulations and how these simulations could test the performance of methods employed for the morphological analysis of sources.

---

[12] https://elt.eso.org/instrument/MAORY/

[13] https://elt.eso.org/instrument/MICADO/

Chapter 3

Simulations of clumpy galaxies

In this Chapter, we describe the methodology employed to simulate clumpy galaxies and their observations with various instruments. We implemented the procedure in a set of functions, now part of a multi-purpose lensing library called PyLensLib (34), and in a Python code, which uses these functions.

3.1 Modeling the sources

Our goal is to simulate lensing of distant, star-forming galaxies, possibly hosting multiple star clusters (including primordial globular clusters).

One approach to model these sources is through cosmological numerical hydrodynamical simulations (11). While this is the most realistic method to understand how primordial galaxies and their star clumps form in a cosmological context, these simulations have very high computational costs and do not allow to tweek the parameters of the simulated sources. If one aims at investigating a large set of sources, particularly to test and validate analysis tools and pipelines, such simulations are not ideal.

In this Section, we describe an alternative approach to generate clumpy sources for lensing image simulations. We model these sources using multiple luminous components, whose brightness profiles are described by analytical functions. Specifically, we use the Sérsic model, given by:

$$I(R) = I_e e^{-b(n)\left[\left(\frac{R}{R_e}\right)^{\frac{1}{n}}-1\right]}, \tag{3.1.1}$$

where I_e is the surface brightness at the effective radius R_e, n is the Sérsic index and b is a function of the Sérsic index well approximated by $b(n) = 2n - \frac{1}{3} + \frac{4}{405n}$. Figure 3.1 shows how the shape of the Sérsic profile varies as a function of n. On average, bulges and elliptical galaxies have the steepest central profiles, with $2 < n < 10$, disks have exponential profiles with $n \sim 1$. Bars have flatter central profiles with $n \leq 0.5$, while the peculiar case with $n = 0.5$ corresponds to a Gaussian brightness profile, often used to describe stellar clumps.

This alternative approach, therefore, allows us to build even complex simulations in relatively short times and to control all the sources parameters, so that we can modify them to match the observations.

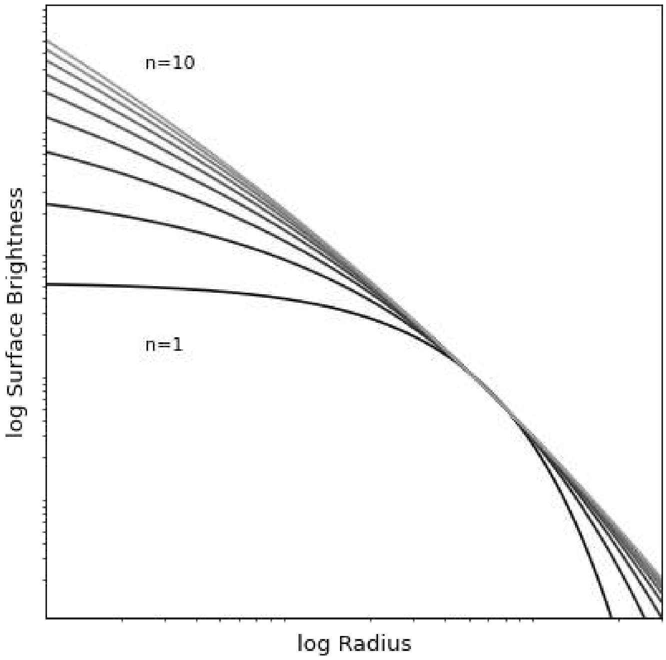

Figure 3.1: Sérsic profiles for different values of n (15). On average, bulges and elliptical galaxies have $2 < n < 10$, disks $n \sim 1$, bars $n \leq 0.5$ and stellar clumps $n = 0.5$.

3.1.1 The Host Galaxies

The first problem we consider is how to model the surface brightness distribution of the host galaxy. We assume that distant galaxies can be well approximated with exponential disks. Thus, we use Sérsic profiles with $n = 1$. Other parameters describing the host galaxies are the effective radius R_e, the flux f, the axis ratio q, the position angle φ, the intrinsic positions $\beta_{s,1}$ and $\beta_{s,2}$, and the redshift z_s.

When drawing a source on a pixellated image, the brightness is evaluated at every pixel position (β_1, β_2). Formally, the Sérsic profile extends to infinity; however, due to its rapidly decreasing behavior, we can safely avoid evaluating it at the pixels that are located sufficiently far from the source center $(\beta_{s,1}, \beta_{s,2})$ to save computational time. This approach is useful when simulating large fields-of-view, which may include more than a single source. In this case, we set the limit for computing the brightness at 100 times the source effective radius.

To account for the galaxy center and position angle, we operate a translation and a rotation of the reference frame where the brightness is computed according to the following equations:

$$\begin{aligned} \beta_1' &= (\beta_1 - \beta_{s,1}) \cos\varphi + (\beta_2 - \beta_{s,2}) \sin\varphi, \\ \beta_2' &= -(\beta_1 - \beta_{s,1}) \sin\varphi + (\beta_2 - \beta_{s,2}) \cos\varphi\,, \end{aligned} \tag{3.1.2}$$

where (β_1', β_2') are the new pixel coordinates.

Then, we account for the source ellipticity, parametrized through the axis ratio q, by computing the *elliptical* radius, given by

$$R = \sqrt{\left(\frac{\beta_1'}{q}\right)^2 + (\beta_2')^2}\,. \tag{3.1.3}$$

Finally, we compute the pixel brightness inserting the radius R into Eq. 3.1.1.

In Figure 3.2, we show an example of a Sérsic galaxy at redshift $z_s = 1.036$, simulated using the abovementioned method. In this case, the galaxy center coincides with the center of the field-of-view, the position angle is $\varphi = \pi/8$, counted counter-clockwise with respect to the vertical axis, and the axis ratio is $q = 0.5$. The input flux can be provided in arbitrary units. In this example, we use counts s^{-1}. Thus, the brightness is evaluated at each pixel in units of counts s^{-1} pixel^{-1}.

3.1.2 The Stellar Clumps

Once created the galaxy, we populate it with stellar clumps according to some recipes that will be discussed in this Section. The brightness distributions of the clumps are modeled exactly as described for the host galaxy, i.e. as Sérsic sources.

To model the population of stellar clumps for a given host galaxy, we make the following assumptions:

1. the clump spatial distribution follows the underlying brightness distribution of the host;
2. the flux in clumps is a predetermined fraction of the total flux of the host;
3. the distribution of clump fluxes obeys a Schechter-like function (47);
4. the clump size is a growing function of the clump flux.

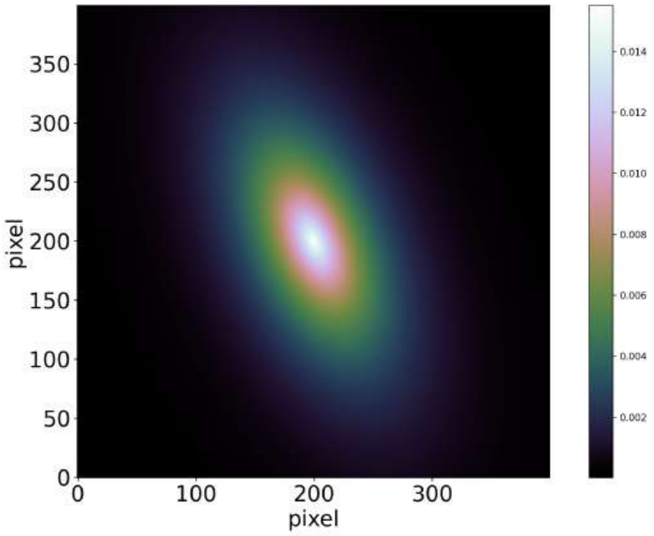

Figure 3.2: A model of a Sérsic host galaxy. Details on the adopted parameters are reported in the text. The colorbar is in units of [counts/sec].

While our modelization is extremely flexible, the model parameters discussed below should be set to match observations. Unfortunately, the statistical properties of stellar clumps in distant, high-redshift galaxies are not well constrained (see e.g. 36). For this reason, we will use observations of local galaxies as *mild* references. Of course, the similarity of these sources to their high-redshift equivalents is not guaranteed. The simulation tools that we have developed will help clarifying this issue in a future study.

Firstly, we constrain the clumps overall number, considering that only a fraction Q of the host galaxy total flux goes into star clumps. This fraction varies with the morphological classification of a galaxy: it is reasonable to assume $Q = [0 - 0.05]$ for early-type, lenticular galaxies, $Q = [0.2 - 0.4]$ for late-type galaxies (41). In fact, we expect late-type galaxies to be characterized by a stronger star formation and to host more star forming regions compared to early type galaxies. Here we simulate sources with exponential disks, assuming a fraction $Q = 0.2$.

As explained earlier, we assume that the clump fluxes follow a distribution which is a generalization of a Schechter model:

$$f(x) = x^{\beta} e^{-\delta\left(\frac{x}{x_{cut}}\right)^{\gamma}}, \tag{3.1.4}$$

where x and x_{cut} respectively are the clump, and the characteristic luminosities (fluxes) normalized to the total galaxy luminosity (or equivalently, flux), while β, δ and γ are the parameters defining the shape of the luminosity function. Compared to a pure Schechter function, this distribution combines a power-law trend with a logarithmic slope β at low luminosities with an exponential cut-off above a characteristic scale x_{cut}. Still, it is defined through two more parameters, δ and γ, which control the shape of the function at $x > x_{cut}$. This parametrization of the clump luminosity function is mutuated from cosmological hydrodynamical simulations of galaxy formation and evolution (e.g. 19) and can be adapted to observations of local galaxies (e.g 1), which are

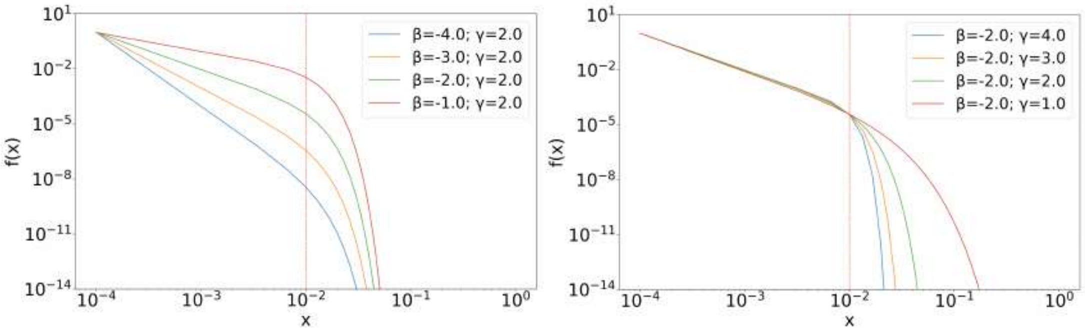

(a) **(b)**

Figure 3.3: The clump luminosity function features a power law trend at low luminosities and an exponential cut-off at $x > x_{cut}$ (highlighted by the dashed vertical red line). x and $f(x)$ are represented in arbitrary units, as they are normalized quantities: $f(x)$ is normalized such that $f(1e-4) = 1$, while x is the clump luminosity in units of the galaxy luminosity. The two panels show the effect of changing the parameter β while maintaining fixed γ (left) and viceversa (right).

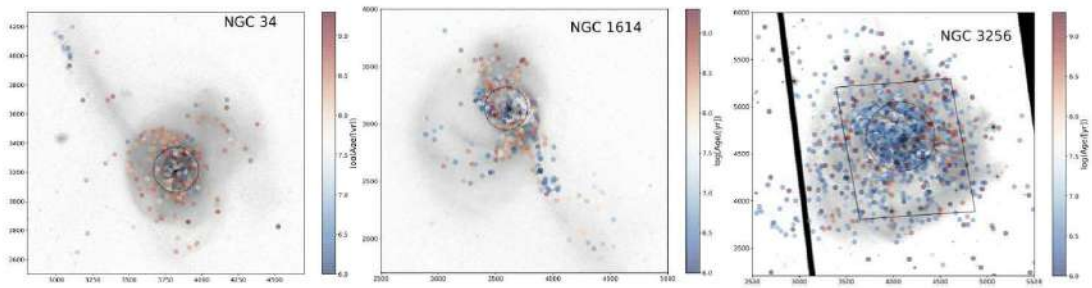

Figure 3.4: In the local Universe the positions of stellar clumps follow the surface brightness distribution of their host galaxies, as we assume in this work; in this Figure, the clumps are colored accordingly to their ages (1).

consistent with setting $\beta = -2$, $\delta = 1.0$, and $\gamma = 2.0$. Furthermore, we assume $x_{cut} = 0.01$. Panel (a) of Figure 3.3 shows how the parameter β controls the slope of the power-law trend, while panel (b) highlights the role of γ in steepening the exponential cut-off.

To assign to each clump a proper luminosity/flux, we use the following method. First, we normalize the cumulative luminosity function $F(x)$ such that $F(x_{min}) = 1$. We assume $x_{min} = 10^{-4}$. Then, we generate random values of $F(x)$ in the interval $[0 - 1]$. We invert the function $F(x)$ in order to compute the flux value x corresponding to the generated value of F. We repeat the procedure until we saturate the flux budget in stellar clumps, as defined by the parameter Q. Our assumption on x_{min} implies that no clumps with luminosity/flux $< x_{min}$ will be generated.

To conserve the total galaxy flux, we subtract from the host flux the sum of the clump fluxes.

Then, we have to define the clump positions. We assume their spatial distribution follows the surface brightness distribution of the host galaxy, as resulting from studies on local galaxies

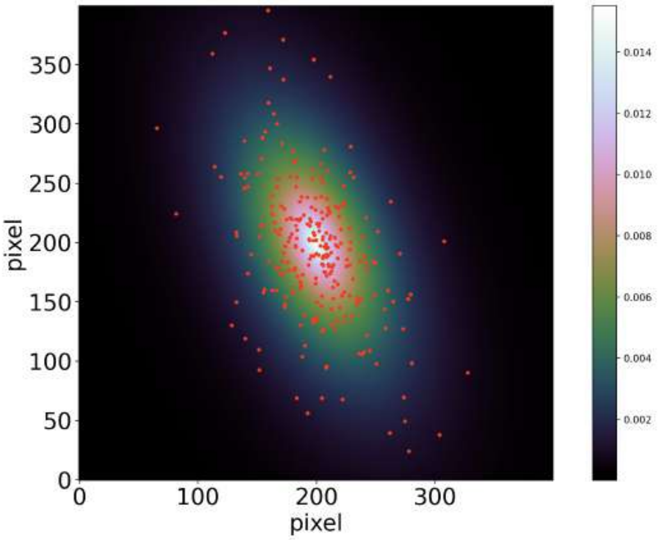

Figure 3.5: Example of a clump distribution inside a Sérsic galaxy. It follows the surface brightness of the galaxy itself. The colorbar is in units of [counts/sec].

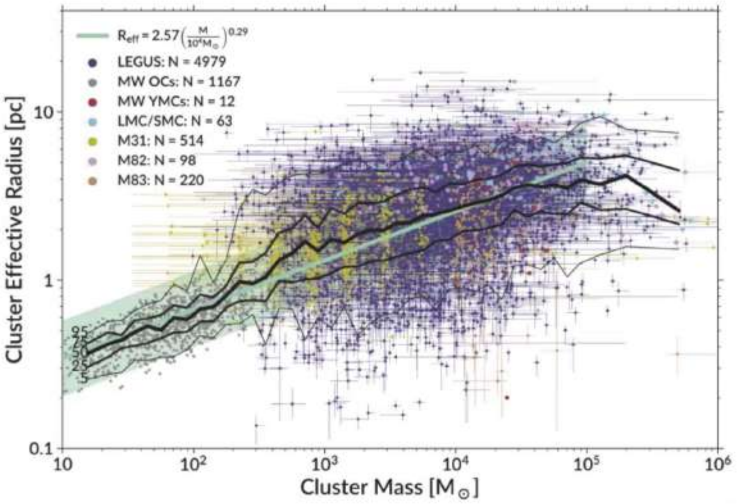

Figure 3.6: Relation between the effective radius and the stellar mass, found in the local Universe ((10)) and used in this work to estimate plausible clump dimensions.

(Figure 3.4). We show our corresponding result in Figure 3.5. To achieve this goal, we implement a procedure similar to that used to generate the clump luminosities. The smooth brightness map of the host is flatten into a one-dimensional array, whose elements are numerated by indexes. The indexes identify the pixels in the 2D-map, and the corresponding surface brightness assigns a probability to each pixel. The `numpy` package includes a function called `random.choice` that can be used to sample one-dimensional arrays using the abovementioned method.

Regarding the stellar clumps size distribution, we rely on a relation between the effective radius R_{eff} and the stellar mass M, found in the local Universe (10):

$$R_e = 2.57\left(\frac{M}{10^4 M_\odot}\right)^{0.29} . \tag{3.1.5}$$

This relation is shown in Figure 3.6.

Up to now, each clump is characterized by a value of flux or luminosity. To use this relation, we must assign to each clump a stellar mass. We assume a fixed mass-to-light ratio $M/L \sim 1$ for simplicity. We stress again that this parameter can be changed in our model to explore alternative scenarios. Figure 3.7 shows how the clump size varies as a function of the clump normalized flux. In particular, we define the clump size both in terms of arcseconds and parsec. Clearly, in order to compute the correct conversion between these units, we have to know the source redshift (here, $z = 1.036$) and assume a given cosmology. In this work, we consider a flat cosmology with $\Omega_M = 0.3$, $\Omega_\Lambda = 0.7$, and $H_0 = 70$ km s^{-1} Mpc^{-1}.

Regarding the Sérsic index n_{cl}, we establish all the clumps follow a Gaussian brightness profile ($n_{cl} = 0.5$). Finally, for the position angle φ_{cl} we assume a uniform distribution in the range [0, π). We further assume that the distribution of the axis ratios q_{cl} is uniform in the range [0.3, 1).

Panel (a) of Figure 3.8 shows the same galaxy of Figure 3.2 after the inclusion of the stellar clumps described by our nominal model. Panels (b) and (c) show the same galaxy populated with clumps following a luminosity function with $\beta = -1$ and $\beta = -4$, respectively.

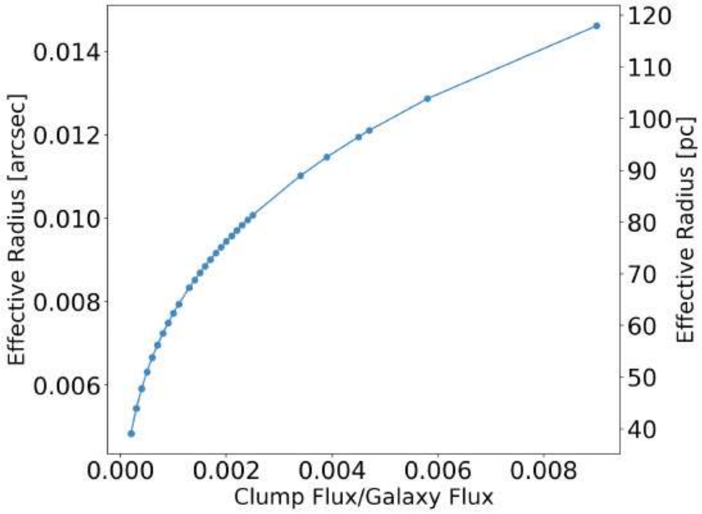

Figure 3.7: The clump sizes in arcseconds and parsecs as a function of the clump normalized flux.

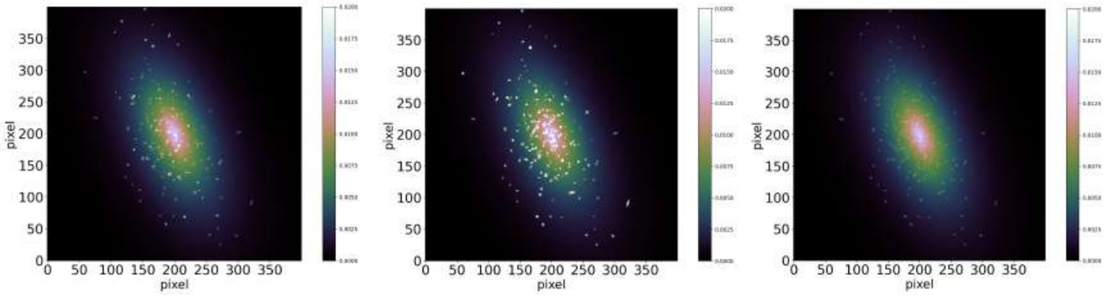

(a) **(b)** **(c)**

Figure 3.8: Three models of a Sérsic host galaxy, populated with Sérsic stellar clumps. In (a) the clump luminosity follows a luminosity function with $\beta = -2$, while in (b) $\beta = -1$ and in (c) $\beta = -4$. The colorbar is in units of [counts/sec].

3.1.3 Adding colors

The host galaxy and clumps are also characterized by a Spectral Energy Distribution (SED). This enables us to assign colors to the sources and to simulate multi-band observations.

The SED templates used in this Thesis were previously constructed using stellar population synthesis techniques by (4). They are shown in Figure 3.9. Our code is very flexible in terms of the SEDs that can be associated to the host and clumps. Depending on the user's choice, these SEDs can be set or chosen randomly by the software. We also built a function that creates new intermediate SEDs by interpolating between SED pairs. Clearly, the SEDs are redshifted, according to the source redshift, using Eq. 2.2.1.

The SED allows us to compute the fluxes in any photometric bands. For a given pass-band $F(\lambda)$, the flux for a source with SED $S(\lambda)$ is

$$f_\lambda = \frac{\int S(\lambda)F(\lambda)\lambda d\lambda}{\int F(\lambda)\lambda d\lambda} \ . \tag{3.1.6}$$

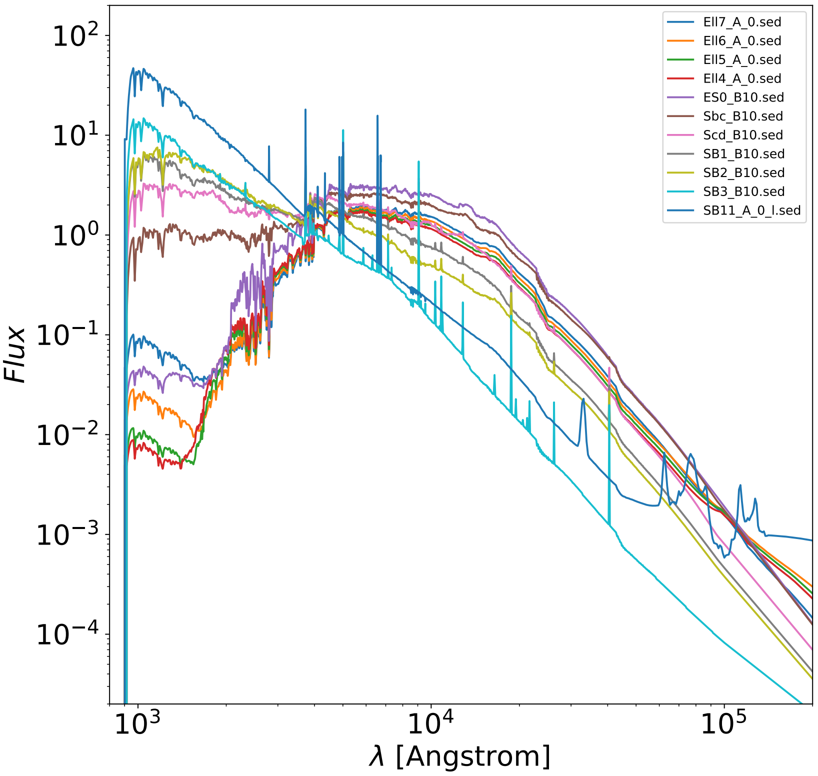

Figure 3.9: SED models used in this Thesis. The models range from SEDs typical of elliptical galaxies (Ell*) to SEDs of starburst sources (SB*).

The flux is in units of erg s^{-1} cm^{-2} Å^{-1}. The SEDs in Figure 3.9 can be normalized to return a specific flux in a reference band. Then, using Eq. 3.1.6, we can compute the fluxes in other bands.

In Figure 3.10, we show two examples of clumpy galaxies with $R_e = 1''$ at $z_s = 1$. The parameters of the host and clumps are identical in the two cases. However, in the left and right panels we use a redder and a bluer SED for the host, respectively. Specifically, the redder galaxy has a SED randomly chosen among the Ell4-7 templates. On the contrary, the bluer galaxy has a SED obtained by interpolating the Sab-Scd templates. For the star clumps, we adopt SEDs typical of starburst objects in both panels. To create these models, we use $Q = 0.1$. We produce images in three HST pass-bands (F435W, F606W, and F814W) and combine them to create the RGB images.

Finally, in Figure 3.11, we show the same galaxy shown in Figure 3.10, simulated with two different values of Q and SEDs. In the left panel, the host galaxy is redder, and we assume $Q = 0.02$. On the contrary, we use a bluer SED and assume $Q = 0.2$ to simulate the galaxy in the right panel.

For the examples shown in the following sections, since we are particularly interested in simulating young galaxies at high redshift, we use SEDs typical of spiral objects for the galaxy hosts, selecting them randomly. Regarding the star clumps, we repeat the same operation, but, as done

Figure 3.10: RGB images of a clumpy galaxy at $z = 1.0$. The images show two simulations of the same galaxy populated with stellar clumps assuming $Q = 0.1$. However, the SEDs used to model the host galaxies are different. In the left and right panels, we use a redder (Ell-type) and a bluer (Sbc-Scd) SED, respectively. The size of each image is $5''$.

in the previous example, with SEDs typical of starburst objects.

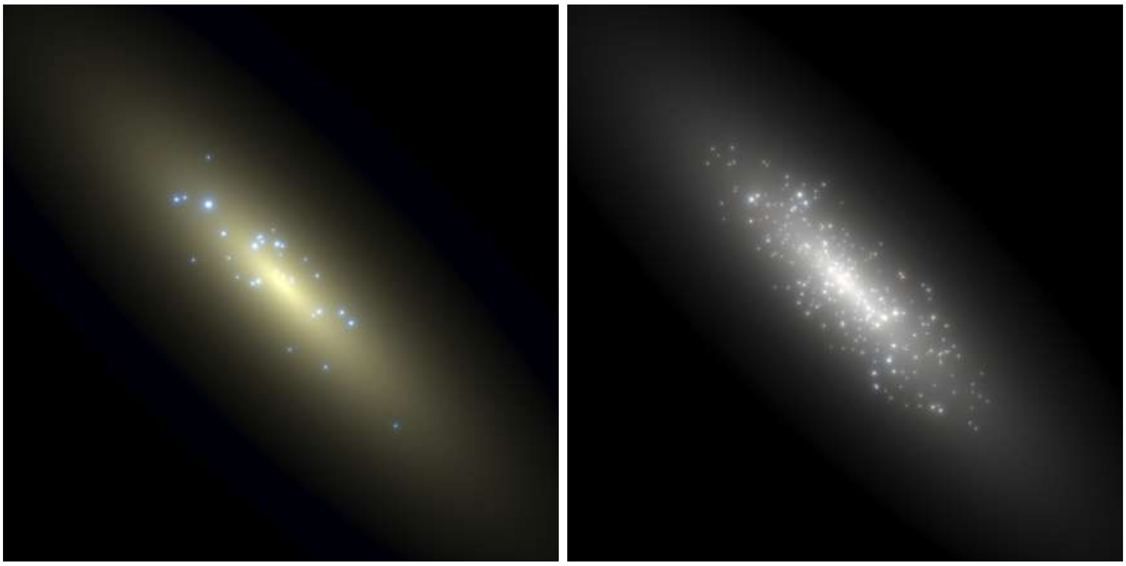

Figure 3.11: RGB images of clumpy galaxies with different SEDs and Q parameters. The images show the same galaxy as in Figure 3.10, but simulated with $Q = 0.02$ and $Q = 0.2$, respectively. The size of each image is $5''$.

3.2 Simulating lensing effects

In this section, we discuss how we apply lensing effects to the sources generated with our model. We consider lensing by galaxy clusters, but the procedure to simulate lensing effects by galaxies is identical.

3.2.1 Lens Models

Since galaxy clusters are characterized by virial masses $M_{vir} \sim 10^{15} M_{\odot}$, they are the strongest gravitational lenses in the Universe. Therefore, building models of real clusters turns out to be of extreme relevance. These models can be generated through the public software `Lenstool` ((25), (23), (22)), which follows a parametric approach, as described in (7) and (40). More precisely, the total mass distribution of the cluster is decomposed into several components, each characterized by a set of parameters. The mass distribution is, then, constrained minimizing a χ^2 function, which quantifies the discrepancy between model and observations. In particular, the χ^2 function takes into account the difference between observed multiple images and their model-predicted positions:

$$\chi^2(\vec{\xi}) = \sum_{j=1}^{N_{fam}} \sum_{i=1}^{N_{im}^j} \left(\frac{\left|\left| \vec{x}_{ij}^{obs} - \vec{x}_{ij}^{pred}(\vec{\xi}) \right|\right|}{\Delta x_{i,j}} \right)^2 , \tag{3.2.1}$$

where $\vec{x}_{ij}^{obs}$ and $\vec{x}_{ij}^{pred}(\vec{\xi})$ are the observed and predicted positions of the i-th multiple image of the j-th background source, while $\vec{\xi}$ is the totality of free parameters of the system.

In this Thesis we consider five different galaxy clusters as gravitational lenses: MACS J1206.2-0847 ($z = 0.44$), MACS J0416.1-2403 ($z = 0.396$), Abell S1063 ($z = 0.348$), PSZ 1G311.65-18.48

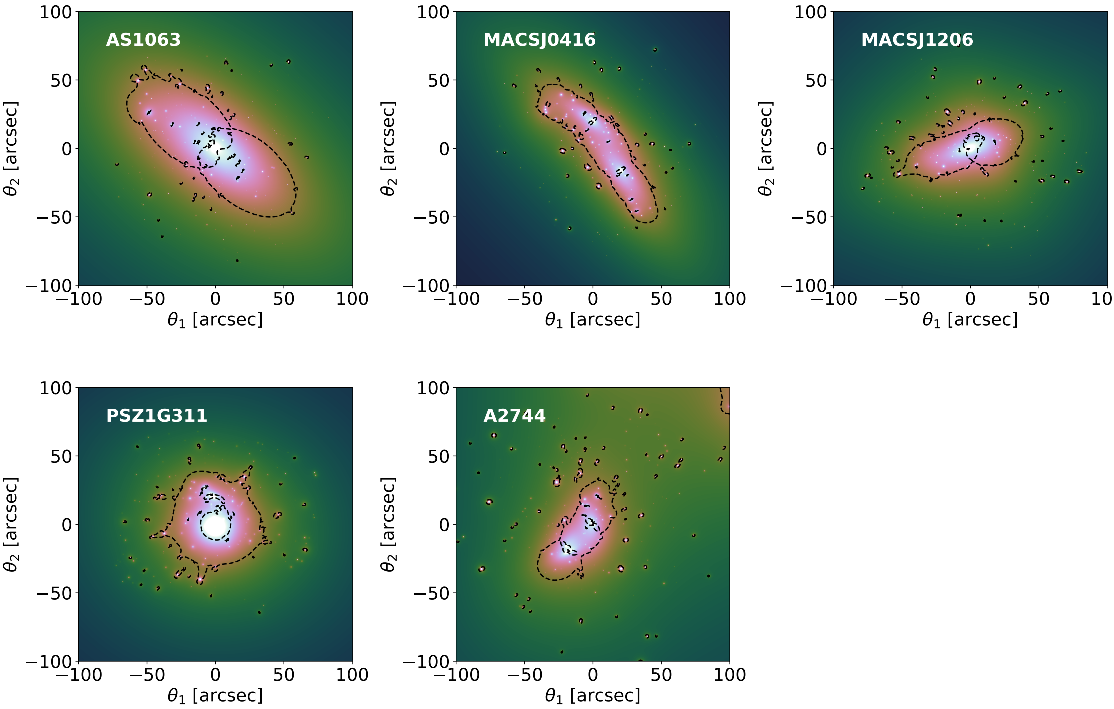

Figure 3.12: Lens models for the five galaxy clusters considered in this Thesis: Abell S1063 (5), MACS J0416.1-2403 (6), MACS J1206.2-0847 (5), PSZ1G311.65-18.48 (40), and Abell 2744 (7). These models are generated with the software `Lenstool`. The dashed lines highlight the radial and tangential critical lines associated to a source at $z \sim 6$.

($z = 0.4436$), and Abell 2744 ($z = 0.308$). The details of the mass modeling can be found in several papers (5; 6; 7; 40). Here, we only show the resulting mass maps in Figure 3.12.

To use the lens models for applying lensing effects to the clumpy sources, we use a class of the pyLensLib library called `deflector`. This class contains several functions to compute lensing quantities such as, the deflection angle, convergence, and shear maps at every position on the lens plane. It also contains functions to draw critical lines and caustics, and to perform ray-tracing between the lens and the source planes. For example, the black dashed lines in Figure 3.12 show the lens critical lines of PSZ 1G311.65-18.48 for $z_s = 6$.

In practice, we create a `deflector` instance reading the deflection angle maps $\alpha_1(\theta_1, \theta_2)$ and $\alpha_2(\theta_1, \theta_2)$ created by `Lenstool`. All the information required to execute this task are stored inside the `best.par` file, which contains all the best-fit parameters of the cluster lens model produced by `Lenstool`.

It is worth noting that the `Lenstool` maps are computed for a single source redshift, $z_{S,ref}$. To compute the deflection angle maps for any other source redshift z_S, we need to rescale the maps by multiplying them by the *family ratio*,

$$\Xi(z_L, z_S, z_{S,ref} = \frac{D_{LS}(z_L, z_S)}{D_S(z_S)} \frac{D_S(z_{S,ref})}{D_{LS}(z_l, z_{S,ref})} \ . \tag{3.2.2}$$

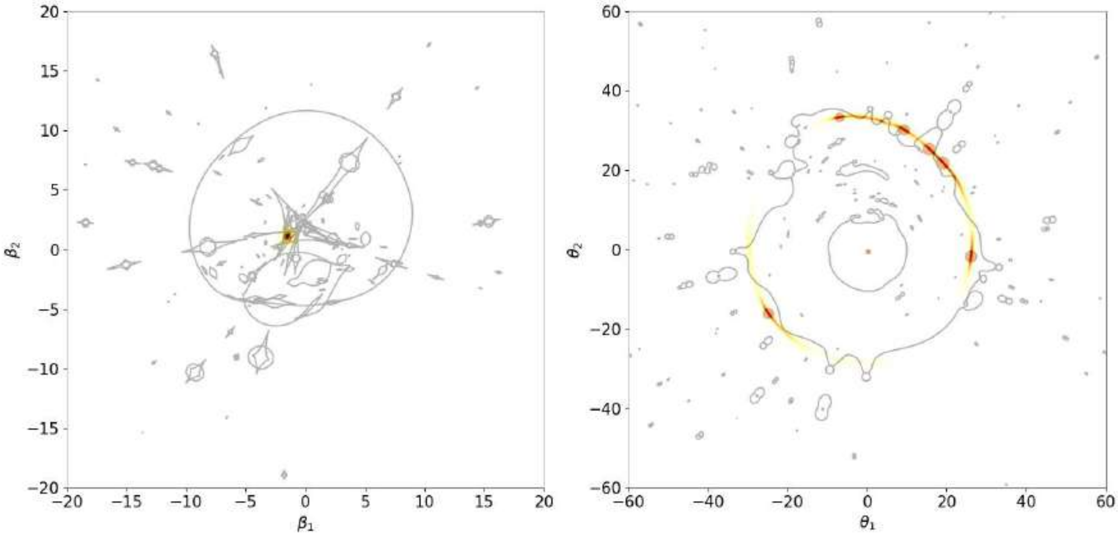

Figure 3.13: Caustics (on the left) and critical lines (on the right) of PSZ1G311.65-18.48. We show how a source located near to a caustic is distorted into a highly magnified set of gravitational arcs. The red circles mark the multiple positions of the images of the source center in the arc.

3.2.2 Lensed images

For a given source with surface brightness $I_s(\beta_1, \beta_2)$, we can derive the surface brightness of its lensed image(s) by means of ray-tracing. This technique consists of tracing bundles of light rays through the lens plane at positions (θ_1, θ_2), where the deflection angles can be read off the deflection angle maps, $\alpha_1(\theta_1, \theta_2)$ and $\alpha_2(\theta_1, \theta_2)$. Then, the arrival position of each ray on the source plane, can be derived from the lens equation in Eq. 1.2.1, as

$$\begin{aligned} \beta_1 &= \theta_1 - \alpha_1(\theta_1, \theta_2) \\ \beta_2 &= \theta_2 - \alpha_2(\theta_1, \theta_2) \; . \end{aligned} \tag{3.2.3}$$

The image surface brightness is finally computed as

$$I(\theta_1, \theta_2) = I_s(\beta_1, \beta_2) \; , \tag{3.2.4}$$

using the fact that lensing conserves the surface brightness.

As said, from the `deflector`, we can derive the lens caustics and critical lines. In particular, analysing the caustics, we can identify the points on the source plane where we should place a source to produce lensed images with the desired shape and spatial extent. For example, the left panel of Figure 3.13 shows in grey the very intricate network of caustics of the cluster PSZ1G311 for $z_s = 2.3$. We place a yellow/red source at a particular position with respect to the caustics, and, as shown in the right panel, we obtain a very extended, almost complete, Einstein ring. This image resembles very closely the so called *Sunburst* arc, observed in this galaxy cluster (43) (40).

Using a similar approach, we identify specific positions on the source plane where we can place sources tailored to produce lensed images with the desired shape. As an example, in Figure 3.14, we show how the source in Figure 3.8 looks like if placed at $z = 1.036$ and lensed by the cluster MACS J1206.2-0847. The source is also shown in colors in the left panel. Since we chose a position near a tangential caustic, the source appears deformed into a tangential gravitational arc with a counter image in the right panel. Note that 1) the lensed images cover a field-of-view much larger than the instrinsic source area; and 2) the blue stellar clumps in the image are also lensed and multiply imaged inside the arcs. More realistic simulations of similar sources will be presented later in this Chapter.

3.3 Inclusion of observational noises

This Section illustrates the main steps aimed at adding the proper observational noise and instrumental contamination to the previously generated noise-free images.

In this Thesis we simulate observations of the clumpy galaxies with several space observatories (HST, JWST, Euclid). The procedure we follow is the same for all of them and consists of the following steps:

1. we draw the surface brightness distribution on a pixel grid resembling the image detector;

Figure 3.14: Strong lensing simulation of a clumpy galaxy. The RGB image in the left panel shows an unlensed source mimicking a red galaxy with bluer stellar clumps and corresponding to the monochromatic source displayed in Figure 3.8. The side-length of the image is $4''$. This source is located at $z = 1.036$ and, if placed near the cluster tangential caustic, is distorted into a gravitational arc and a smaller counter image, shown in the right panel. The side-length of this figure is much larger: $40''$.

2. we convert the source surface brightness into units of counts s^{-1} pixel^{-1};
3. we convolve with the resulting image with the instrument Point-Spread-Function (PSF);
4. we add the sky background;
5. we add photon noise.

We do not consider other instrumental effects such as Charge Transfer Efficiency (CTE) or Brighter Fatter (BF) effects, neither we simulate cosmic rays, radiation damage, hot pixels, etc. We assume that these effects are corrected in the images we produce.

We begin with assigning a magnitude (in a reference band) to the source we want to simulate. As explained earlier, we can compute the magnitudes in any other band knowing the source SEDs (for both the host and the clumps).

Using the instrument Zero-Point (ZP), we convert the magnitude into a total number of counts (or data numbers, DN) s^{-1}. The ZP of an instrument, by definition, is the magnitude of an object that produces one DN per second. The magnitude of an object producing DN counts in an observation of length t_{exp} is, therefore:

$$m_{\mathrm{AB}} = 2.5 \log_{10}\left(\frac{\mathrm{DN}}{t_{exp}}\right) + \mathrm{ZP}_{\mathrm{AB}} \ , \tag{3.3.1}$$

where AB denotes that we work with AB magnitudes. The DN s^{-1} are obtained by inverting the formula above, which yields:

$$\frac{\mathrm{DN}}{t_{exp}} = 10^{-0.4(m_{\mathrm{AB}} - \mathrm{ZP}_{AB})} \ . \tag{3.3.2}$$

We scale the brightness distribution of the source such that the total number of DN s^{-1} corresponds to the value derived from Eq. 3.3.2 for the desired input magnitude.

In the next step, we consider the Point Spread Function (PSF) of the chosen instrument. We apply it to the image of the clumpy galaxy in units of DN s^{-1} pixel^{-1} via a two-dimensional convolution:

$$\tilde{I}(\theta_1, \theta_2) = \int \int d\theta_1' d\theta_2' I(\theta_1', \theta_2) \mathrm{PSF}(\theta_1 - \theta_1', \theta_2 - \theta_2') \ . \tag{3.3.3}$$

In practice, we perform this convolution using the function `signal.convolve` from the Python package `scipy`[1].

The sky background (bkg hereafter) in an astronomical observation depends on several factors, including the direction into which the observation is carried out. In our code, we set the background level according to the signal-to-noise ration (sn) for a point source of a given magnitude m_{lim} inside a circular aperture of radius r_{ap} and area $A_{ap} = \pi r_{ap}^2$, containing N_{pix} pixels. In this case, the background in units of DN s^{-1} pixel^{-1} is given by the equation

$$\mathrm{bkg}[\mathrm{DN}s^{-1}\mathrm{pixel}^{-1}] = \left\{ (C_{lim}[\mathrm{DN}s^{-1}])^2 \times t_{exp}/sn^2 - C_{lim}[\mathrm{DN}s^{-1}] \right\} / N_{pix} \ , \tag{3.3.4}$$

where C_{lim} is the number of DN s^{-1} corresponding to the magnitude m_{lim}.

Finally, the photon noise is computed on the pixel grid assuming it is Poisson distributed with variance given by the sum of the source and background counts. The simulated, sky-subtracted observations are obtained by summing the noise maps and the PSF-convolved source images. More details about this procedure can be found in several papers (35; 41).

3.4 Preparing the Virtual Observations

It is worth noting that the whole process described here can be applied to sources placed anywhere behind the cluster. However, we limit ourselves to give just some examples: only three sources for each gravitational lens, identical in size and shape, and we locate them in very peculiar points of the source plane, namely near to the caustics.

Table 3.1 lists all the parameters to model the clumpy host galaxies shown in the examples of simulated observations. In particular, some sources are conceived to reproduce, once lensed, real arcs and arclets observed in the clusters whose models are used to simulate the lensing effects. In particular, we refer to the re-known Cosmic Snake Arc in MACS J1206.2-0847 (13), the Sunburst Arc in PSZ 1G311.65-18.48 (44), and the System 3 in Abell 2744 (7). These sources are particularly interesting for the stellar clumps they contain. In (14), for instance, they identify from the CLASH images of MACS J1206.2-0847 24 clumps in the counterimage and 55 in the Cosmic Snake, for a total of 79 clumps. In (43), instead, analysing HST images of the Sunburst Arc, they discover that this arc is a single galaxy, lensed into at least 12 multiple images. Finally, regarding System 3 in Abell 2744, three star-forming clumps are identified in (50).

---

[1] `https://docs.scipy.org/doc/scipy/reference/generated/scipy.signal.convolve.html`

The positions of the remaining sources are chosen to reproduce images with different levels of magnification and distortion.

Cluster	Source	n	Re (arcsec)	q	ϕ	$\beta_{s,1}$ [arcsec]	$\beta_{s,2}$ [arcsec]	mag	z_S
MACS J1206.2-0847	1	1.0	0.3	0.5	$\pi/8$	5.099	2.1588	20	1.036
	2	1.0	0.3	0.5	$\pi/8$	-9.184	-5.167	20	2.5
	3	1.0	0.3	0.5	$\pi/8$	12.177	3.1457	20	4.0
MACS J0416.1-2403	1	1.0	0.3	0.5	$\pi/8$	-10.132	2.127	20	1.0
	2	1.0	0.3	0.5	$\pi/8$	-10.408	0.823	20	2.5
	3	1.0	0.3	0.5	$\pi/8$	-14.122	3.96	20	4.0
Abell S1063	1	1.0	0.3	0.5	$\pi/8$	11.668	-9.411	20	1.0
	2	1.0	0.3	0.5	$\pi/8$	-22.387	15.825	20	2.5
	3	1.0	0.3	0.5	$\pi/8$	-15.3807	8.441	20	4.0
PSZ 1G311.65-18.48	1	1.0	0.3	0.6	$-\pi/8$	-1.7149	0.8985	20	2.3702
	2	1.0	0.3	0.6	$\pi/8$	0.129	1.55	20	1.0
	3	1.0	0.3	0.6	$\pi/8$	-1.408	2.89	20	4.0
Abell 2744	1	1.0	0.3	0.4	$-\pi$	28.395195	40.2729467	20	3.98
	2	1.0	0.3	0.4	$\pi/8$	16.5237	29.898	20	1.0
	3	1.0	0.3	0.4	$\pi/8$	9.862	17.09	20	2.5

Table 3.1: Keywords used to model the sources as Sérsic galaxies. For every source we specify the Sérsic index (n), the effective radius (Re), the axis ratio (q), the position angle (ϕ), the source position (βs1 and βs2), the source magnitude (mag), and redshift (z_s).

As said, all lensed sources are observed with three instruments/cameras, namely HST/ACS, JWST/NIRCAM and Euclid/VIS. These instruments are characterized by different pixel scales and PSFs. Some details are given here below:

HST/ACS The native pixel size of the ACS WFC camera on-board the HST is $0.0495''$/pxl. We generate the PSF models in different bands using the public PSF modeling tool `Tiny Tim` (27). This software models the diffraction, and all the aberrations and obscurations in the HST optical system. In addition, it considers the focus displacements the telescope experiences during its operational life and which are caused by the desorption and the so called *breathing*. The first one induces a long-term focus change which is corrected moving the secondary mirror every six months. The breathing, instead, is associated to the thermal effects the telescope experiences during an orbit. In principle, all these effects can be accounted for in our simulations by changing the PSF model depending on the case of interest (time, position on the CCD, etc). However, here we generate a single PSF per pass-band and we use it in all our simulations.

More specifically, `Tiny Tim` is composed of three programs: `tiny1`, `tiny2`, and `tiny3`. `tiny1` asks a series of questions that define the observation, including which detector and filter are requested, the sub-sampling relative to the default HST/ACS pixel scale, the PSF diameter, the spectrum of the simulated star, etc. Based on these parameters it determines the appropriate grid sizes for drawing the PSF model, it multiplies the stellar spectrum by the filter curve, and outputs the results along with the instrument parameters and the aberrations in a parameter file for the next step, which is executed by `tiny2`. This second program computes the PSF. More specifically, it produces a series of monochromatic PSFs in the wavelength range of the filter, and it adds them together, weighing by the system transmission and stellar spectrum. Finally `tiny3` applies the geometric distortions of the ACS camera.

We simulate observations in the bands F435W, F606W, and F814W. We request $sn = 10$ for a point source of magnitude $m_{lim} = 24$ in a circular aperture of radius $r_{ap} = 1''$. The exposure time is estimated basing on these parameters using the HAST ACS Exposure Time Calculator[2].

JWST/NIRCAM We simulate observations in the imaging mode of the JWST NIRCAM through the short-wavelength channel (0.6-2.3 μm) in the bands F090W, F150W, and F200W. The pixel scale in this case is $0.031''$/pxl. The PSF models were taken from (41), who generated them using the WEBBPSF tool[3]. We use the same constraints as in the HST simulations for defining the background level[4].

Euclid/VIS In the case of Euclid, we simulate observations only in the *riz* band with the VIS instrument. The pixel scale is $0.1''$/pxl. The NISP imager, which observes in the NIR bands Y, J, and H, has too coarse spatial resolution ($0.3''$/pxl) to enable studies of stellar clumps in distant sources. Thus we do not simulate observations in these bands, although our code easily could do it. A model of the Euclid VIS PSF was provided by members of the strong lensing working group within the Euclid Consortium. In the case of Euclid, we followed the prescriptions for the wide survey of 15,000 sq. deg that the mission will perform during a period of 6 years. Details about the suvery strategy can be found in (18). Euclid is expected to reach a limiting magnitude $m_{lim} = 24.5$ (for extended sources) at $sn = 10$ with a total exposure time of $2280s$.

Table 3.2 lists the background levels and exposure times estimated for HST/ACS, JWST/NIRCAM and Euclid/VIS in all bands considered.

Instrument	Filter	texp (s)	bkg CR (counts/s)
ACS	F435W	1160.28	57.40
	F606W	598.55	180.79
	F814W	1125.46	149.07
NIRCAM	F090W	2168.83	10.17
	F150W	1095.15	10.44
	F200W	880.42	9.59
VIS	*riz*	2280.0	2.52

Table 3.2: Exposure times and background count rates for HST/ACS and JWST/NIRCAM in different filters.

---

[2] https://etc.stsci.edu/etc/input/acs/imaging/

[3] https://www.stsci.edu/jwst/science-planning/proposal-planning-toolbox/psf-simulation-tool

[4] https://jwst.etc.stsci.edu

3.5 Simulation gallery

In this Section we present a gallery of simulated observations obtained with our simulation pipeline. For each source in Table 3.1 we show:

1. the unlensed source models in Figure 3.16 (hereafter, we name the 15 sources considering the corresponding letter in this Figure);
2. the relative positions of the sources and the corresponding images with the respect to the lens caustics and critical lines, respectively (Figures 3.17, 3.22, 3.26, 3.30, 3.34);
3. the lensed images, both as noise-free, high-resolution images, and as simulated observations with Euclid, HST, and JWST. In the case of the Euclid simulations, we show virtual observations only in the VIS band. On the contrary, the simulated observations with the other instruments are shown as RGB images obtainened by combining observations in the F814W, F606W, and F435W bands in the case of HST, and in the F200W, F150W, and F090W bands in the case of JWST;

These sources are lensed by the following galaxy clusters, whose models were all previously generated with the software `Lenstool`, as described in Section 3.2.1:

- MACS J1206.2-0847: located at $z = 0.439$, it is one of the galaxy clusters observed in the CLASH program. The lens model we use in this Thesis was generated by (5). This cluster hosts the *Cosmic Snake Arc*, which we try to reproduce in our simulations;
- MACS J0416.1-2403: placed at z = 0.3960, it is one of the galaxy clusters observed in the CLASH program. The lens model we use in this Thesis was generated by (6);
- Abell S1063: located at $z = 0.348$, it is one of the galaxy clusters observed in the Hubble Frontier Fields program. The lens model we use in this Thesis was generated by (5);
- PSZ 1G311.65-18.48: placed at $z = 0.4436$, this cluster hosts the *Sunburst Arc*, which we try to reproduce in our simulations. The lens model we use in this Thesis was generated by (40);
- Abell 2744: located at $z = 0.3072$, it is one of the galaxy clusters observed in the Hubble Frontier Fields program. This cluster hosts a peculiar gravitational arc, named *System 3* in (7), who also generated the lens model we use in this Thesis.

Figure 3.15 shows the HST images of these five clusters.

Regarding the simulations, we begin with the cluster MACS J1206.2-084 and source A (Figure 3.16a, $z = 1.036$), as this latter has been our example until now. In Figure 3.18 we can see how it deforms when placed as shown in the top panel of Figure 3.17. In particular, it deforms into a very elongated arc, which is supposed to reproduce the Cosmic Snake Arc (14), and a more regular and less amplified counterimage. The arc is composed of two stretched multiple images whose parity is inverted, while the counterimage is placed in a region of less amplification and shows the

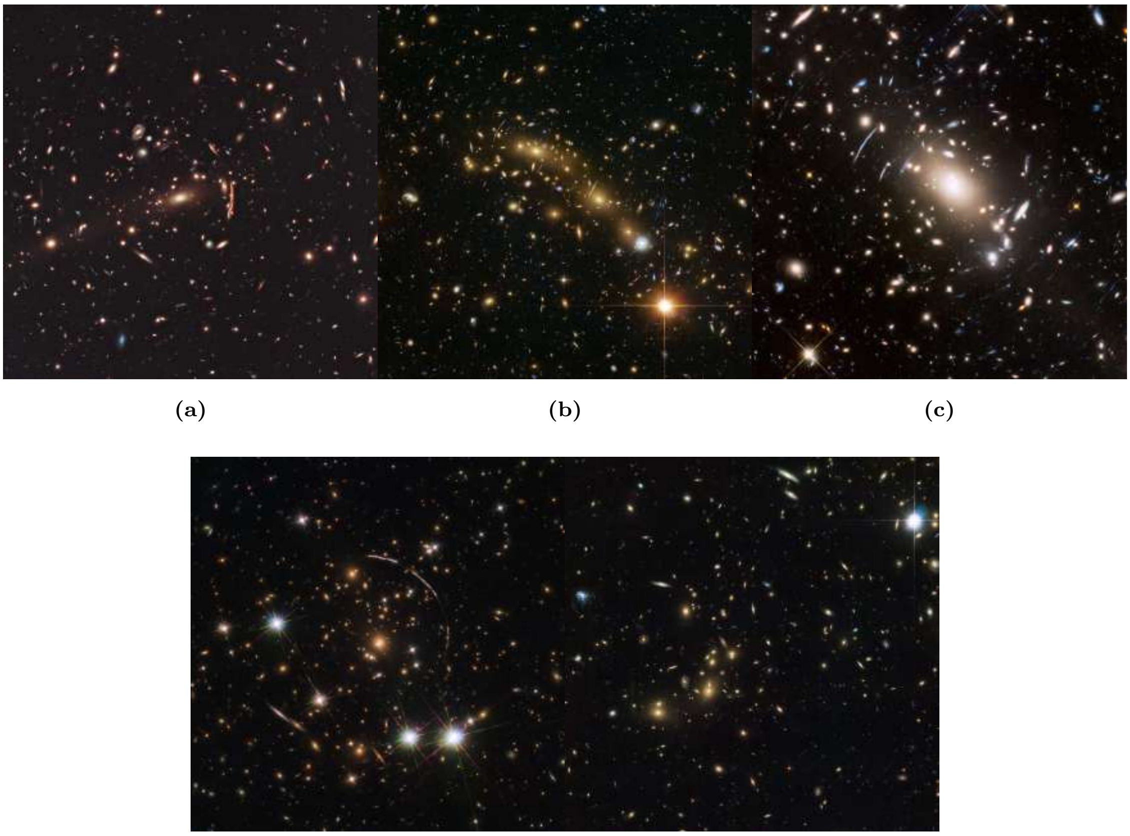

(a) (b) (c)

(d) (e)

Figure 3.15: (a) MACS J1206.2-0847, observed by M. Postman and the CLASH Team using HST-ACS/WFC and HST-WFC3/IR; (b) MACS J0416.1-2403, observed by the HST Frontier Fields Team using HST-ACS/WFC and HST-WFC3/IR; (c) Abell S1063, observed by the HST Frontier Fields Team using HST-ACS/WFC and HST-WFC3/IR; (d) PSZ1G311.65-18.48, observed by the HST with the instruments WFC3-UVIS, WFC3-IR and ACS-WFC; (e) Abell 2744, observed by the HST Frontier Fields Team using the intrument HST-ACS/WFC.

entire galaxy. The whole system extends in length for 40” over the lens plane. In Figure 3.19 we show three zooms-in over the arc and the counterimage, in order to better appreciate the difference in spatial resolution of the three instruments: while in the JWST zoom-in many stellar clumps are clearly visible, their number slightly decreases in the HST image and significantly decreases in the Euclid one. However, a more in-depth discussion will be held in the following Chapter. The other sources, B and C (Figure 3.16b, $z = 2.5$ - Figure 3.16c, $z = 4$), are placed where indicated in the central and bottom panel of Figure 3.17. The first is distorted into a very stretched arc, composed of two images of the source galaxy, and a less amplified counterimage. In (Figure 3.20) we only show the arc, where the two images are clearly visible in its extremities as brighter regions and which extends in length for 20”. The second, if placed as shown in the bottom panel of the same Figure 3.17, appears as a really elongated arc which is composed of just one image of the source galaxy (Figure 3.21). It extends for 40”.

Moving to the second cluster, MACS J0416.1-2403, Figure 3.22 shows the position of the three sources with respect to the caustics. In particular, source D (Figure 3.16d, $z = 1$) is distorted into a less extended (20”) arc, composed of just one image of the source galaxy (Figure 3.23); source E (Figure 3.16e, $z = 2.5$), on the other hand, generates three different objects covering 40” in length, namely a stretched arc, composed of five multiple images, and two less magnified counterimages, which are quite fine representations of the source galaxy (Figure 3.24); source F (Figure 3.16f, $z = 4$), instead, turns into a single very elongate gravitational arc, stretching for 40”. It is formed by a single image.

The three sources G (Figure 3.16g, $z = 1$), H (Figure 3.16h, $z = 2.5$) and I (Figure 3.16i, $z = 4$) are placed as shown in Figure 3.26 and lensed by Abell S1063. Source G, in particular, forms an arc of 30” made of just one single image (Figure 3.27). Sources H and I, instead, are distorted into an elongate arc, made of two images of the galaxy, and a less amplified counterimage (Figure 3.28 and Figure 3.29). The first system extends for 40”, while the second one for 30”.

Turning to PSZ1G311.65-18.4, the sources which this cluster lenses are J (Figure 3.16j, $z = 2.3702$), K (Figure 3.16k, $z = 1$) and L (Figure 3.16l, $z = 2.5$). Figure 3.30 illustrates their positions with respect to the caustics. In all three cases, the sources are deformed into very extended and almost complete Einstein Rings. In particular, source J generates a highly magnified gravitational arc (Figure 3.31), which is supposed to reproduce the Sunburst Arc (40) and extends over a region of 80”x80”. It is composed of 9 multiple images of the source galaxy. Similarly, source K is deformed into an arc formed by 5 multiple images covering 40”x40” on the lens plane (Figure 3.32), while source L appears as an arc extending over a region of 80”x80” composted of 3 multiple images (Figure 3.33).

Finally, Figure 3.34 shows where we place the three sources lensed by Abell 2744. They are source M (Figure 3.16m, $z = 3.98$), N (Figure 3.16n, $z = 1.0$) and O (Figure 3.16o, $z = 2.5$). The first one is distorted into two objects: an arc extending for about 20”, shown in Figure 3.35, and a less amplified counterimage. The arc, which is supposed to reproduce the System 3 (7), is made of two multiple images of the source galaxy whose parities are inverted. Then, source N generates an arc, formed of two multiple images and extending for 20” on the lens plane, and a counterimage (Figure 3.36). Lastly, source O generates a single, but very stretched gravitational arc, which extends for 40” and hosts at least two multiple images of the galaxy (Figure 3.37).

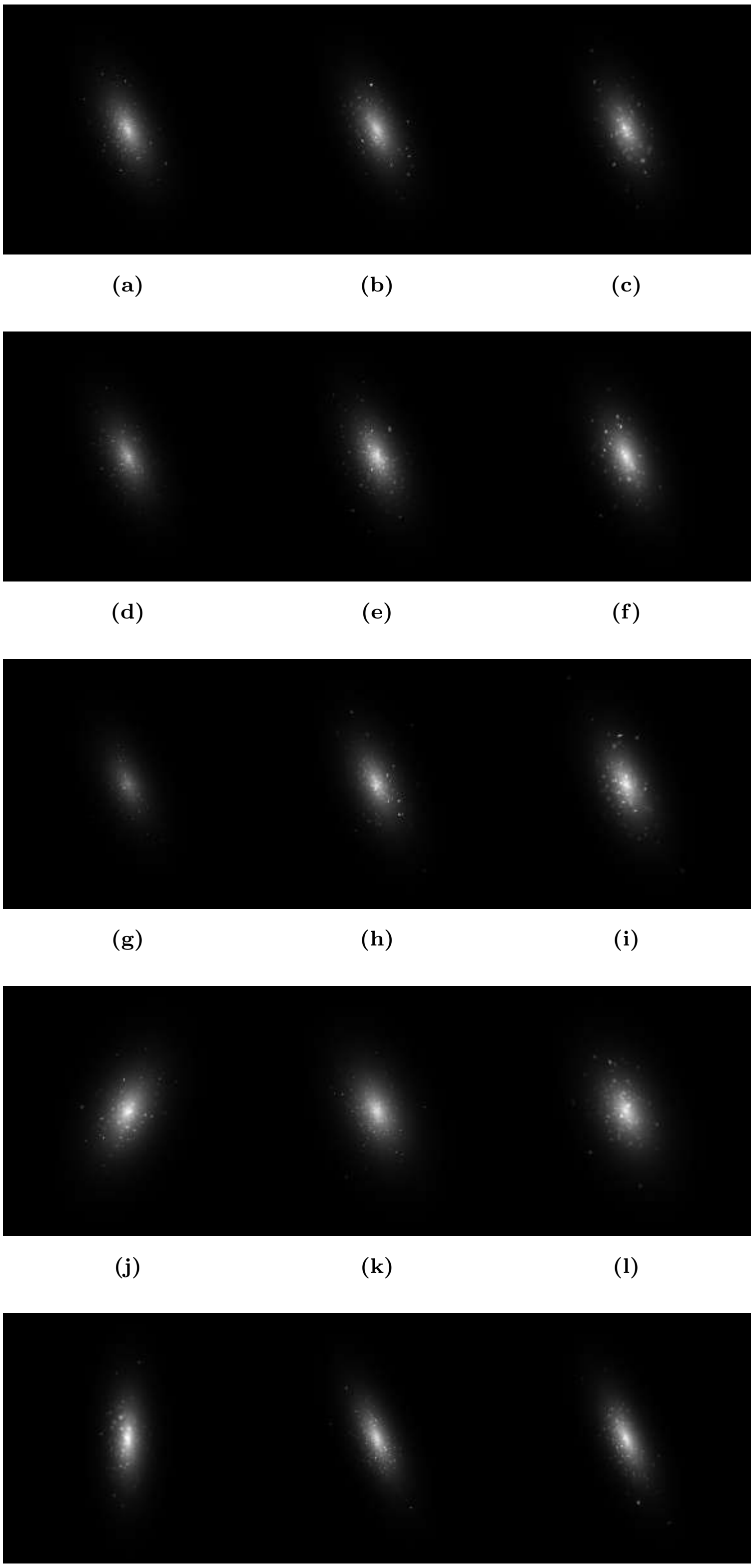

(a) **(b)** **(c)**

(d) **(e)** **(f)**

(g) **(h)** **(i)**

(j) **(k)** **(l)**

(m) **(n)** **(o)**

Figure 3.16: The unlensed representation of the sources which will be lensed by the five galaxy clusters. In particular, (a), (b) and (c) will be lensed by MACS J12062-0847; (d), (e) and (f) by MACS J0416.1-2403; (g), (h) and (i) by Abell S1063; (j), (k) and (l) by PSZ1G311.65-18.48; (m), (n) and (o) by Abell 2744. The model parameters used to build these sources are listed in Table 3.1.

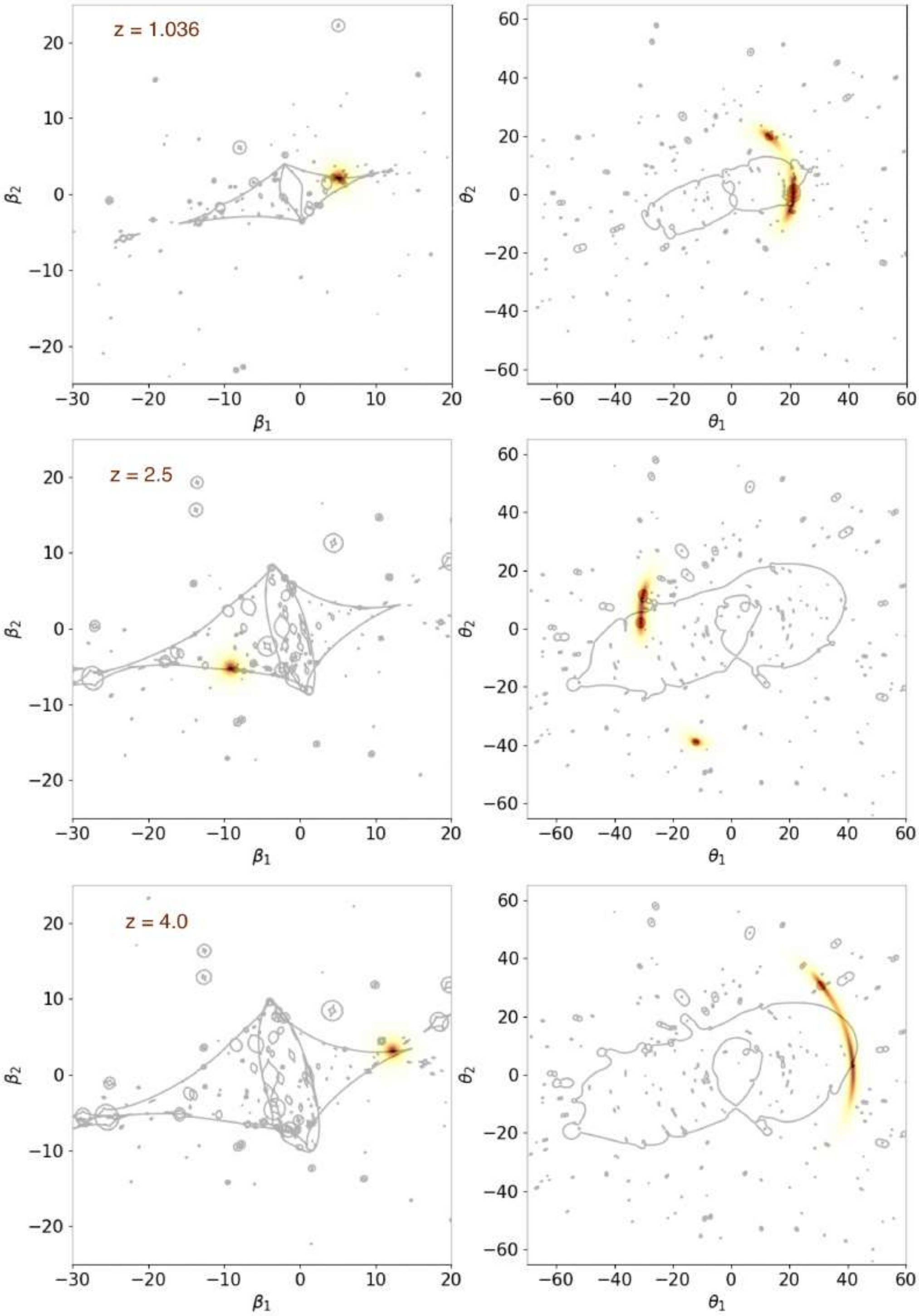

Figure 3.17: Caustics (on the left) and critical lines (on the right) of MACS J12062-0847 for three sources located at z = 1.036, z = 2.5 and z = 4, respectively, such as (a), (b) and (c) in Figure 3.16. We place these sources on the source plane in correspondence of the red-yellow point and they are distorted into highly magnified gravitational arcs. The red circles mark the positions of the multiple images.

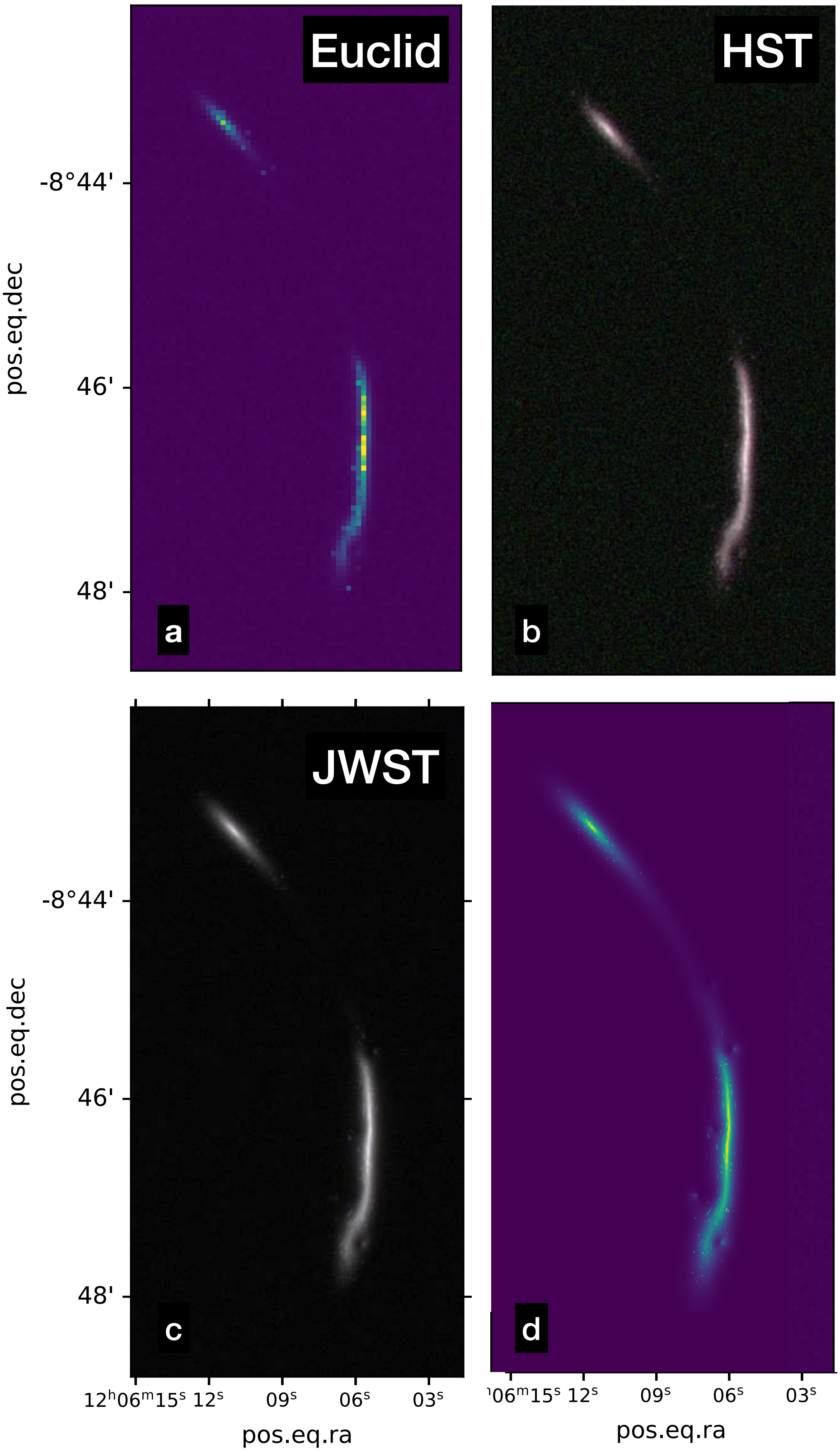

Figure 3.18: MACS J1206.2-0847, source A (z = 1.036): (a) simulation produced with Euclid/VIS (0.1 arcsec/pix); (b) simulation produced with HST-ACS (0.05 arcsec/pix) using the filters F814W, F606W, and F435W; (d) simulation produced with JWST-NIRCAM (0.031 arcsec/pix) using the filters F200W, F150W and F090W; (d) noise-free simulation (0.003 arcsec/pix). This source is supposed to reproduce the Cosmic Snake Arc.

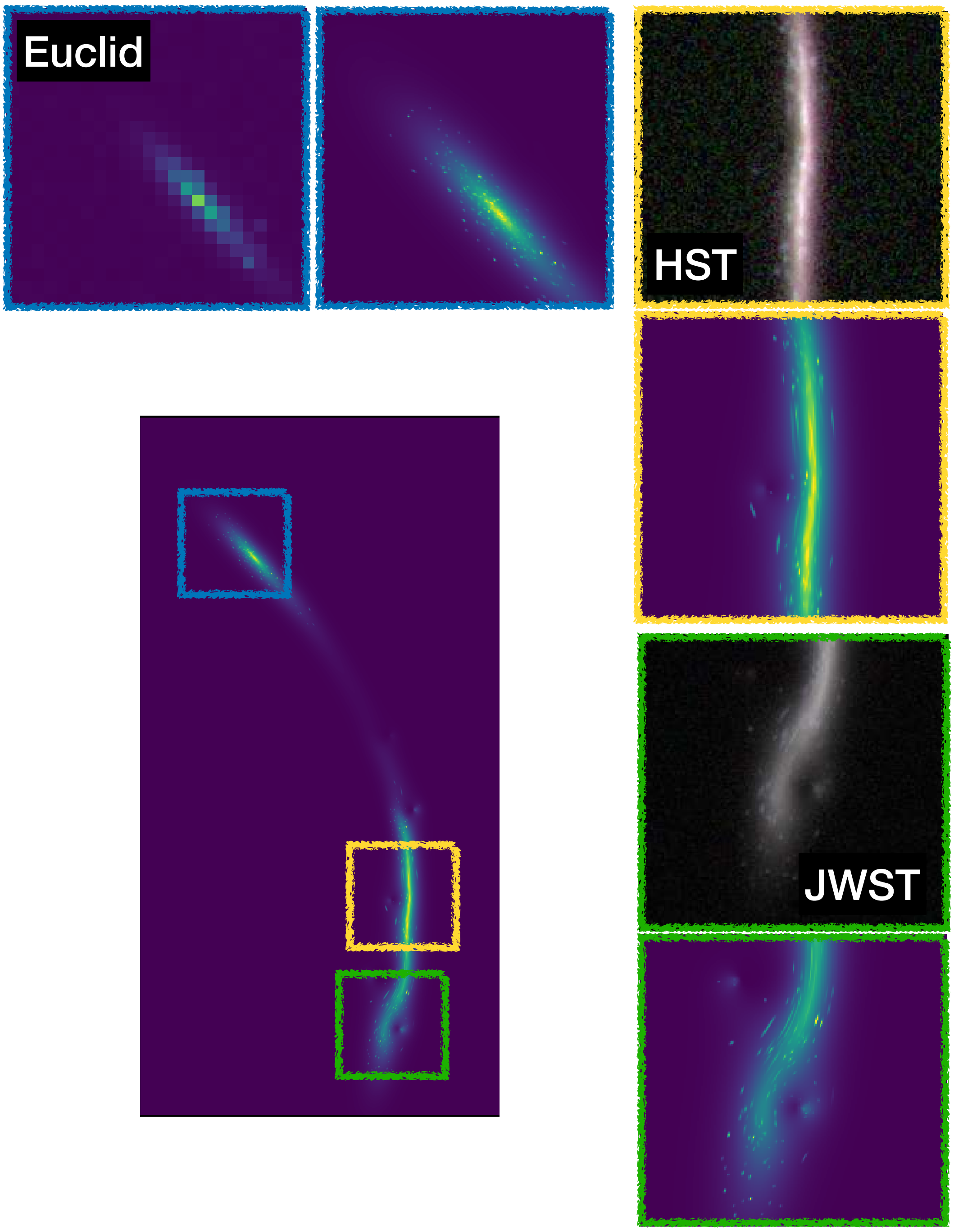

Figure 3.19: MACS J1206.2-0847, source A: a zoom-in comparison between the same sectors of the gravitational arc as seen by the three instruments.

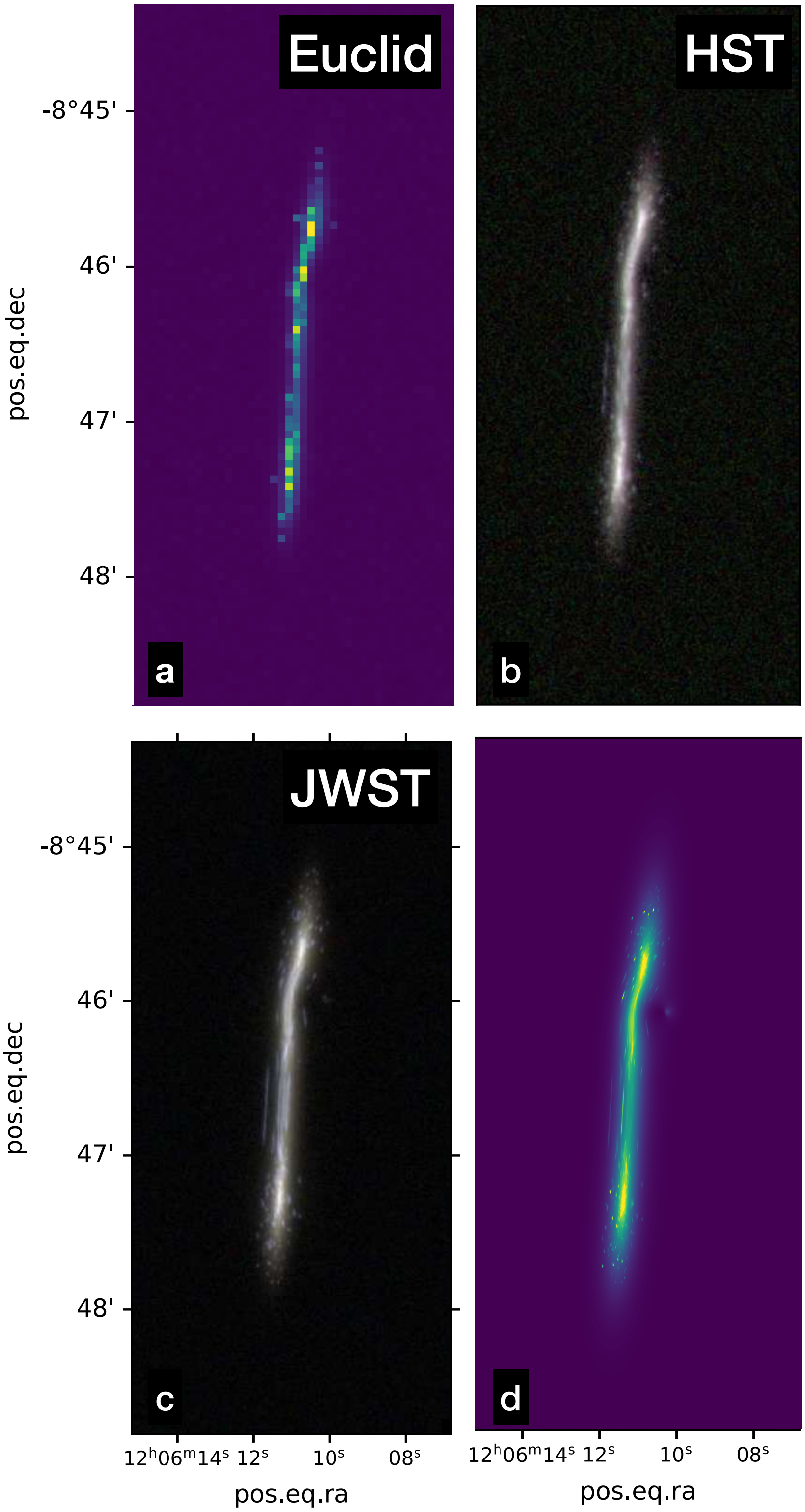

Figure 3.20: MACS J1206.2-0847, source B ($z = 2.5$): (a) simulation produced with Euclid/VIS (0.1 arcsec/pix); (b) simulation produced with HST-ACS (0.05 arcsec/pix) using the filters F814W, F606W, and F435W; (d) simulation produced with JWST-NIRCAM (0.031 arcsec/pix) using the filters F200W, F150W and F090W; (d) no noise simulation (0.003 arcsec/pix).

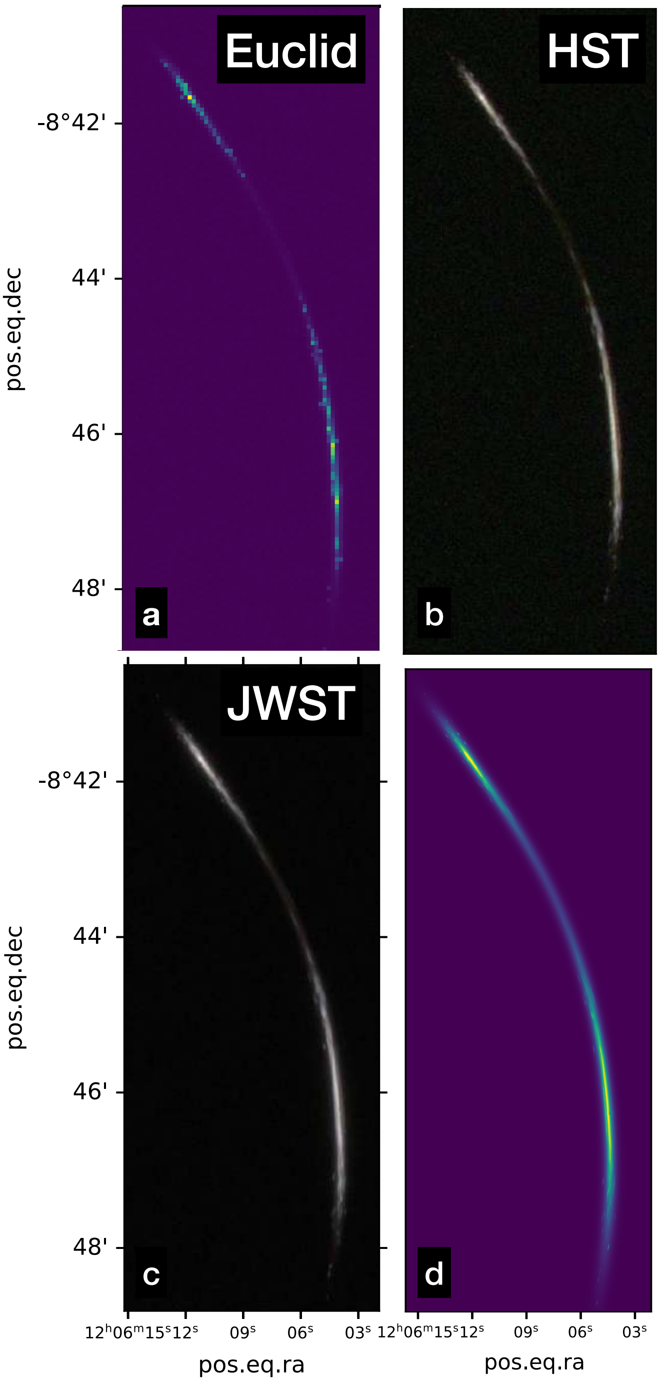

Figure 3.21: MACS J1206.2-0847, source C ($z = 4$): (a) simulation produced with Euclid/VIS (0.1 arcsec/pix); (b) simulation produced with HST-ACS (0.05 arcsec/pix) using the filters F814W, F606W, and F435W; (d) simulation produced with JWST-NIRCAM (0.031 arcsec/pix) using the filters F200W, F150W and F090W; (d) no noise simulation (0.003 arcsec/pix).

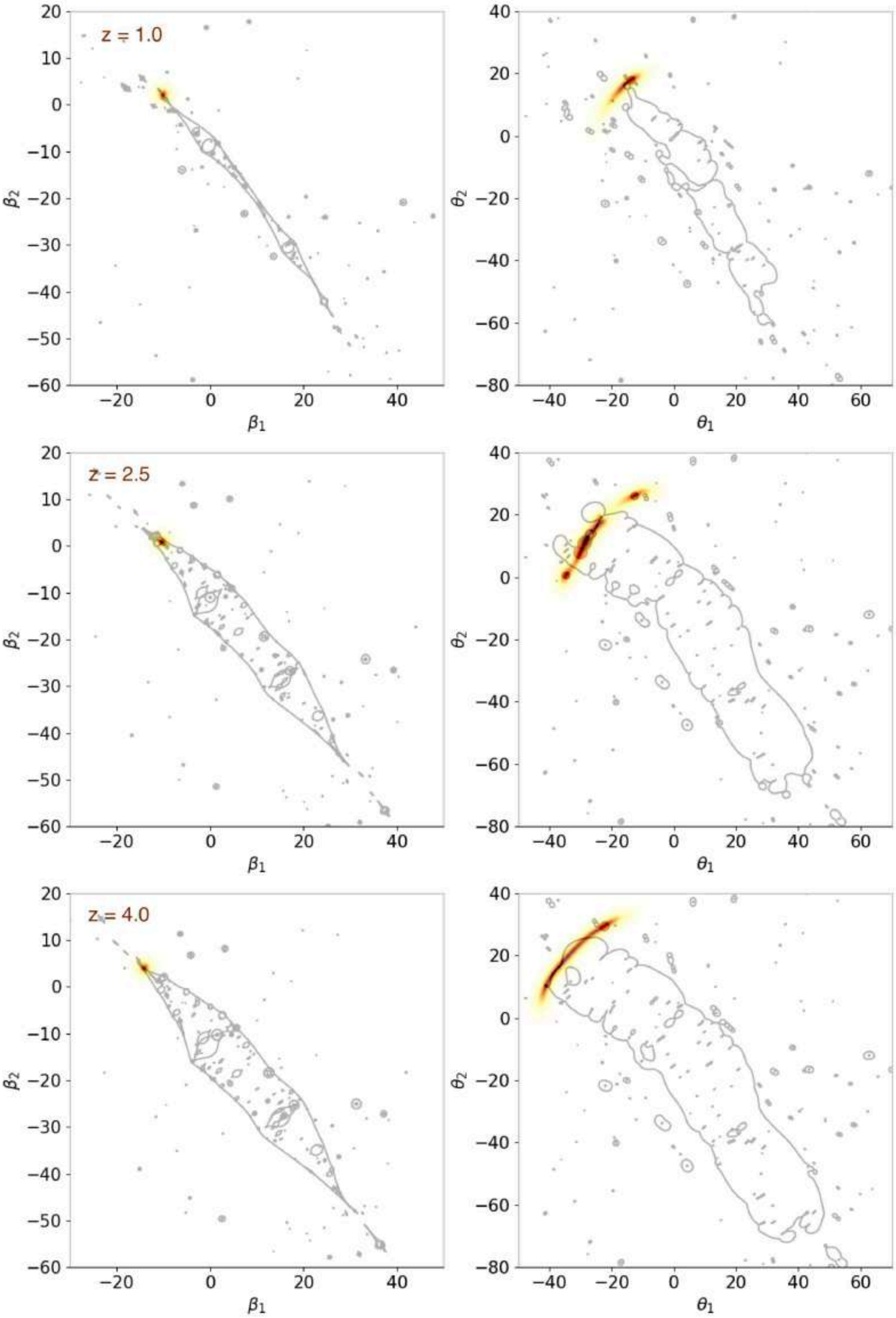

Figure 3.22: Caustics (on the left) and critical lines (on the right) of MACS J0416.1-2403 for three sources located at $z = 1.0$, $z = 2.5$ and $z = 4$, respectively, such as (d), (e) and (f) in Figure 3.16. We place these sources on the source plane in correspondence of the red-yellow point and they are distorted into highly magnified gravitational arcs. The red circles mark the positions of the multiple images.

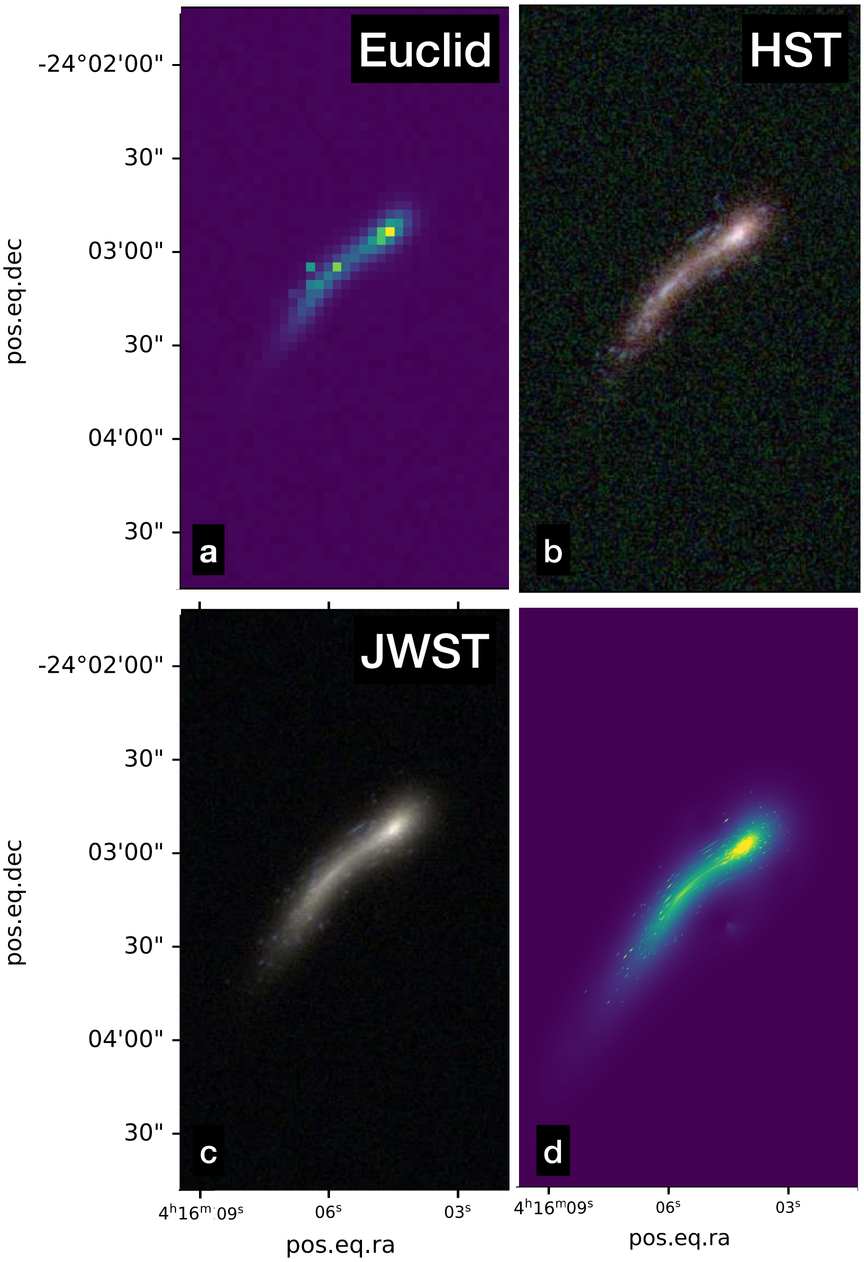

Figure 3.23: MACS J0416.1-2403, source D ($z = 1$): (a) simulation produced with Euclid/VIS (0.1 arcsec/pix); (b) simulation produced with HST-ACS (0.05 arcsec/pix) using the filters F814W, F606W, and F435W; (d) simulation produced with JWST-NIRCAM (0.031 arcsec/pix) using the filters F200W, F150W and F090W; (d) no noise simulation (0.003 arcsec/pix).

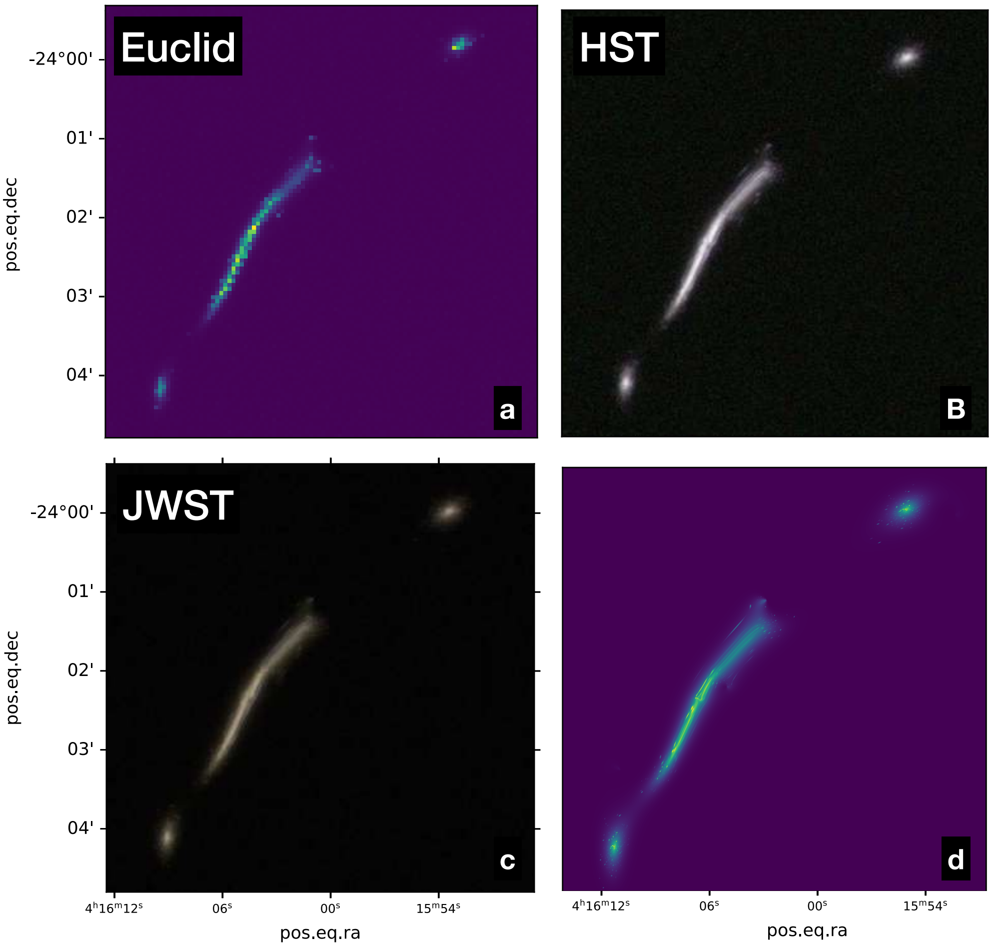

Figure 3.24: MACS J0416.1-2403, source E ($z = 2.5$): (a) simulation produced with Euclid/VIS (0.1 arcsec/pix); (b) simulation produced with HST-ACS (0.05 arcsec/pix) using the filters F814W, F606W, and F435W; (d) simulation produced with JWST-NIRCAM (0.031 arcsec/pix) using the filters F200W, F150W and F090W; (d) no noise simulation (0.003 arcsec/pix).

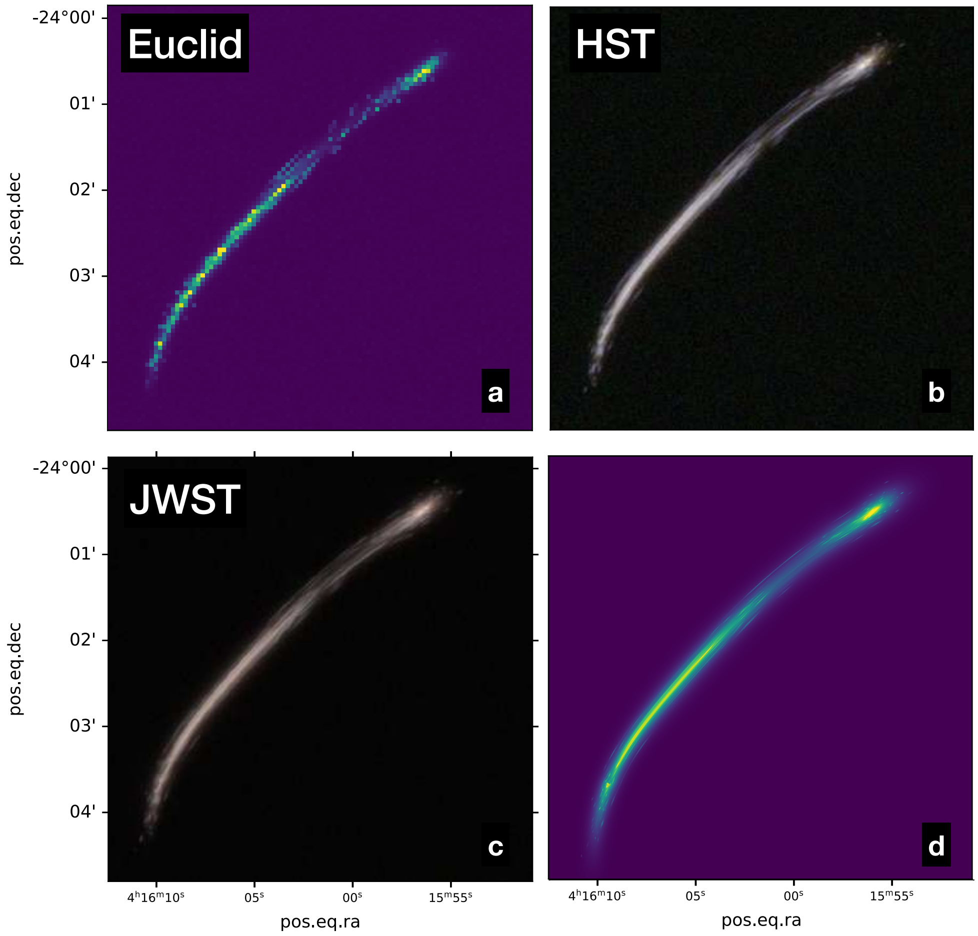

Figure 3.25: MACS J0416.1-2403, source F ($z = 4$): (a) simulation produced with Euclid/VIS (0.1 arcsec/pix); (b) simulation produced with HST-ACS (0.05 arcsec/pix) using the filters F814W, F606W, and F435W; (d) simulation produced with JWST-NIRCAM (0.031 arcsec/pix) using the filters F200W, F150W and F090W; (d) no noise simulation (0.003 arcsec/pix).

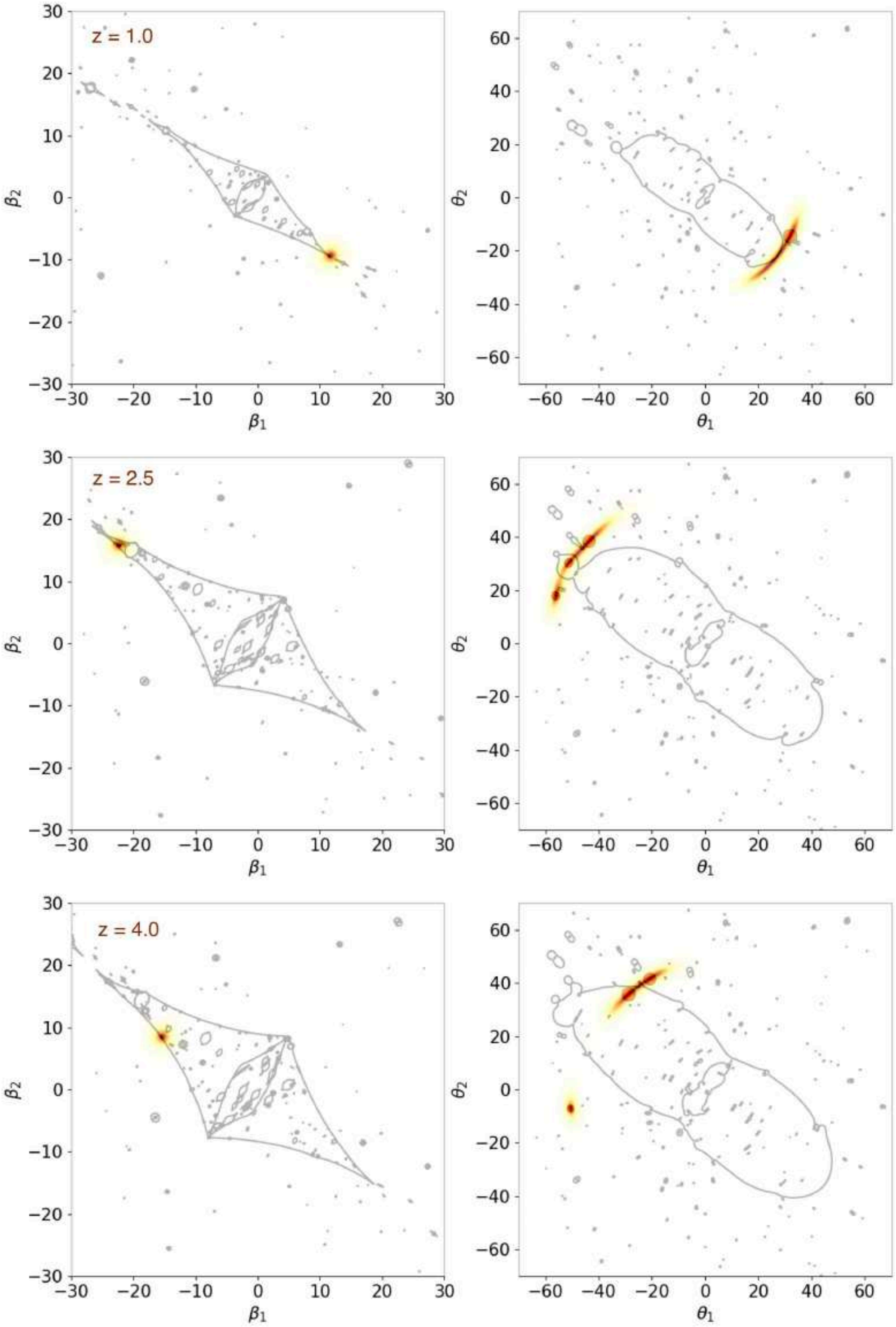

Figure 3.26: Caustics (on the left) and critical lines (on the right) of Abell S1063 for three sources located at $z = 1.0$, $z = 2.5$ and $z = 4$, respectively, such as (g), (h) and (i) in Figure 3.16. We place these sources on the source plane in correspondence of the red-yellow point and they are distorted into highly magnified gravitational arcs. The red circles mark the positions of the multiple images.

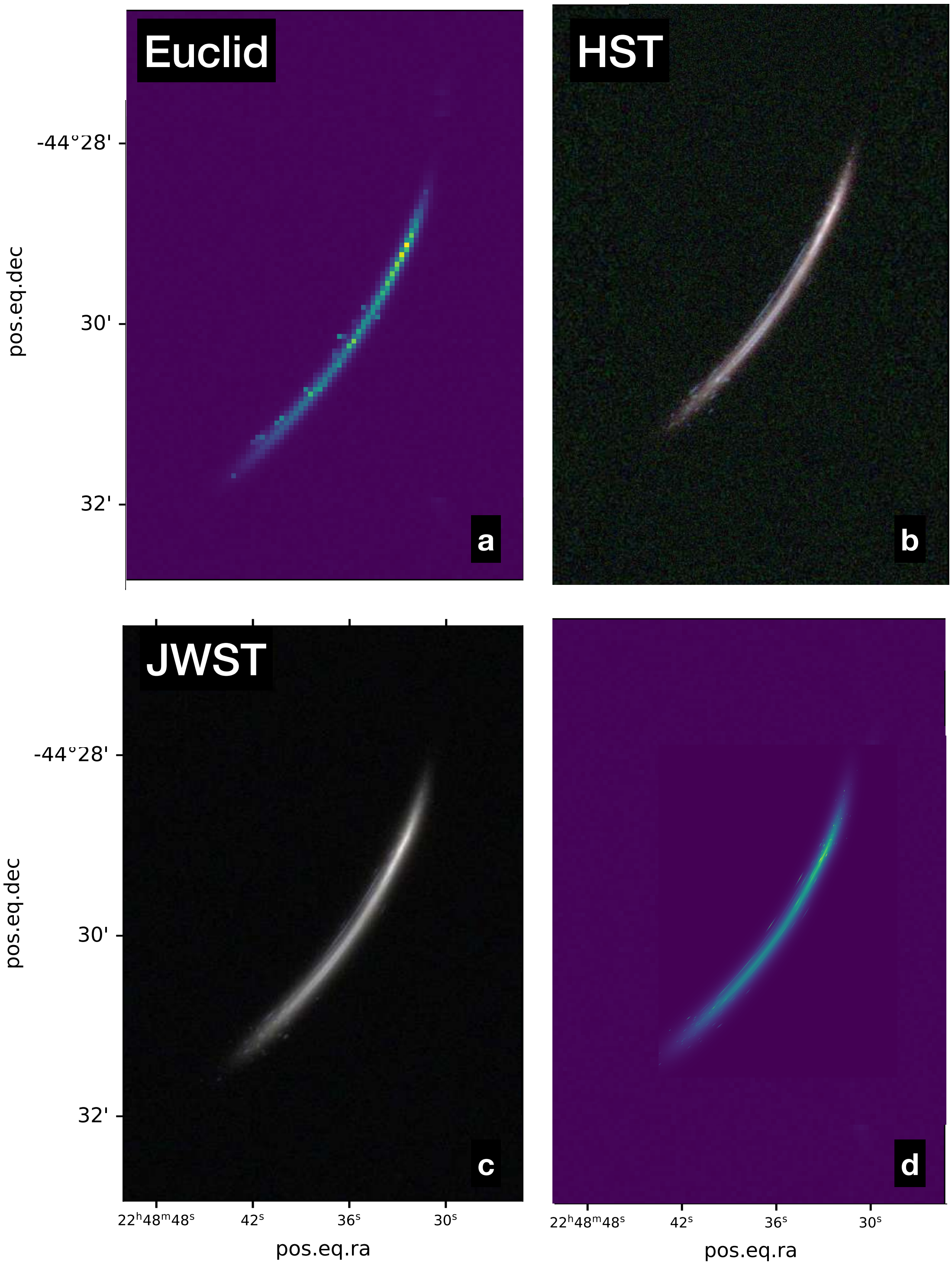

Figure 3.27: Abell S1063, source G ($z = 1$): (a) simulation produced with Euclid/VIS (0.1 arcsec/pix); (b) simulation produced with HST-ACS (0.05 arcsec/pix) using the filters F814W, F606W, and F435W; (d) simulation produced with JWST-NIRCAM (0.031 arcsec/pix) using the filters F200W, F150W and F090W; (d) no noise simulation (0.003 arcsec/pix).

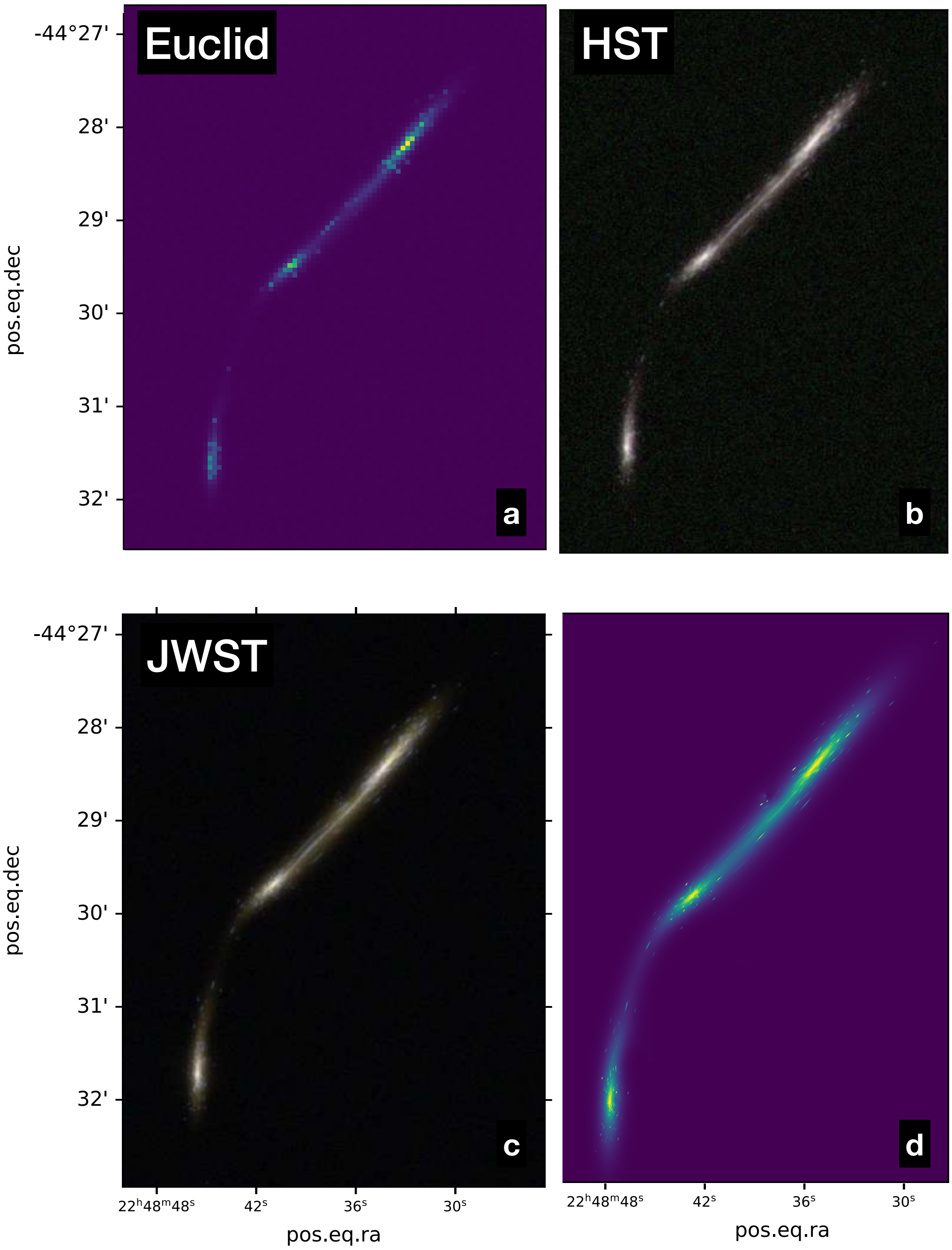

Figure 3.28: Abell S1063, source H ($z = 2.5$): (a) simulation produced with Euclid/VIS (0.1 arcsec/pix); (b) simulation produced with HST-ACS (0.05 arcsec/pix) using the filters F814W, F606W, and F435W; (d) simulation produced with JWST-NIRCAM (0.031 arcsec/pix) using the filters F200W, F150W and F090W; (d) no noise simulation (0.003 arcsec/pix).

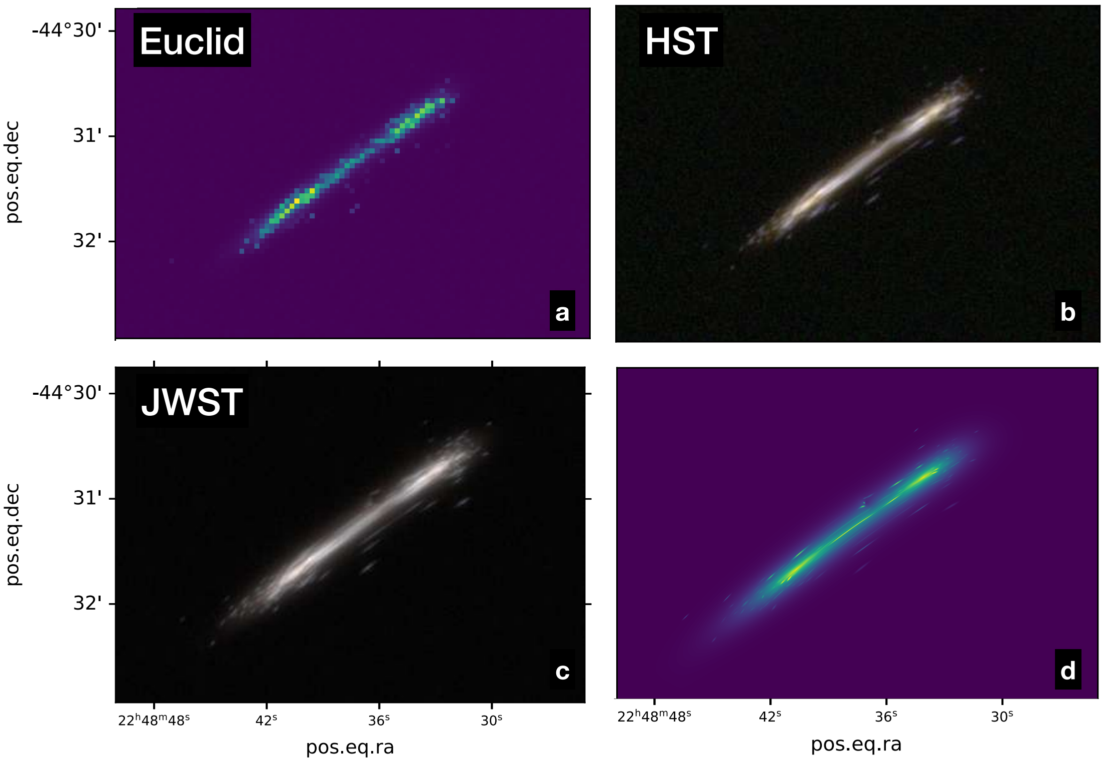

Figure 3.29: Abell S1063, source I ($z = 4$): (a) simulation produced with Euclid/VIS (0.1 arcsec/pix); (b) simulation produced with HST-ACS (0.05 arcsec/pix) using the filters F814W, F606W, and F435W; (d) simulation produced with JWST-NIRCAM (0.031 arcsec/pix) using the filters F200W, F150W and F090W; (d) no noise simulation (0.003 arcsec/pix).

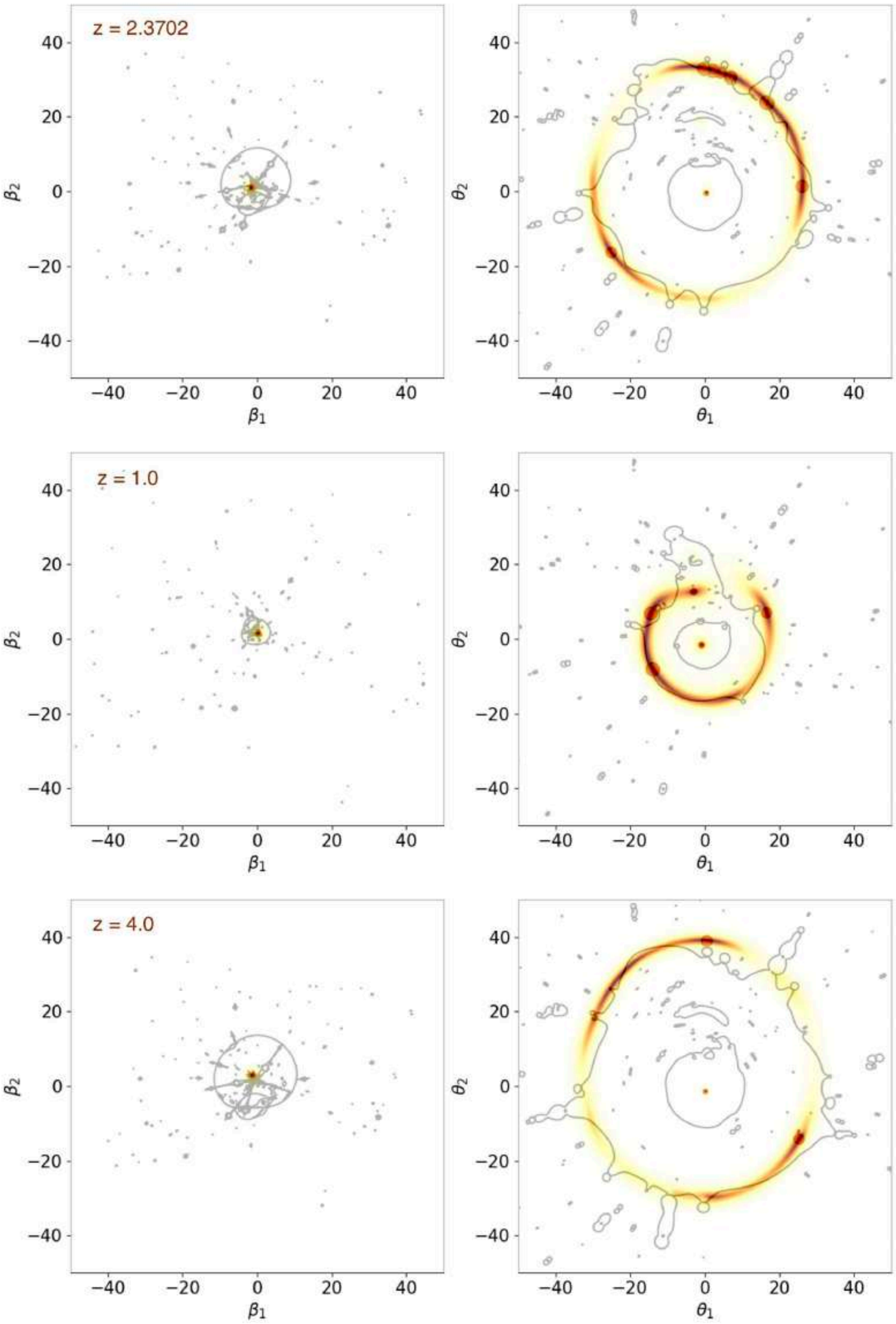

Figure 3.30: Caustics (on the left) and critical lines (on the right) of PSZ1G311.65-18.4 for three sources located at $z = 2.3702$, $z = 1.0$ and $z = 4$, respectively, such as (j), (k) and (l) in Figure 3.16. We place these sources on the source plane in correspondence of the red-yellow point and they are distorted into highly magnified gravitational arcs. The red circles mark the positions of the multiple images.

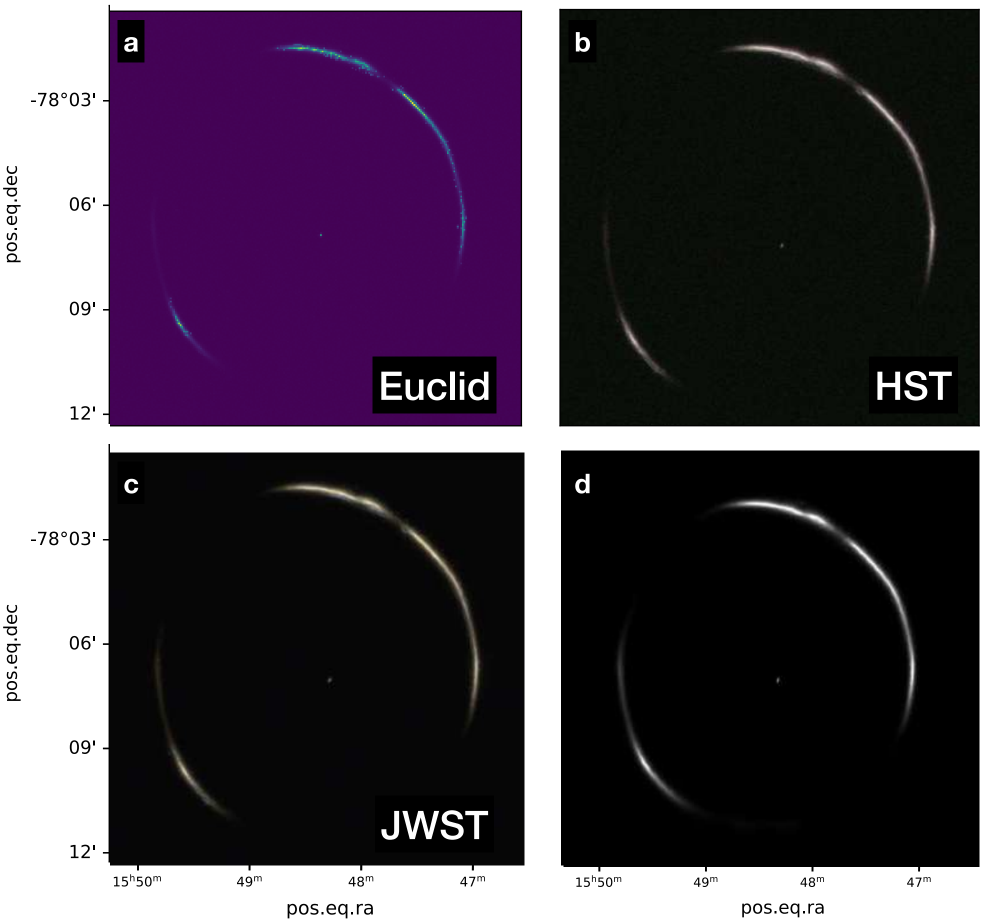

Figure 3.31: PSZ1G311.65-18.48, source J (z = 2.3702): (a) simulation produced with Euclid/VIS (0.1 arcsec/pix); (b) simulation produced with HST-ACS (0.05 arcsec/pix) using the filters F814W, F606W, and F435W; (d) simulation produced with JWST-NIRCAM (0.031 arcsec/pix) using the filters F200W, F150W and F090W; (d) no noise simulation (0.003 arcsec/pix). This source is supposed to reproduce the Sunburst Arc.

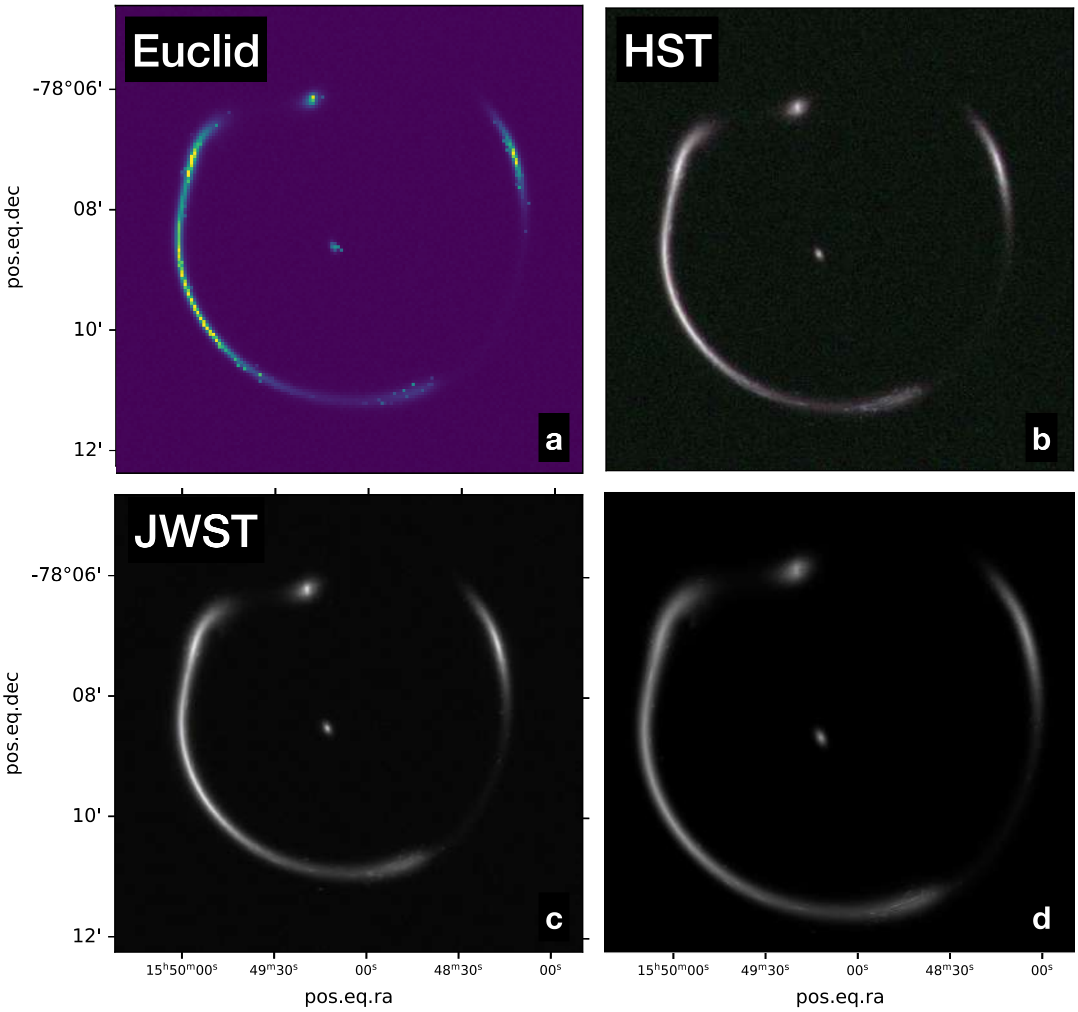

Figure 3.32: PSZ1G311.65-18.48, source K ($z = 1$): (a) simulation produced with Euclid/VIS (0.1 arcsec/pix); (b) simulation produced with HST-ACS (0.05 arcsec/pix) using the filters F814W, F606W, and F435W; (d) simulation produced with JWST-NIRCAM (0.031 arcsec/pix) using the filters F200W, F150W and F090W; (d) no noise simulation (0.003 arcsec/pix).

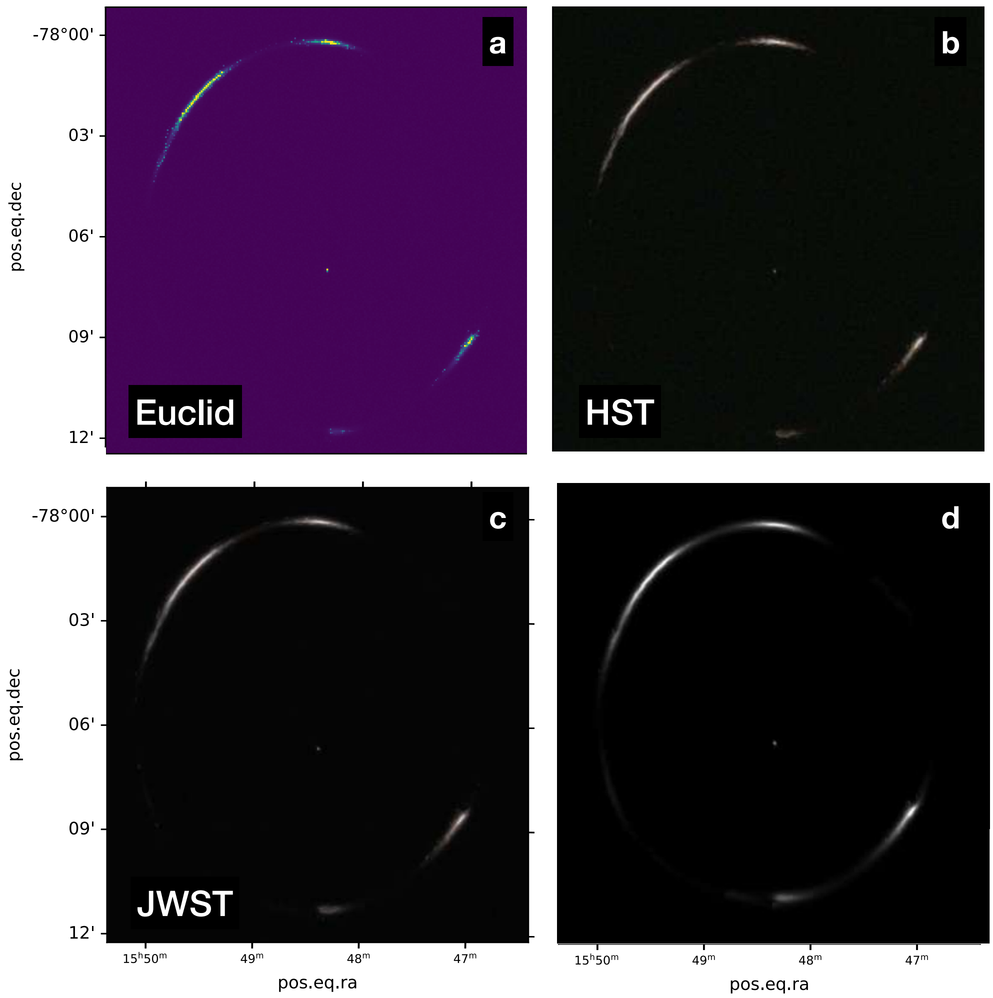

Figure 3.33: PSZ1G311.65-18.48, source L ($z = 4$): (a) simulation produced with Euclid/VIS (0.1 arcsec/pix); (b) simulation produced with HST-ACS (0.05 arcsec/pix) using the filters F814W, F606W, and F435W; (d) simulation produced with JWST-NIRCAM (0.031 arcsec/pix) using the filters F200W, F150W and F090W; (d) no noise simulation (0.003 arcsec/pix).

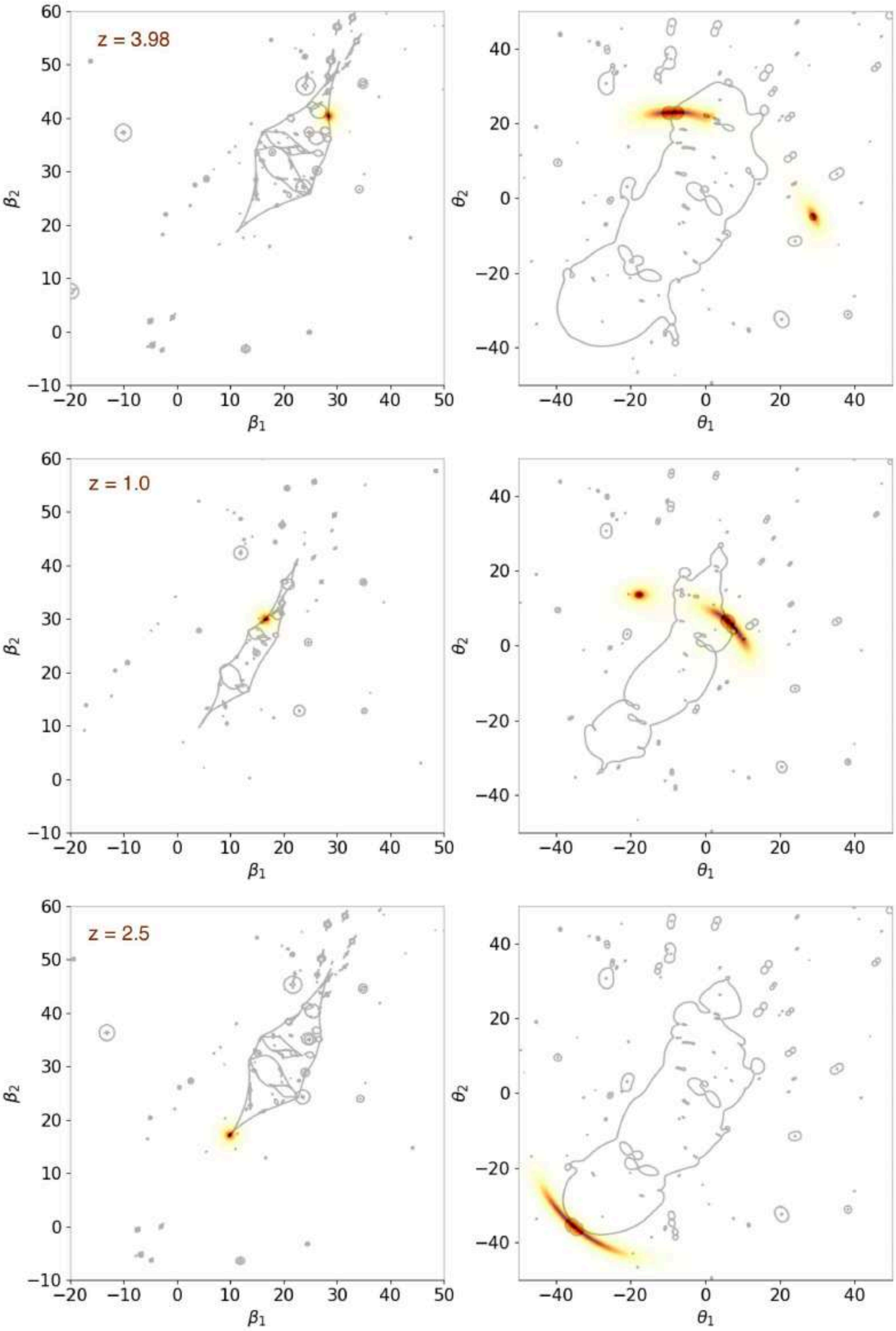

Figure 3.34: Caustics (on the left) and critical lines (on the right) of Abell 2744 for three sources located at $z = 3.98$, $z = 1.0$ and $z = 2.5$, respectively, such as (m), (n) and (o) in Figure 3.16. We place these sources on the source plane in correspondence of the red-yellow point and they are distorted into highly magnified gravitational arcs. The red circles mark the positions of the multiple images.

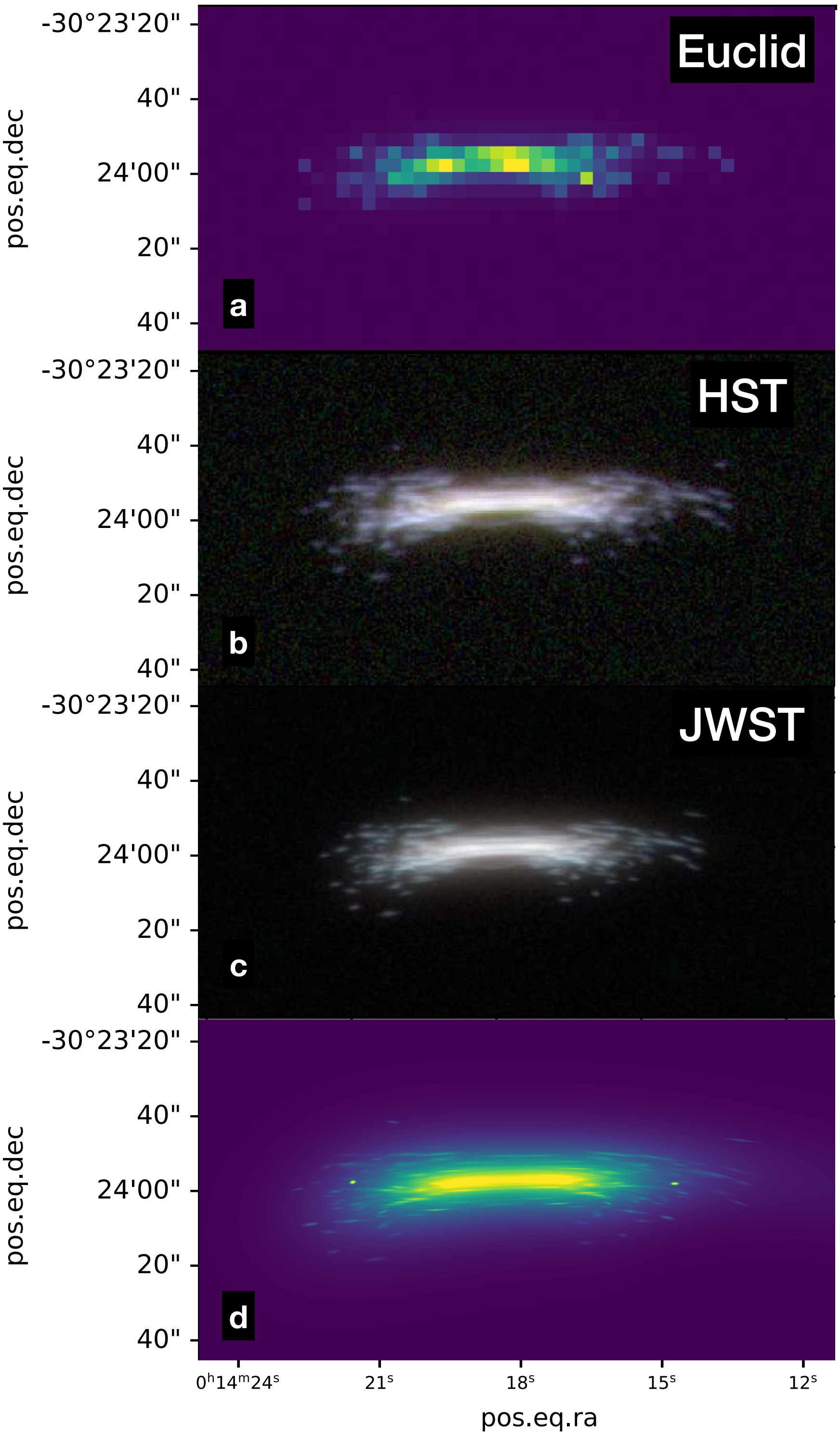

Figure 3.35: Abell 2744, source M ($z = 3.98$): (a) simulation produced with Euclid/VIS (0.1 arcsec/pix); (b) simulation produced with HST-ACS (0.05 arcsec/pix) using the filters F814W, F606W, and F435W; (d) simulation produced with JWST-NIRCAM (0.031 arcsec/pix) using the filters F200W, F150W and F090W; (d) no noise simulation (0.003 arcsec/pix).

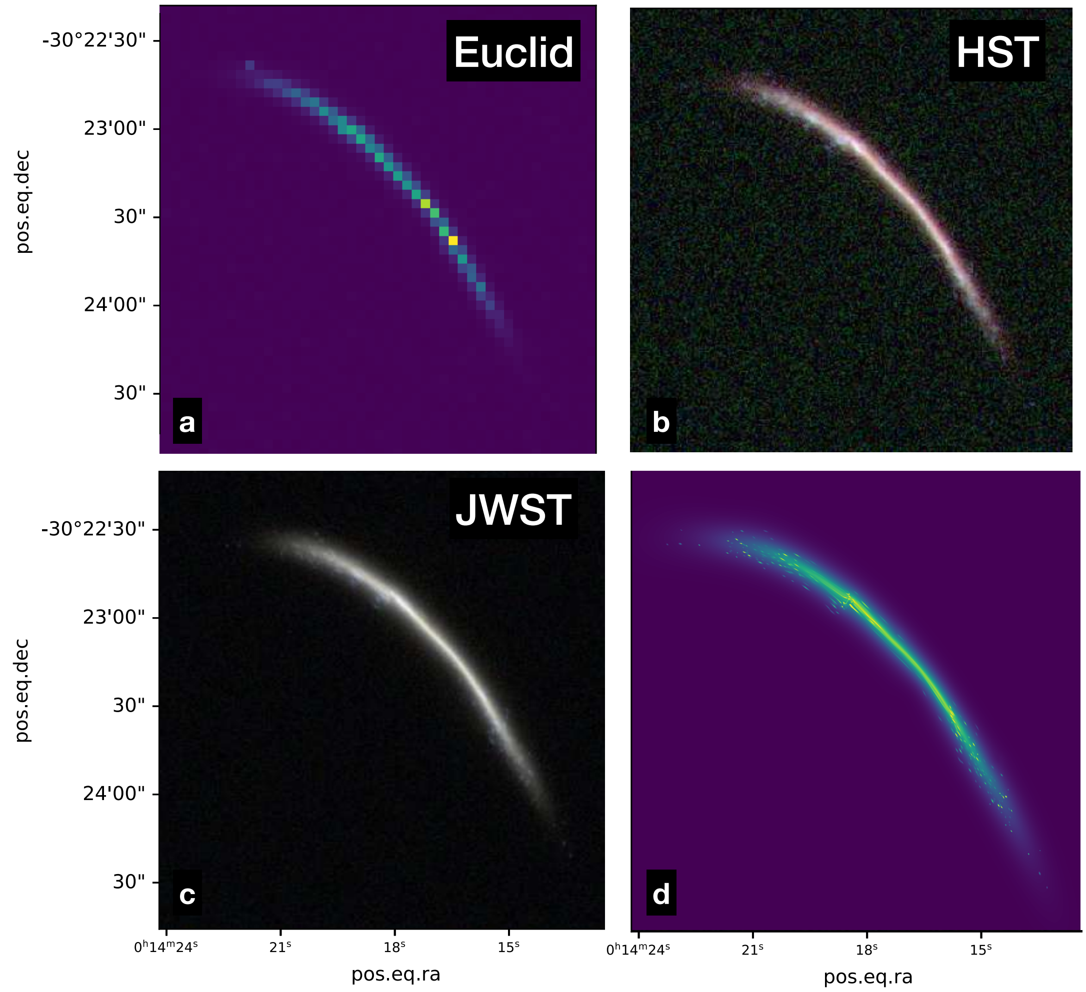

Figure 3.36: Abell 2744, source N ($z = 1.0$): (a) simulation produced with Euclid/VIS (0.1 arcsec/pix); (b) simulation produced with HST-ACS (0.05 arcsec/pix) using the filters F814W, F606W, and F435W; (d) simulation produced with JWST-NIRCAM (0.031 arcsec/pix) using the filters F200W, F150W and F090W; (d) no noise simulation (0.003 arcsec/pix).

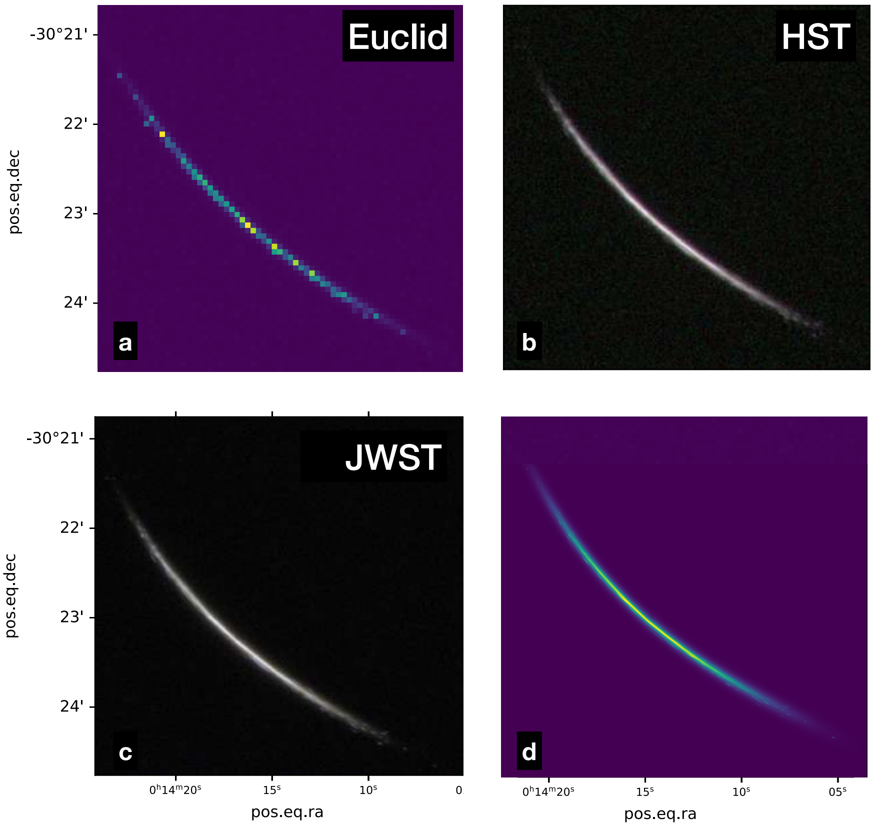

Figure 3.37: Abell 2744, source O ($z = 2.5$): (a) simulation produced with Euclid/VIS (0.1 arcsec/pix); (b) simulation produced with HST-ACS (0.05 arcsec/pix) using the filters F814W, F606W, and F435W; (d) simulation produced with JWST-NIRCAM (0.031 arcsec/pix) using the filters F200W, F150W and F090W; (d) no noise simulation (0.003 arcsec/pix).

Chapter 4

Applications

In this Chapter we show two applications of our simulation pipeline. First, we address the problem of detecting stellar clumps in strongly lensed galaxies. We perform an analysis of simulated observations with different instruments evidencing the visible stellar clumps and attempting a simple statistical comparison of the detections. This analysis is performed with a new software recently developed to address this kind of problems. The analysis presented here validates the performance of this software.

Second, we show how the images simulated with our pipeline can be ingested by other more specific instrument simulators. Specifically, we use `SimCADO`, the instrument data simulation package for MICADO at the ELT, which also incorporates the simulator for MORFEO, the Multiconjugate adaptive Optics Relay For ELT Observations that will support MICADO.

4.1 Detecting stellar clumps with GravityFM

4.1.1 GravityFM

In this work we rely on the python-based modeling code `GravityFM`, developed by Bergamini et al. to study gravitational lenses and lensed backgroud sources. A paper about this software is currently under development and will be submitted in the next months. It is worth noting that `GravityFM` uses the functions included in the lensing library PyLensLib (34).

There are two main types of modeling: inverse and forward modeling. In the inverse modeling, we know a peculiar state and we want to build a model which can describe that state. In other words, we try to understand where our data come from. Whereas, in the forward modeling, we know the model and we study how it will behave and which results it can give. In this case, we do not work on data, but directly on the model. The inverse modeling is fundamental when we do not have a good knowledge of the problem, while, once we have a well developed model, the forward modeling allows us to predict its behaviors.

In particular, `GravityFM` is a forward modeling code implemented to model the surface brightness distribution of lensed background sources. Therefore, if we have an observational image featuring some lensed sources and the deflection angle maps describing the mass distribution of the lens, `GravityFM` is able to model these sources and also to reconstruct how they should appear on the source plane. In practice, we have to fill in a parameter file (*input file*), declaring some technical information regarding the instrument and the photometric filter used for the observation, such as the exposure time, the telescope gain, the noise, and the instrument PSF. Then, we have to load the deflection maps, specifying the lens redshift, as well as the *input image* to be modeled and an eventual noise map. Besides, it contains all the parameters describing the light distributions to be added on the source or lens plane in order to resemble the observation properly. These distributions are assumed to be Sérsic profiles, and, hence, the sources are described by Sérsic parameters: redshift, on-sky position, Sérsic index, effective radius in arcseconds, axis ratio, position angle in degrees, and total flux. Each of these parameters can be fixed or can vary according to a uniform prior distribution defined within a minimum and a maximum value (uninformative prior). Informative Gaussian priors can also be adopted on the parameter values, but these will not be used in our analysis. Hence, `GravityFM` is able to model all the sources by fitting these free parameters of the source light distributions.

Once filled in the input file, `GravityFM` scales the deflection angle maps to the same pixel scale of the input image, in order to obtain, in the end, a model with the same size and number of pixels of the original data.

Then, the modeling process, namely the optimization of the free parameter values of the source light distributions, can start. `GravityFM` performs a Bayesian analysis to sample the posterior distributions of these free parameters. It implements the optimization in two steps: the Maximum Likelihood Estimation and the Likelihood Sampling.

According to the Bayes Theorem, the *Posterior* or *Cost Function*, namely the probability that the parameters $\overrightarrow{\theta}$ of the model M could be representative of the observed data D, can be written as

$$\Pr(\overrightarrow{\theta}|D, M) = \frac{\Pr(D|\overrightarrow{\theta}, M)\Pr(\overrightarrow{\theta}|M)}{\Pr(D|M)}, \tag{4.1.1}$$

where $\Pr(D|\overrightarrow{\theta}, M)$ is the *Likelihood Function*, $\Pr(\overrightarrow{\theta}|M)$ are the priors adopted on parameter values, and $\Pr(D|M)$ is the *Evidence* (23).

Considering a sample of N observed parameters x^i_{obs}, the Likelihood Function can be defined as

$$\mathcal{L} = \prod_{i=1}^{N} \frac{1}{\sqrt{2\pi\sigma_i^2}} e^{-\frac{\chi_i^2}{2}}, \tag{4.1.2}$$

with

$$\chi_i^2 = \frac{[x^i_{obs} - x^i(\overrightarrow{\theta})]^2}{\sigma_i^2}, \tag{4.1.3}$$

where $x^i(\overrightarrow{\theta})$ represents the values assumed by the model given the set of model parameters $\overrightarrow{\theta}$ and is obtained in the optimization process, while σ_i are the errors associated to the data.

However, it is computationally less complicated to work with the natural logarithmic transformation of the Likelihood Function, namely

$$\ln\mathcal{L} = -\frac{1}{2}\sum_{i=1}^{N}\left(\frac{[x^i_{obs} - x^i(\overrightarrow{\theta})]^2}{\sigma_i^2} + \ln(2\pi\sigma_i^2)\right). \tag{4.1.4}$$

The Maximum Likelihood Estimation is meant to maximize the Cost Function $\Pr(\overrightarrow{\theta}|D, M)$ or equally the Likelihood and, therefore, to minimize the χ^2, so that the differences between the data and the model are reduced as much as possible.

In `GravityFM`, the Likelihood Function is defined as the sum over the N pixels of the input image, represented by x^i_{obs}, while $x^i(\overrightarrow{\theta})$ denotes the values of the pixels of the model image and σ is the noise map. In particular, we do not load in `GravityFM` any noise map, as we aim at obtaining a clean model, but a σ image is automatically generated from the exposure time and includes two sources of noise: the photon noise, with a Poisson distribution, and the background count rate. Regarding the Priors, these are the uninformative uniform distributions assumed on the free model parameters defined in the input file. More specifically, the software verifies if each parameter describing the model is included inside the corresponding range written in the input file. If so, the Prior assumes a constant value. Otherwise it is set at -∞ and, therefore, the maximization of the Cost Function fails.

In practice, in order to find those values of the free parameters which maximize the Likelihood and the Cost Function, `GravityFM` utilizes the *Particle Swarm Optimization* (PSO) through the python toolkit `pySwarms` ((24) and (48)). It is an iterative optimization algorithm, inspired by the social behaviour of swarm of birds. The free parameters, or walkers, move intelligently towards the maximum likelihood peak. More precisely, in each iteration these walkers move inside the space of parameters towards a new point. The movement is accepted only if a peculiar probability, determined through an algorithm inherent to the walkers and associated to that point, is higher than a fixed threshold. Otherwise, the walker comes back to the previous position. In `pySwarms` this probability is computed through the Metropolis-Hastings algorithm, which imposes that the closer the walkers get to the Likelihood peak, the easier the movement is to be accepted. Therefore, all the walkers are supposed to advance towards the proper peak, without coming back, as they should move from a high probability region to a lower one.

At the end of the PSO-optimization, this algorithm provides a best-fit value, or *best-PSO* for all the free parameters we are considering.

Subsequently, there is the second part of the optimization process: the likelihood sampling, executed through the python module `emcee` (20) and aimed at sampling the posterior distributions of the free parameters. This process starts from the best-PSO values. It initializes the walkers considering a hypersphere centered in the best-PSO values. It is worth noting that the sampling executed by `emcee` is well-functioning if the number of walkers is equal to $2n + 2$, where n is the number of free parameters. However, `GravityFM` considers this requirement and defines the optimal number of walkers. The initial phase of the sampling is the burn-in, where the walkers start moving away from the best-PSO values. As soon as their positions can be considered independent of the initial position, `GravityFM` starts the iterative sampling: the walkers move inside the space of parameters, and in each point they compute the probability that the parameters assume those peculiar values. We note that some of the model parameters could be degenerate. For instance, the Sérsic index n strongly degenerates with the effective radius R_e: the combination high n and low R_e values generates a similar probability to that obtained with higher R_e and lower n. When degenerate pairs are optimized together, they bring to more combinations of different solutions described by the same observational data. Evidently, the likelihood sampling is more time-demanding than the maximum likelihood estimation, since the walkers now have to finely explore the considered parameter space. The results of the posterior sampling process are a series of Monte Carlo Markov Chains (MCMC) that register the walker positions as a function of the optimization steps. From the MCMC we can derive the shape of the posterior distribution for the parameters.

The best-fit values determined with this optimization process enable us to generate models not only of the unlensed source, but also of the multiple images. By convolving these models with the PSF specified in the input file, `GravityFM` is able to generate images that are directly comparable to the observations. To generate more realistic model images, a realistic noise model can also be added by `GravityFM`.

Below, for completeness, we report some of the several different modes in which `GravityFM` can work:

- INPUT: generates an example of input file;
- OPTIMIZE: optimizes the source and lens parameters specified in the input file;
- RESULTS: allows us to read the results, originally packed in a compressed file;
- IMAGES: generates models for the multiple images on the lens plane;
- CUTOUTS: generates data, model and residual cutouts;
- SOURCES: generates models for the unlensed sources on the source plane;
- SOURCE_POSITIONS: allows us to deproject the point-like positions of the multiple images onto the source plane;
- MAPVALUES: maps an image from the image plane to the source plane;
- RADEC2XY: transforms RA and DEC coordinates into distances in arcsec with respect to reference coordinates;
- XY2RADEC: transforms distances in arcsec into RA and DEC coordinates (inverse function of RADEC2XY).

	data	best-fit
z	3.98	-
x [arcsec]	28.395195	28.3952
y [arcsec]	40.2729467	40.2730
n	1.0	-
Re [arcsec]	0.3	0.2999
q	0.4	-
ϕ [deg]	-180	-
F_{tot} [DN/s]	215.07	215.00

Table 4.1: First column: input parameters of the simulated Sérsic background source producing the lensed arc visible in the top left panel of Figure 4.1; second column: best-fit values resulting from `GravityFM`. From top to bottom, the parameters are the source redshift z, positions x and y, Sérsic index n, effective radius Re, axis ratio q, position angle ϕ and flux F_{tot}. Fixed model parameters are marked with a bar (-) in the second column.

We note that, in this work, we consider deflection angle maps which we assume to describe perfectly the mass distribution of galaxy clusters. However, real lens models are not perfect. To account for this problem, it can be necessary to add to the deflection maps some corrections, up to the second order. In practice, `GravityFM` can generate adaptive maps, including translations or more complex transformations.

Finally, `GravityFM` also gives the possibility to add extra gravitational lenses and light distributions on the lens plane. We have to specify which model describes the new lens and to declare some additional parameters in the input file (e.g., redshift, position, velocity dispersion, axis ratio, position angle). However, our lens models are assumed to be perfect, and, therefore, we do not add any extra lens.

4.1.2 First applications

In this Chapter, we use `GravityFM` to model some of our simulated images of gravitationally lensed systems (see Chapter 3), testing its performance when confronted with different instruments and spatial resolutions. Moreover, we want to give an estimation of the number of stellar clumps that we are able to detect in the images observed by the different considered telescopes (i.e. Euclid, HST and JWST).

To test the `GravityFM` performances, at first we try to model some simple objects. In this preliminary test, we consider the host galaxy alone and we parametrize it as a Sérsic source lensed by the galaxy cluster Abell 2744 and whose properties are listed in the first column of Table 4.1. We choose to treat as free parameters the source position, effective radius, and total flux. The optimization process (mode `OPTIMIZE`) provides the best-fit values listed in the second column of the same Table.

The cutouts (mode `CUTOUTS`) are shown in the left panels of Figure 4.1. They show DATA, the original image, MODEL, generated at the end of the `GravityFM` optimization process by using the best-fit values as Sérsic parameters, and RESIDUALS, which corresponds to the difference between DATA and MODEL images. The purpose of our optimization is to minimize the χ^2, namely the difference between the input image and the final model, which also corresponds to the definition of residual image. Hence, we can say the modeling is successful if the RESIDUALS is the closest to zero in each pixel.

To complicate the source, we add to the galaxy a single Sérsic clump, whose properties are listed in the second column of the Table 4.2. We still consider as free parameters the effective radius, the clump position and the total flux. The optimization process provides the best-fit values listed in the third and fourth columns of the same Table, while the cutouts are shown in the right panels of Figure 4.1.

	data galaxy	data clump	galaxy best-fit	clump best-fit
z	3.98	3.98	-	-
x [arcsec]	28.395195	28.3	28.3952	28.3004
y [arcsec]	40.2729467	40.2	40.2726	40.2005
n	1.0	4.0	-	-
Re [arcsec]	0.3	0.01	0.3003	0.0096
q	0.4	1.0	-	-
ϕ [deg]	-180	-90	-	-
F_{tot} [DN/s]	215.07	1.13	214.91	1.16

Table 4.2: First column: input parameters of the simulated Sérsic background source producing the lensed arc visible in the top right panel of Figure 4.1; second column: input parameters of the simulated Sérsic clump located inside the host galaxy; third column: best-fit values for the galaxy resulting from `GravityFM`; fourth column: best-fit values for the clump. From top to bottom, the parameters are the redshift z, positions x and y, Sérsic index n, effective radius Re, axis ratio q, position angle ϕ and flux F_{tot}. Fixed model parameters are marked with a bar (-) in the third and fourth column.

4.1.3 Morphological analysis

Between all the gravitational arcs generated in the previous Chapter, we choose to model with `GravityFM` just the least extended one on the sky plane and, therefore, the ones with lower computational costs. In particular, we use the source M lensed by Abell 2744 (Figure 3.16m), the source D lensed by MACS 0416.1-2403 (Figure 3.16d), and the sources A and B lensed by MACS J1206.2-084 (Figure 3.16a and Figure 3.16b).

Our analysis consists of the following steps: we firstly select a region which includes the source, in order to select and minimize the number of pixels to be fitted; then, we optimize only the source parameters, totally ignoring the substructures. Thus, we expect to see in the residuals cutouts only those stellar clumps detected by the instrument, clearly blended with the noise. Finally, using the `photutils` function `find_peaks()`, we can identify the peaks in the image as the maxima above a fixed threshold and, therefore, proceed with a statistical analysis about the number of clumps detected by each instrument.

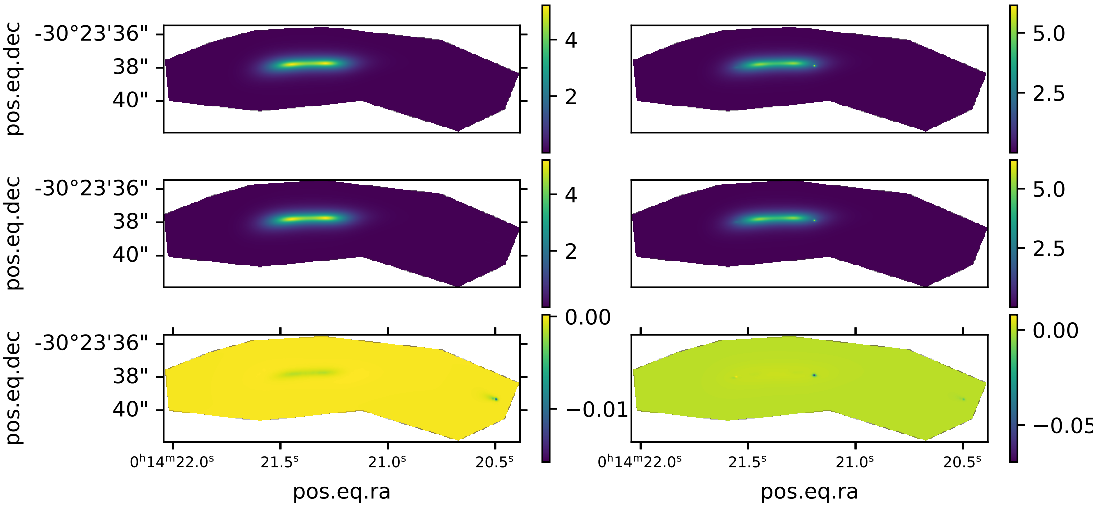

Figure 4.1: Cutouts of the optimized sources: in the left panels, from top to bottom there are DATA; `GravityFM` MODEL; RESIDUALS for the first preliminary test. In the right panels, from top to bottom there are DATA; `GravityFM` MODEL; RESIDUALS for the second preliminary test. These images are produced through the `CUTOUTS` mode of `GravityFM`.

This task is executed both for the unlensed and lensed sources previously selected, in order to see the effects of gravitational lensing on high-redshift galaxies. It is worth noting that to optimize the unlensed sources, we use null deflection maps as input in `GravityFM`.

GravityFM Optimization

As an example, we continue to show our simulation of the Cosmic Snake Arc, describing for it the `GravityFM` optimization process. We note that, the same process is followed for every source, both lensed and unlensed. Since we are trying to consider the most general case, the only Sérsic parameters we fix are the source redshift and Sérsic index, as this latter is degenerate with the effective radius. In each case, we set 3000 steps for the PSO optimization and 5000 for the maximum likelihood sampling, in order to give all the walkers the opportunity to find the corresponding maximum likelihood peak and to determine the posterior distributions.

We begin with the unlensed source and generate the proper null deflection maps. Then, also the lensed source is optimized, using the deflection maps associated to MACS J1206.2-084. This task is replicated for HST/ACS, JWST/NIRCAM, and Euclid/VIS. The Sérsic parameters describing this source as seen by the three telescopes are listed in the first, fourth and seventh row of Table 4.3. Lastly, the optimization is executed and leads towards the cutouts shown in Figure 4.2 and Figure 4.3, while the best-fit values are reported in the other rows of the same Table. It is worth noting these are clean models, namely we do not add to them the noise. However, they all are convolved with the PSF associated to the proper filter.

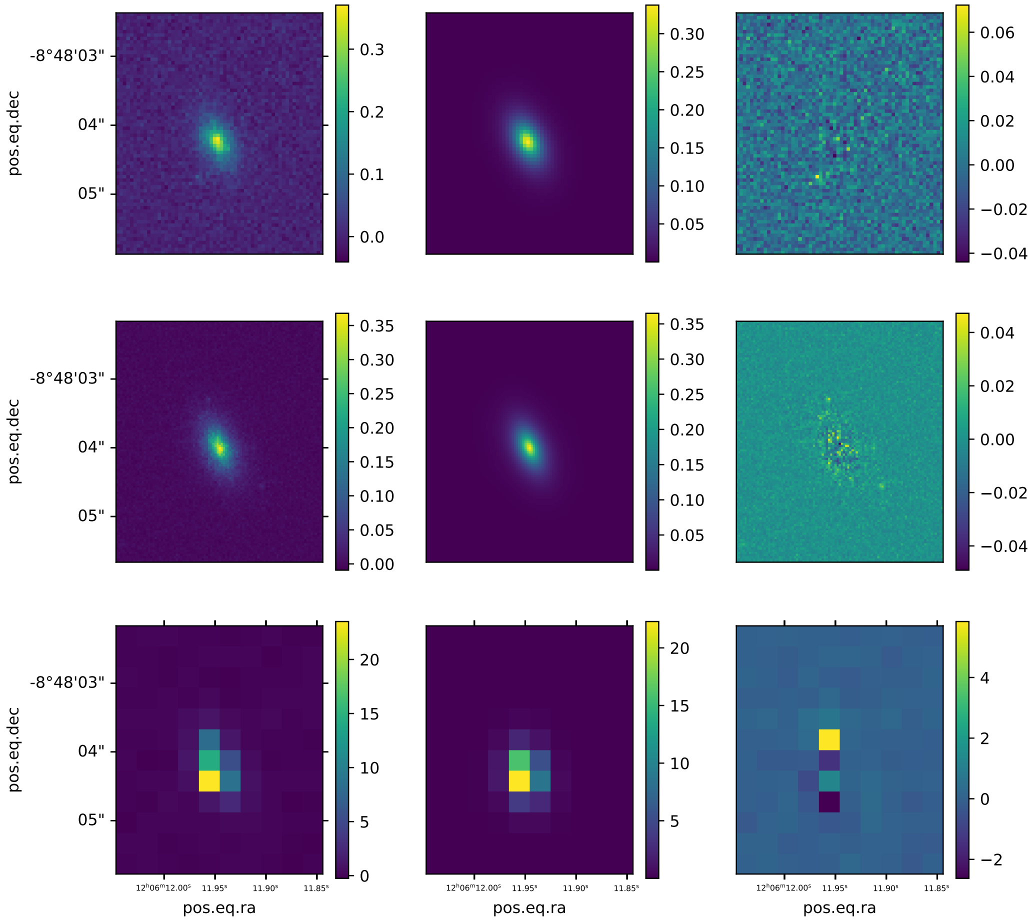

Figure 4.2: CUTOUTS from the optimization of source A. This is the unlensed case, hence generated using null deflection maps as input in `GravityFM`. In the first column are listed the DATAs, in the second the MODELs and in the third the RESIDUALSs, while the rows represent HST, JWST and Euclid simulated observations. These images are produced through the `CUTOUTS` mode of `GravityFM`.

Substructure statistics

This paragraph describes the second part of our analysis, where we use the `photutils` function `find_peaks()`[1] on the residual cutouts to find the simulated source substructures. To use this function, two input parameters have to be specified: the `box_size`, corresponding to a region around each pixel defining a minimum separation between the detected substructures, and `threshold`, which fixes the data value to be used as a threshold for the detection. Both parameters have to be adapted to each individual case. The residuals cutouts obtained with the three different instruments, but associated to the same source, are considered simultaneously. Moreover, in order to be as consistent as possible, these images are normalized so that each pixel contains a number of

---

[1] https://docs.scipy.org/doc/scipy/reference/generated/scipy.signal.find_peaks.html

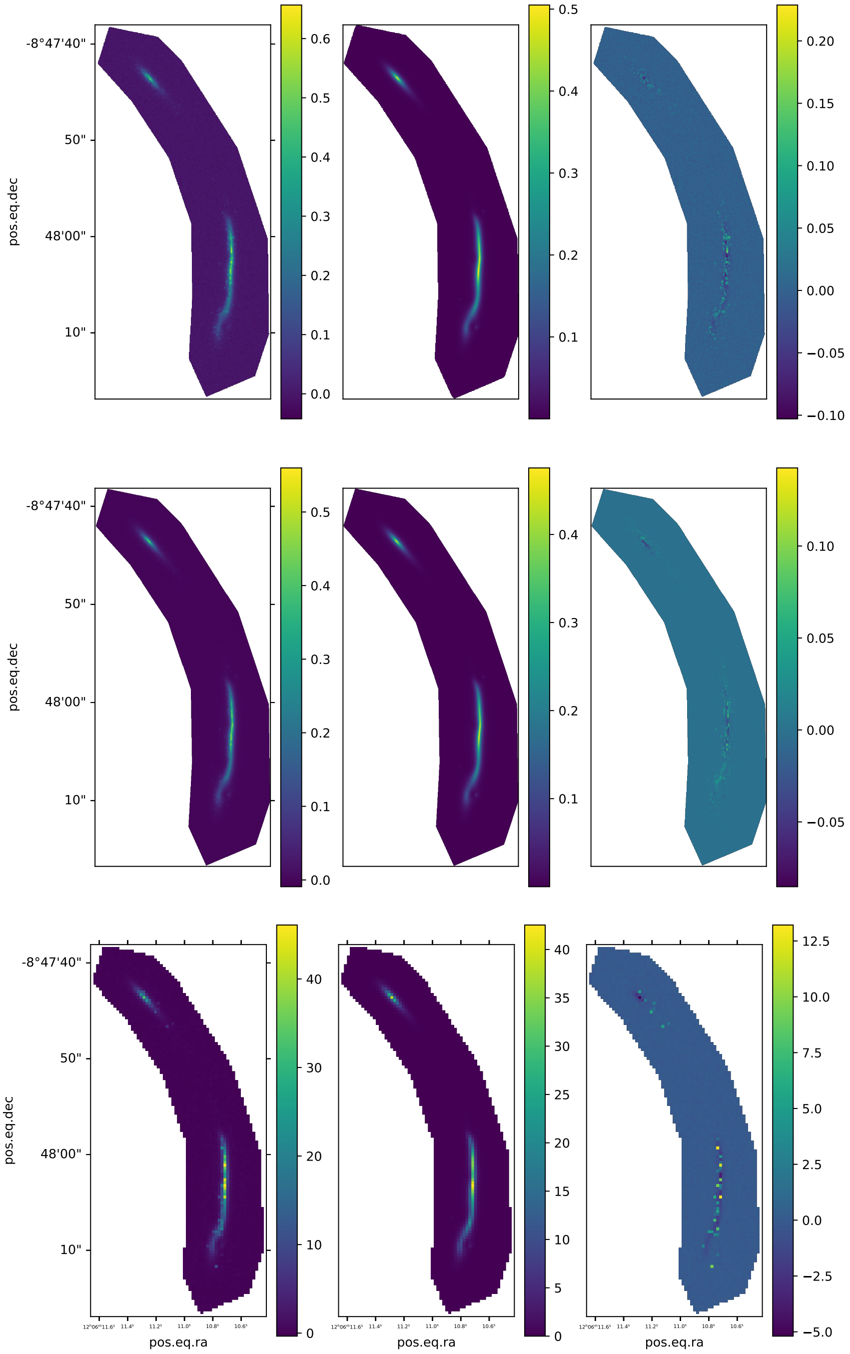

Figure 4.3: CUTOUTS from the optimization of the source A. This is the lensed case, hence generated using the deflection maps generated by the mass distribution of MACS J1206.2-084. In the first column we show the DATAs, in the second the MODELs and in the third the RESIDUALSs, while the rows represent HST, JWST and Euclid simulated observations. These images are produced through the `CUTOUTS` mode of `GravityFM`.

counts/s which lies in the range $[0, 1]$: thereby, we can fix a common threshold and this guarantees us an objective comparison. Clearly, a too high threshold value could lead to a loss of statistical information, while a too low value could lead to spurious detections associated with the noise. For this reason we choose the two `find_peaks` parameters in the attempt to detect in each residual

	z	x [arcsec]	y [arcsec]	n	Re [arcsec]	q	pa	F_{tot} [counts/s]
data HST	1.036	5.099	2.1588	1.0	0.3	0.5	22.5	23.95
unlensed best-fit HST	-	5.0939	2.1596	-	0.2882	0.5558	24.2427	27.83
lensed best-fit HST	-	5.0911	2.1612	-	0.2862	0.5348	22.1055	29.14
data JWST	1.036	5.099	2.1588	1.0	0.3	0.5	22.5	61.39
unlensed best-fit JWST	-	5.1294	2.1894	-	0.2918	0.5053	22.3755	65.29
lensed best-fit JWST	-	5.1142	2.1662	-	0.2888	0.5142	21.3433	66.54
data Euclid	1.036	5.099	2.1588	1.0	0.3	0.5	22.5	53.77
unlensed best-fit Euclid	-	5.0616	2.0625	-	0.2255	0.6562	6.0824	81.84
lensed best-fit Euclid	-	5.0969	2.1555	-	0.2888	0.5267	21.7724	58.45

Table 4.3: First, fourth and seventh row: input parameters of the simulated Sérsic background galaxy; second, fifth, eighth row: best-fit values for the unlensed source resulting from `GravityFM`; third, sixth, ninth row: best-fit values for the source lensed by MACS J1206.2-084 resulting from `GravityFM`. From top to bottom, the parameters are the redshift, positions, Sérsic index, effective radius, axis ratio, position angle and flux. Fixed model parameters are marked with a bar (-).

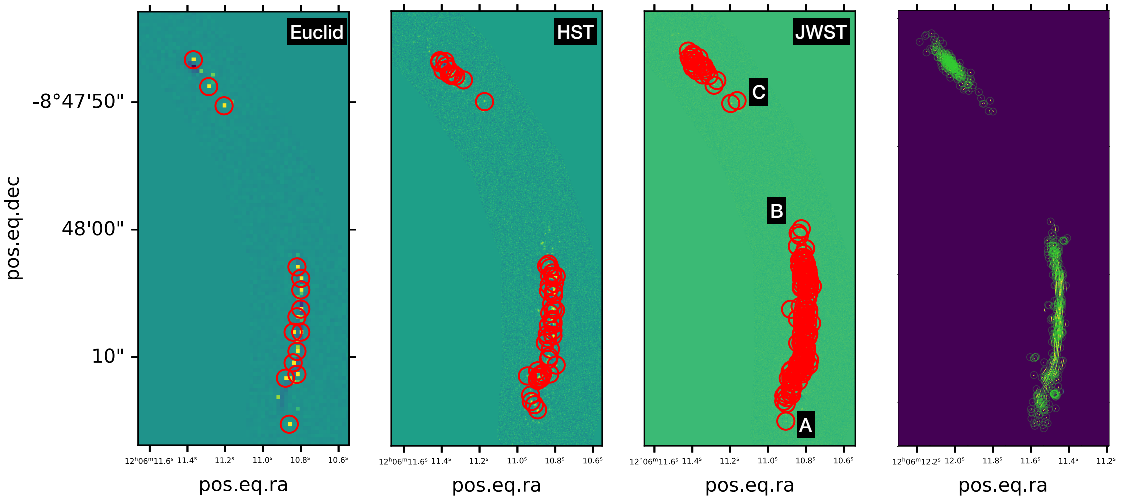

Figure 4.4: MACS J1206.2-084, source A: residual cutouts from `GravityFM` associated to Euclid (first panel), HST (second panel) and JWST (third panel), while the fourth panel is a high-resolution image (0.005 arcsec/pxl). The red circles highlight the peaks detected over a threshold, fixed to 0.51, by the function `find_peaks`. The letters A, B and C mark three peculiar clumps described in the text.

cutout only the actual substructures. Moreover, we visually inspect all the detected substructures in order to finely tune the `threshold` and `box_size` values. The output of the `find_peaks` function is a table listing the pixel coordinates of the peaks and their values. Then, we use these coordinates to highlight the positions of the detected clumps.

MACS J1206.2-084, source (a) We start our analysis from the source A, lensed by MACS J1206.2-084. In Figure 4.4 we show the residual cutouts computed over the models resulting from `GravityFM`. In order, they are associated to Euclid, HST and JWST, while the fourth panel is a high-resolution image (0.005 arcsec/pxl) which portrays the clumps without the host galaxy and is extremely useful as a means of comparison. The red circles highlight the peaks detected by `find_peaks` over a fixed threshold, which here is set to 0.51. Clearly, setting the threshold is arbitrary and depends on what we are committed to observe. Our purpose is to detect as many clumps as possible, without including noise spikes. Therefore, we adjust the threshold consequently, until we do not find a proper correspondence between the residuals and the high resolution image. We note that, inside the JWST residuals image shown in Figure 4.4, we can distinguish also other clumps whose flux lies under the threshold. However, the selected threshold results as the best compromise to obtain a large number of detected substructures without including peaks due to noise fluctuations.

Using `find_peaks` on this gravitational arc, we determine that Euclid detects 15 clumps, HST 54, while JWST 145. Considering that in this source we simulated 267 substructures which lead to 677 multiple images, we find that Euclid detects the 2.25%, HST the 8.10%, while JWST the 21.74% of the overall number. This trend is not surprising, as a higher spatial resolution characterizes JWST and, hence, a sharper detection is naturally expected. In Figure 4.4, we can see not only that JWST detects a higher number of substructures (clump A and clump B), but also is able to distinguish those clumps which appear as single objects in the HST image (clump C).

Figure 4.5 shows some cutouts of this gravitational arc, enabling us to operate a more accurate comparison between HST and JWST. In particular we consider two different regions. Regarding the first one (red box), we increase the threshold to 0.71. For instance, observing the group of clumps labeled with the letter D, it emerges that, while JWST detects only one clump, HST identifies three objects. Even if this output seems to be in contradiction with what has been told up to now, it is due to the different pixel scales of the two instruments: considering photons coming from the same source, while JWST spreads them in a larger number of pixels, HST collects them in less pixels and, therefore, the number of counts/s associated to each HST pixel will be higher and more likely to overcome the threshold. In addition, contrarily to HST, JWST detects the substructures individually, confirming its extraordinary observational capabilities.

Regarding the other set of cutouts (blue box), we keep the same threshold as in Figure 4.4 in order to better see how the number of detected clumps varies as a function of the instrument. For instance, clump E, clearly visible in the JWST observation, is completely missing from the HST image. JWST enables us to recognize more details than HST, thanks to its unrivalled spatial resolution.

Considering the unlensed source (Figure 4.6), it emerges the same trend as a function of the telescope resolution, even though now the overall number of detected substructures is lower than in the previous case. Thanks to the magnification and image multiplicity originated from gravitational lensing the detection of high-redshift sources is facilitated. In particular, using `find_peaks` with a threshold of 0.76, we find 1 clump for Euclid, 3 clumps for HST and 11 clumps for JWST. Since the overall number of clumps is 267, Euclid detects 0.37%, HST 1.12%, while JWST 4.12%.

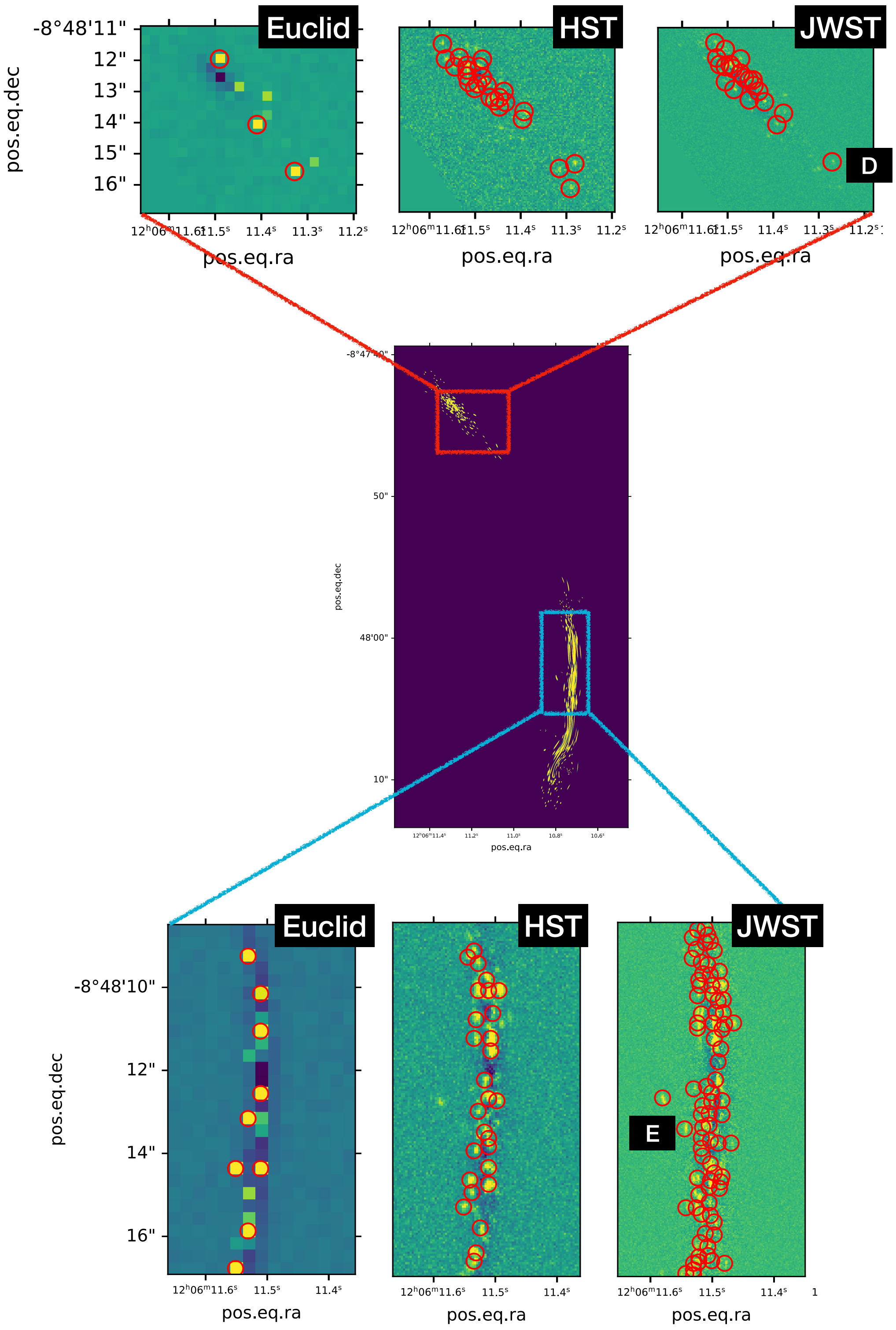

Figure 4.5: Zoom-in over two regions of the gravitational arc. In the red box we consider a threshold equal to 0.71, aiming at finding peculiar substructures such as the group of clumps *D*. In the blue box, instead, we set the threshold back to 0.51 and observe how the detection of clump *E* varies moving from HST to JWST.

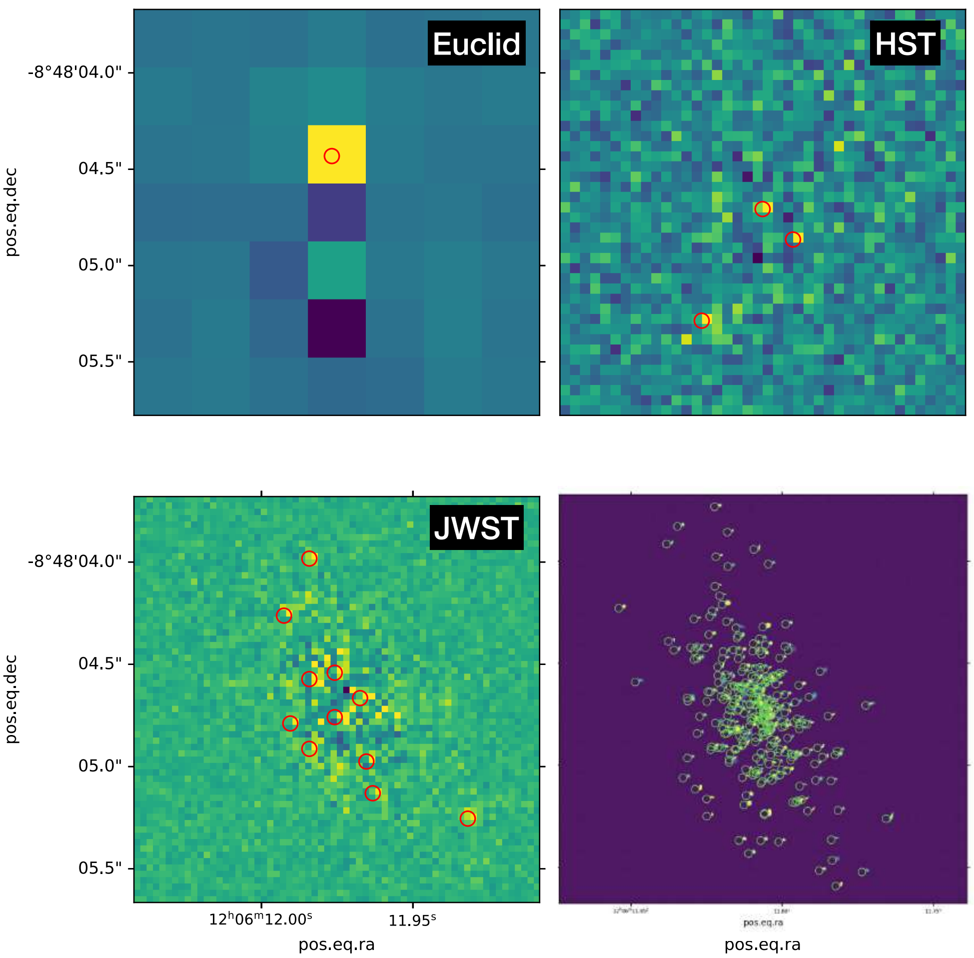

Figure 4.6: We show the residuals associated to the unlensed source corresponding to the arc in Figure 4.4, together with a high resolution image (0.005 arcsec/pxl). The red circles indicate the clumps detected by the three instruments over a threshold set to 0.76.

MACS J1206.2-084, source B Moving to the second source lensed by the same cluster, Figure 4.7 shows the residuals obtained from the `GravityFM` optimization: from left to right Euclid, HST and JWST, respectively. The last panel on the right shows a high resolution image (0.005 arcsec/pxl) of the clumps associated to this lensed source. With `find_peaks` we discover that Euclid detects 10 clumps, HST 71 and JWST 104. Since in this source we simulated 269 substructures which led to 468 multiple images, we can state Euclid detects 2.14%, HST 15.17%, while JWST 22.22% of the overall number. It is worth noting the similarity with the previous results. In this case we set the threshold to 0.55, to allow the detection of special details. In particular, inside this arc there is a region populated by highly stretched clumps, which are a true challenge for `find_peaks`. If the threshold is too low, this function highlights more than one peak inside a single arc, because of the noise and the instrument PSF, and misrepresents the statistical analysis. Increasing the threshold value leads to a better description of the arcs but, at the same time, to a severe loss of information in other regions. The solution is to consider a threshold which is the best

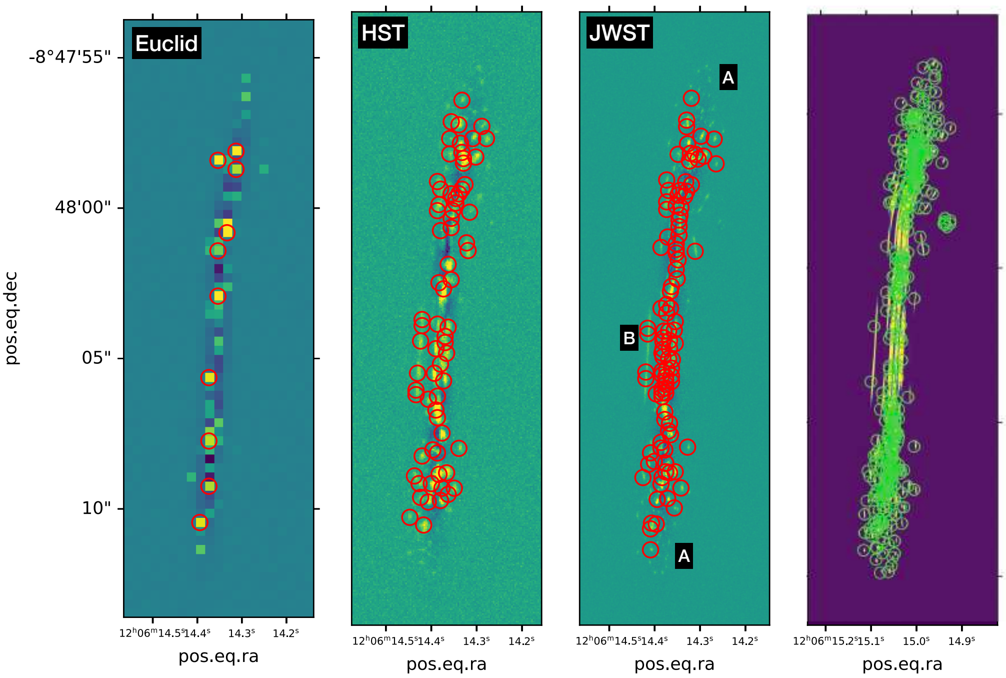

Figure 4.7: MACS J1206.2-084, source B: residual cutouts from `GravityFM` associated to Euclid, HST and JWST (from left to right), while the fourth panel is a high-resolution image (0.005 arcsec/pxl). The red circles highlight the peaks detected over a threshold fixed to 0.55, while the letters A and B mark the two peculiar regions described in the text.

compromise, in order to avoid an excessive loss of information or including too many noise spikes. This is the reason why in Figure 4.7 there are visible clumps which are, however, not included in our analysis (clumps A), together with detected, undesired noise spikes (region B).

In Figure 4.8, we show a zoom-in of two peculiar region inside the arc as seen by Euclid, HST and JWST. The red box focuses on the region populated by the stretched substructures, and the threshold is increased up to 0.75, which is the ideal limit to have only one detection for stretched clump. In this case, it is HST to detect the highest number of substructures: its larger pixels collect more photons and are more willing to overcome the selected threshold. In the blue box, instead, we use a lower threshold, fixed to 0.45: it emerges that with 0.55 we are truly losing some information, mainly for JWST. From a comparison between the cutouts associated to HST and JWST, we can see that JWST not only detects a higher number of substructures, but it can also distinguish those objects that appear as a single source to HST, for instance clump C.

Figure 4.9 illustrates the residuals of the unlensed source. In this case, we have to set the threshold to 0.74, in order to avoid to collect noise peaks in the HST image, even if this means we are ignoring some clumps visible with JWST. The statistical analysis with `find_peaks` leads us to detect 1 clump with Euclid, 3 with HST and 3 with JWST. The total number of clumps in this galaxy amounts to 263; therefore, Euclid detects 0.38% of the clumps, while HST and JWST both 1.14% of them. We note that, as just mentioned, the number of detected clumps in JWST by `find_peaks` is significantly under-estimated. As for the previous source, moving from the lensed

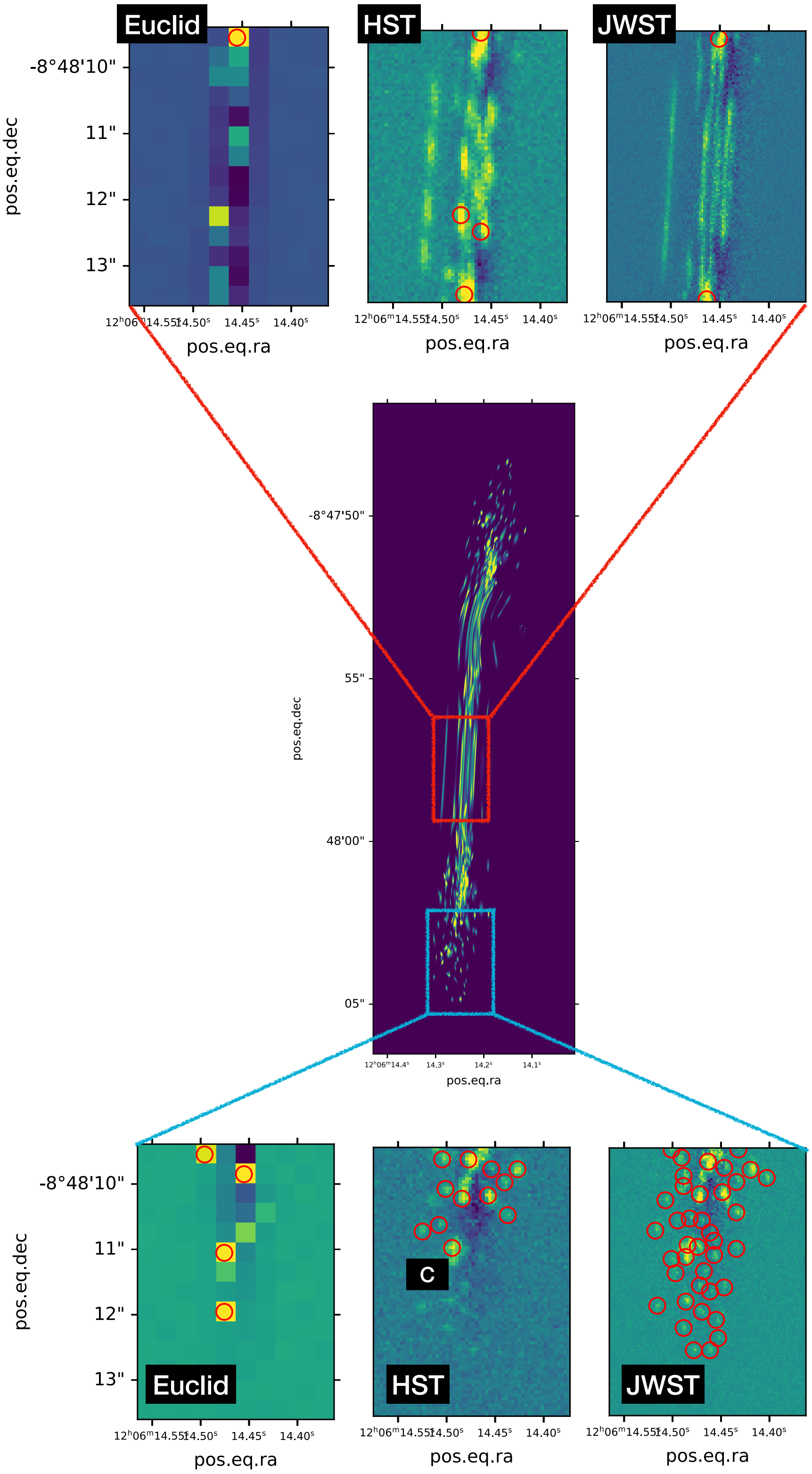

Figure 4.8: Zoom-in over two regions of the gravitational arc. In the red box we consider a threshold equal to 0.75, aiming at detecting highly stretched clumps. In the blue box, instead, we set the threshold to 0.45 and observe that many clumps visible for JWST (C) are not detected by HST.

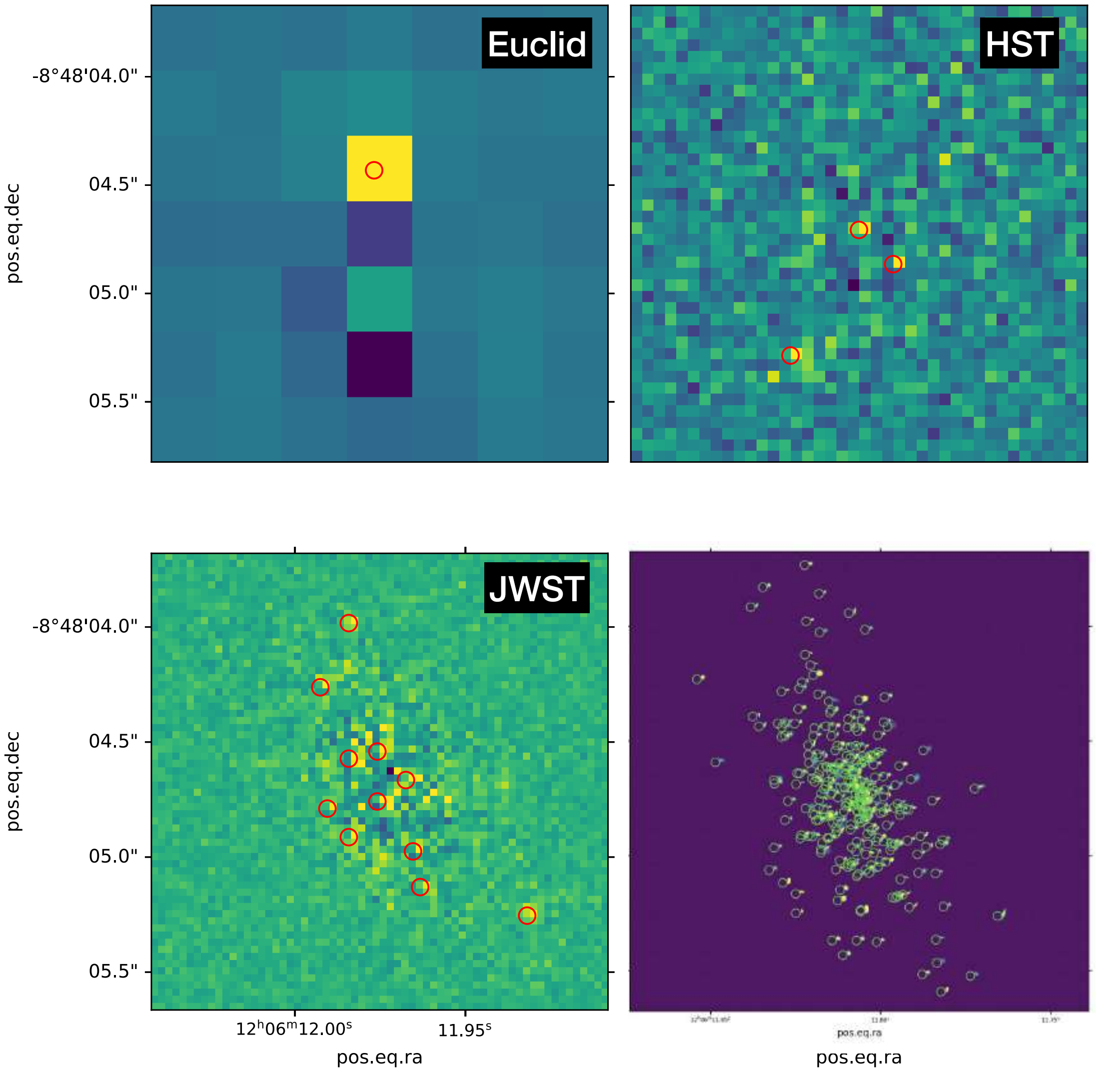

Figure 4.9: The residuals associated to the unlensed source corresponding to the arc in Figure 4.7, together with a high-resolution image (0.005 arcsec/pxl). The red circles indicate the clumps detected by the three instruments over a threshold set to 0.74.

to the unlensed source leads to a decrease in the number of detected clumps.

Abell 2744, source M The third source analysed in this Chapter is source M which is represented in Figure 4.10. As in the previous cases, this Figure shows the three residual maps obtained from `GravityFM` and the high-resolution image of the clumps alone. Again, we can distinguish inside the arc regions where the clumps are highly stretched, and, for this reason, we have to determine a threshold which is the right compromise between two opposite effects. In particular, we set 0.6. Clearly, we lose some statistical information (clump A) and include some noise (region B). However, with this threshold, we find that Euclid detects 2 clumps, HST 76 and JWST 95. Since the total true number of clumps is 251 and they become 293 lensed images, Euclid, HST, and JWST identify 0.68%, 25.94%, and 32.42% of them, respectively.

The cutouts of two peculiar regions of the gravitational arc are shown in Figure 4.11. The

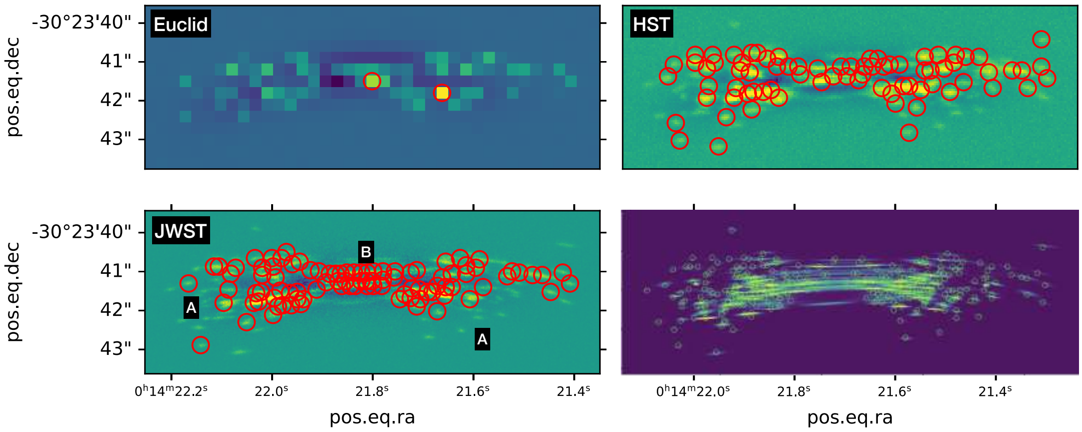

Figure 4.10: Abell 2744, first source: residual cutouts associated to Euclid, HST and JWST and a high-resolution image (0.005 arcsec/pxl) in the fourth panel. The red circles highlight the peaks detected over a threshold of 0.6, while the letters *A* and *B* label the two peculiar regions described in the text.

red box zooms over the sector populated by the stretched clumps. Here we fix the value of the threshold to 0.96 in order to catch just one clump per arc. Naturally, with such a high threshold, the number of detection decreases. The blue box, instead, covers a more external region, and the corresponding cutouts show the usual trend as a function of the telescope. It is worth noting how the clump *C* detected in HST appears to be composed of many more components, when observed by JWST.

The unlensed source in shown in Figure 4.12. Using `find_peaks` with a threshold set to 0.58, we discover that Euclid identifies 2 substructures, HST 4 and JWST 20. Thus, the detections with the three instruments amount to 0.8%, 1.59% and 7.97% of the total number of simulated clumps.

MACS J0416, source D Moving to the source D, lensed by MACS J0416 (Figure 4.13), we fix the threshold to 0.6, in order to reach the usual compromise between regions populated by stretched clumps (region *A*) and the ones where there are more point-like sources (region *B*), in the attempt to minimise the inclusion of noise spikes from the first and the loss of information from the latter. With `find_peaks`, we discover that Euclid identifies 2 substructures, HST 29 and JWST 93. Since there are 269 clumps with 293 multiple images, it means they detect 0.68%, 9.9% and 31.74%, respectively.

In Figure 4.14, we show some cutouts of peculiar regions of the arc. In particular, the blue box zooms over the highly stretched clumps, with a threshold set to 0.8 in order to identify a larger number of substructures. The red box, instead, covers a region populated by more point-like objects, with a threshold which is the same we considered in Figure 4.13, in order to compare the performances of HST and JWST. In this latter case, JWST reveals a higher number of stellar clumps, even if each of them is characterized by a lower value of flux, as, for instance, we can discern looking at the color of the clump *C* in the two residual cutouts. The different size of the pixels of HST and JWST once again causes this effect.

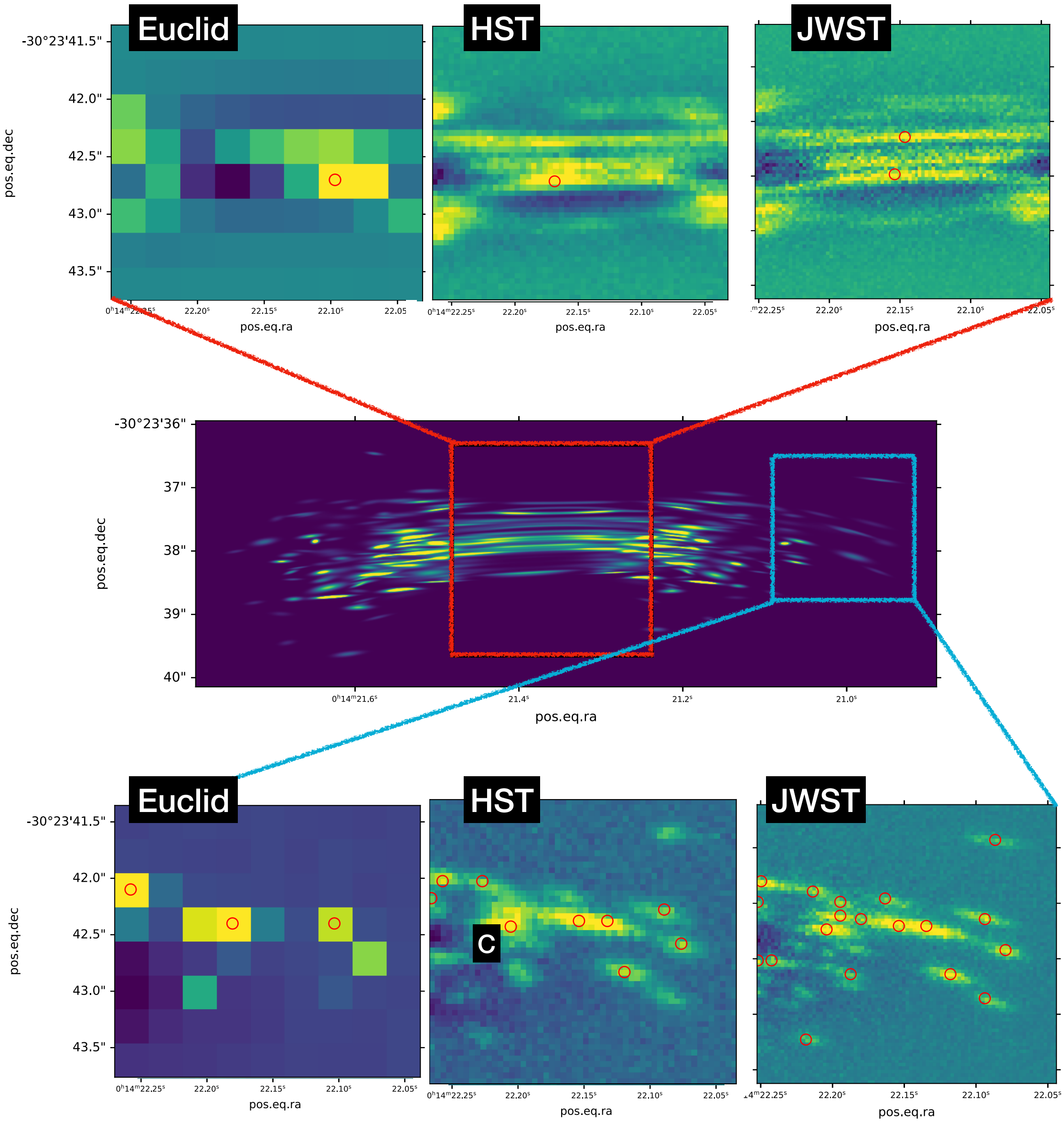

Figure 4.11: Zoom-in over two regions of the gravitational arc lensed by Abell 2744. In the red box we consider a threshold equal to 0.96, aiming at detecting only highly stretched clumps. In the blue box, instead, we consider the same threshold as in Figure 4.10.

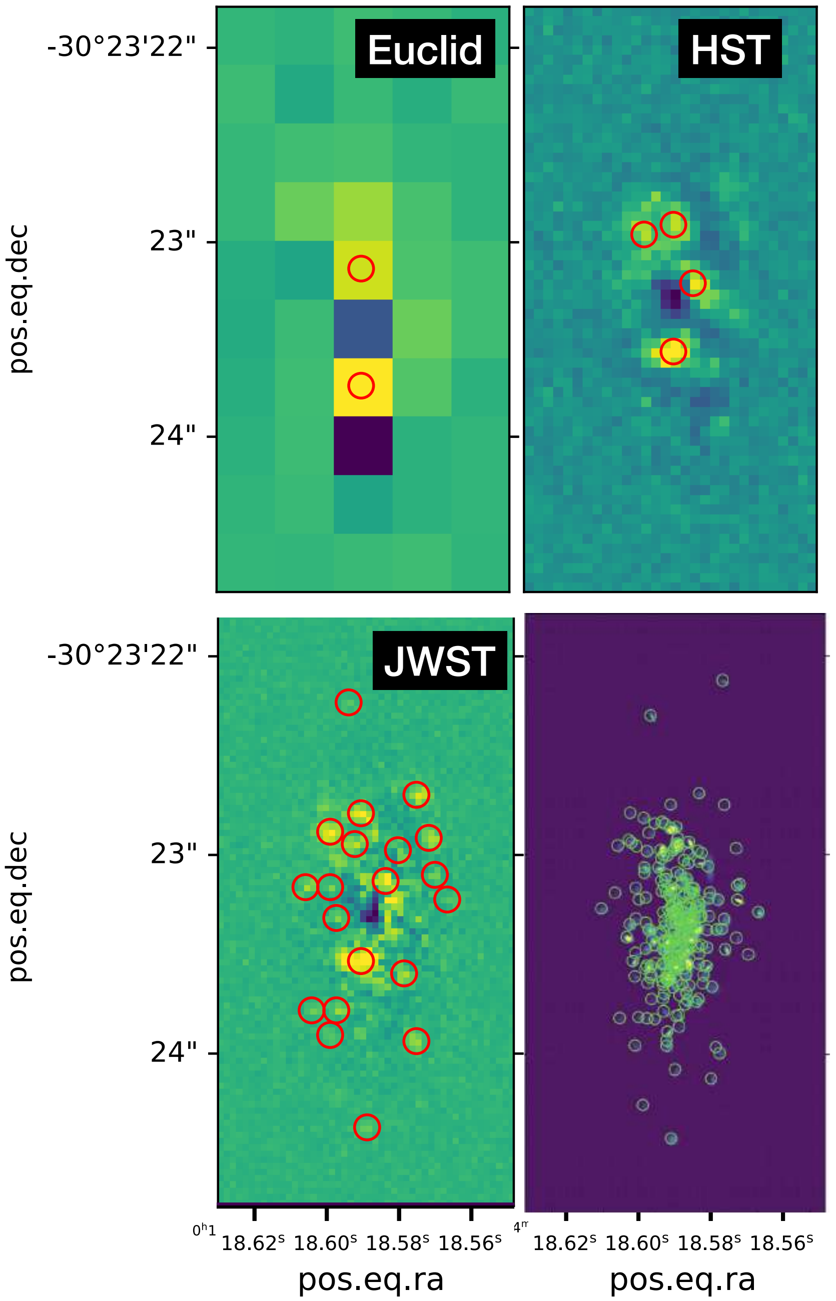

Figure 4.12: The residuals associated to the unlensed source corresponding to the arc in Figure 4.10, while the fourth panel shows a high-resolution image (0.005 arcsec/pxl). The red circles indicate the clumps detected by the three instruments over a threshold set to 0.58.

Lastly, Figure 4.15 shows the corresponding unlensed source, obtained setting the threshold to 0.8. We observe that Euclid identifies 2 substructures, HST 6 and JWST 7. Since there are 269 clumps, it means they detect the 0.74%, 2.23% and 2.6%, respectively.

Summary For clarity, the numbers of detections per instrument for every lensed and unlensed source are recapped in the two histograms in Figure 4.16.

Therefore, in summary, from the analysis on both the unlensed and lensed sources, it emerges

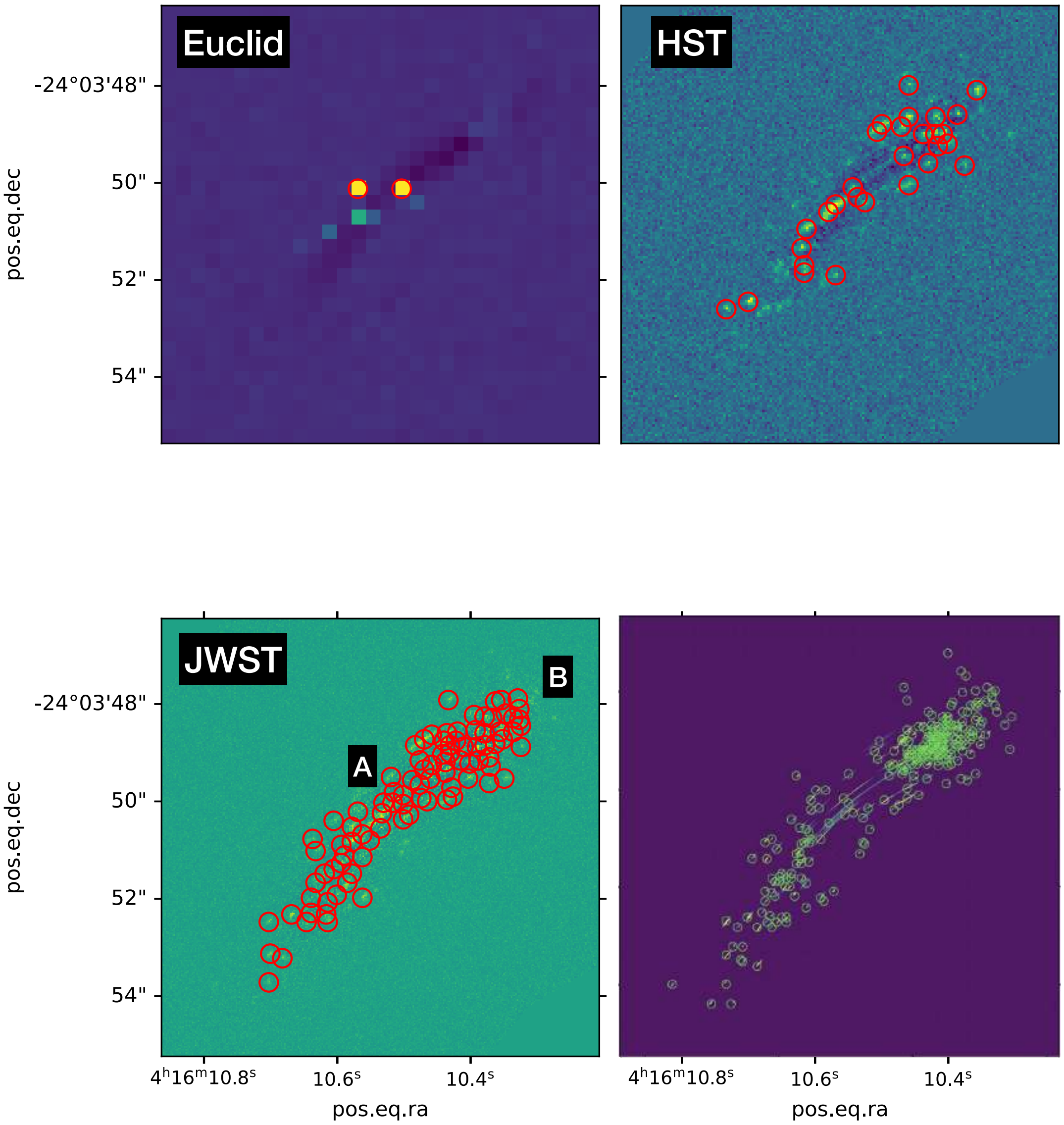

Figure 4.13: MACS J0416, first source: residual cutouts associated to the observations simulated with Euclid, HST and JWST. The fourth panel shows a high-resolution image (0.005 arcsec/pxl). The red circles highlight the peaks detected over a threshold of 0.6, while the letters A and B label the two peculiar regions described in the text.

that the higher spatial resolution which characterizes JWST, in comparison to HST or future instruments like Euclid, enables us to detect a significantly higher fraction of stellar clumps and to resolve more compact objects. This is a crucial information as, for instance, the number and positions of substructures in gravitational arcs are fundamental constraints used to develop strong lensing models for the galaxy clusters. Clearly, relying on observations conducted with instruments whose spatial resolution is not suitable to the detection of such substructures can lead to errors inside the lens model itself.

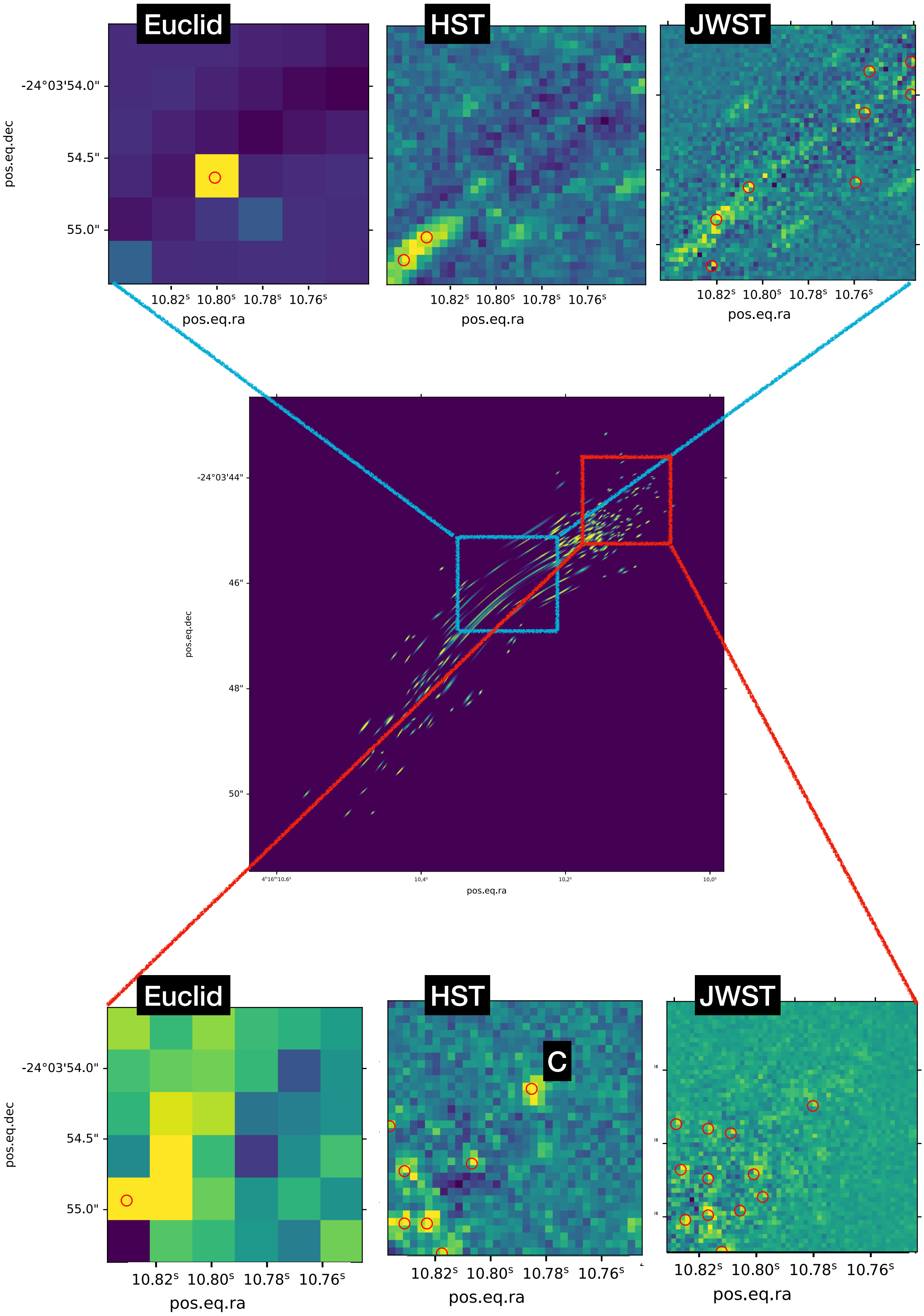

Figure 4.14: Zoom-in over two regions of the gravitational arc lensed by MACS J0416. The red box highlights a sector populated by point-like substructures, with a threshold equal to 0.6, while the blue box, over highly stretched clumps, with a threshold set to 0.8.

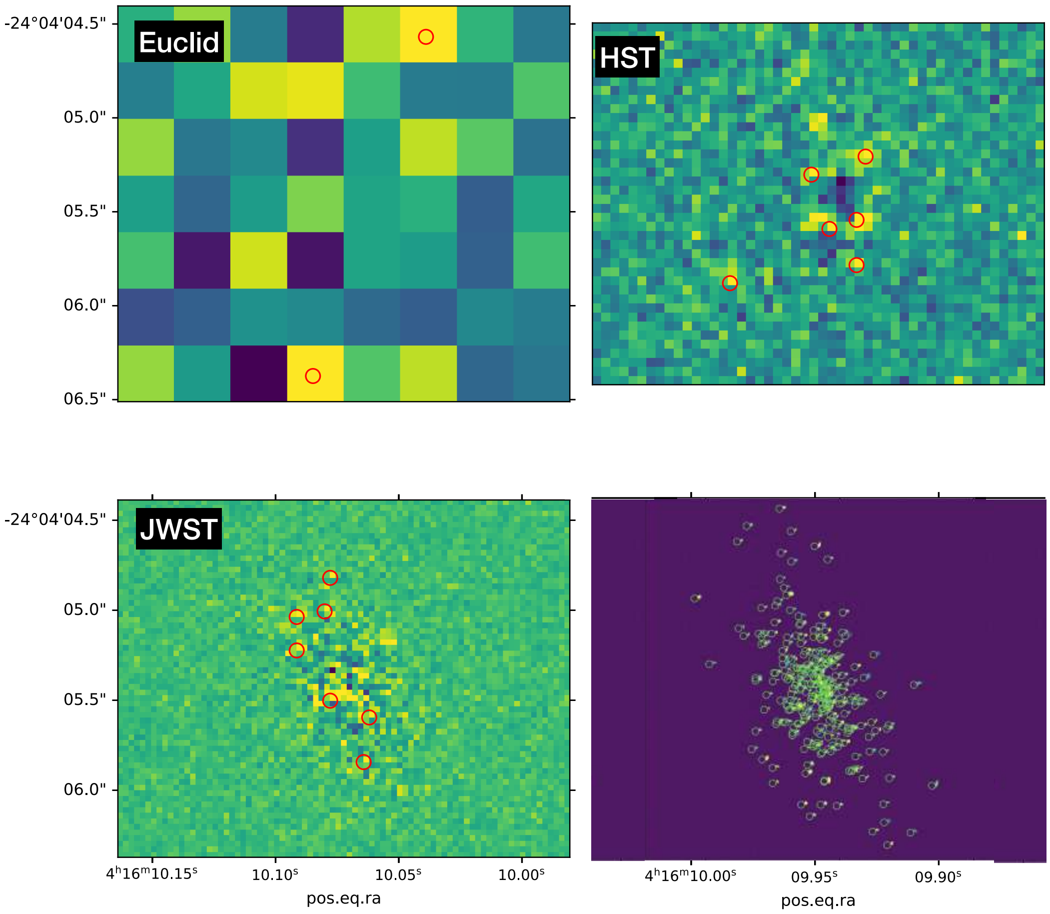

Figure 4.15: The residuals of the unlensed source corresponding to the arc in Figure 4.13, and a high-resolution image (0.005 arcsec/pxl) in the fourth panel. The red circles indicate the clumps detected by the three instruments over a threshold set to 0.8.

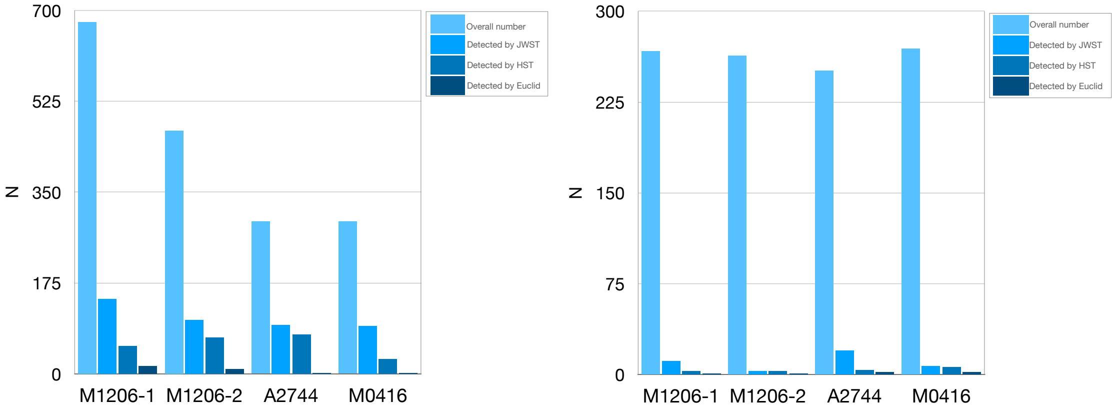

(a) **(b)**

Figure 4.16: Histograms showing the number of detected stellar clumps in the simulated Euclid, HST, and JWST images. The number of clumps detected in the lensed images or in the unlensed background sources are shown in panel (a) and (b), respectively.

4.2 SimCADO

The simulations generated in the previous Chapter can be used to test the performance of new generation instruments when detecting small substructures, such as stellar clumps with typical sizes of ~ 10 pc or less.

In this Section, we describe how our simulations can be ingested by another software, `SimCADO`, designed to simulate observations with specific instruments. In particular, we consider the E-ELT/MICADO (Section 2.3), which, thanks to the support from MORFEO and its single (SCAO) or multi-conjugate adaptive optics system (MCAO), is designed to work at the diffraction limit of the ELT. In particular, MICADO is supposed to reach a spatial resolution of 0.004 arcsec/pxl over a field-of-view of $50.5''$x$50.5''$ or, in a zoom mode, 0.0015 arcsec/pxl over a field-of-view of $19''$x$19''$. Regarding the two Adaptive Optic modules, SCAO will provide an exceptional correction over a small field-of-view (10 arcsec), using an extremely bright guide star (approximately of magnitude in band $V \leq 16$), placed within a few arcsec from the target. The MCAO mode, instead, will provide a moderate correction over a wider field-of-view (50 arcsec), relying on three guide stars with magnitude in band $H \leq 19$ placed in an annular region between 45 arcsec and 100 arcsec from the target. In order to obtain the best corrections, these guide stars should be placed at the vertexes of a triangle.

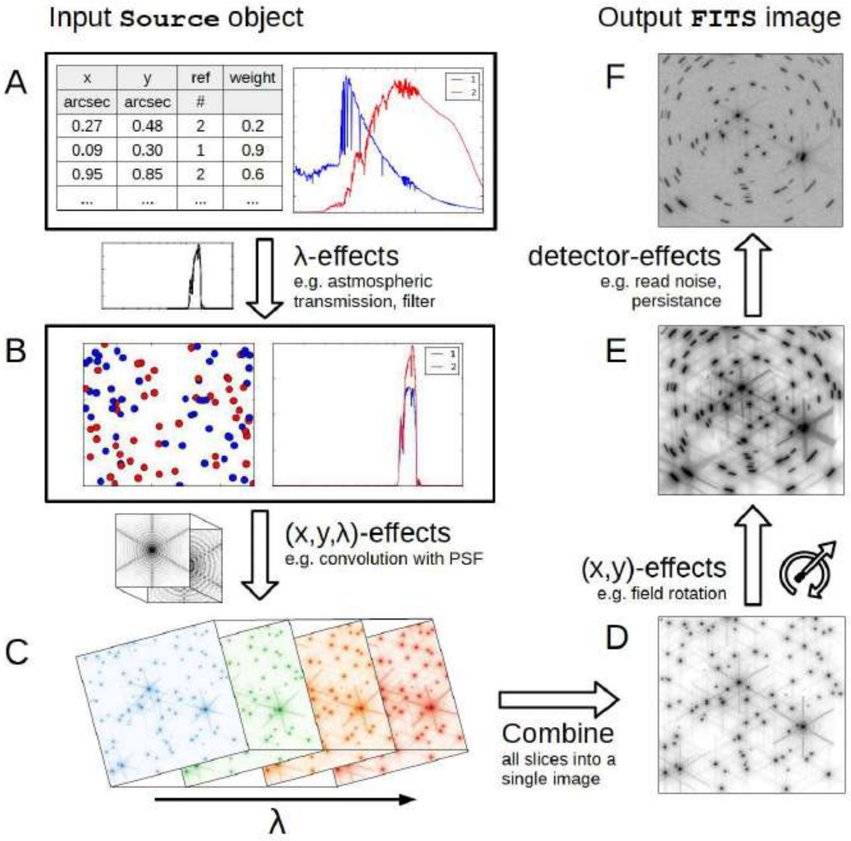

x	y	ref	weight
arcsec	arcsec	#	
0.27	0.48	2	0.2
0.09	0.30	1	0.9
0.95	0.85	2	0.6
...	...	...	...

Figure 4.17: Schematic representation of how `SimCADO` works (29).

The software `SimCADO`, developed by the A* consortium and the MICADO consortium (29), aims at simulating the effects of the atmosphere, E-ELT and MICADO on incoming photons. The tool is currently under active development. Referring to Figure 4.17, we can briefly describe the procedure behind `SimCADO`:

- We first create or load a `Source` object, which contains the spatial and spectral information referred to the source we are interested in simulating.
- All the optical elements which act on the wavelengths (i.e. filters, mirrors) are combined into a single effect and this latter is applied to the input spectrum, which is now expressed in the proper photo-electron count for the detector.
- The spectrum is divided into several bins, creating a sort of narrow-band filter images, which are, then, altered by some spatial effects, such as the atmospheric dispersion and the convolution with the PSF.
- All the slices are combined together in order to create a single image and the purely spatial effects (field rotation, telescope jitter) can be applied.
- The background and the mirror blackbody emissions are added to the image, assuming them both as spatially constant.
- Finally, the detector effects are taken into consideration: the image is resampled to the pixel scale of the detector chips and the noise (read-out noise, dead pixels, photon noise) is added.

Our simulation pipeline described in Chapter 3 can be combined with this software, since it can generate the images which are then adapted by `SimCADO` to the instrumental characteristics of MICADO. In particular, the images we produce with our simulator are completely noise free and highly resolved with a pixel scale of 0.001 arcsec/pxl. Since MICADO can cover a field-of-view of 50.5″x 50.5″ at most, while some of the gravitational arcs we simulated in the previous Chapter extend for more than 60 arcsec, we consider only those arcs which are less extended on the lens plane. For this reason, we consider the MICADO wide-field mode (0.004 arcsec/pxl over a field-of-view of 50.5″x50.5″) and the MCAO correction. Besides, the detector of MICADO is composed of 9 chips of 4096 x 4096 pixels and `SimCADO` gives the possibility to speed up simulations of small objects. In fact, in this case, we do not need to read out all the 9 chips of the detector, but, if the source is centred in the field-of-view, the middle chip is enough. In particular, `SimCADO` offers three options: we can use only a 1024x1024 pixels window at the centre of the middle chip, the whole middle chip, or the full field-of-view. We choose between them according to the size of the considered arc. Lastly, regarding the PSF, `SimCADO` can use both SCAO and MCAO PSF models. The MCAO models are built considering the three guide stars placed in their idealistic geometry, namely at the vertexes of a triangle, and simulating three different atmospheric conditions. In this Thesis, we consider the MCAO model build in average atmospheric conditions. At the moment, all the PSFs are assumed constant across the field, although they degrade moving away from the centre of the image.

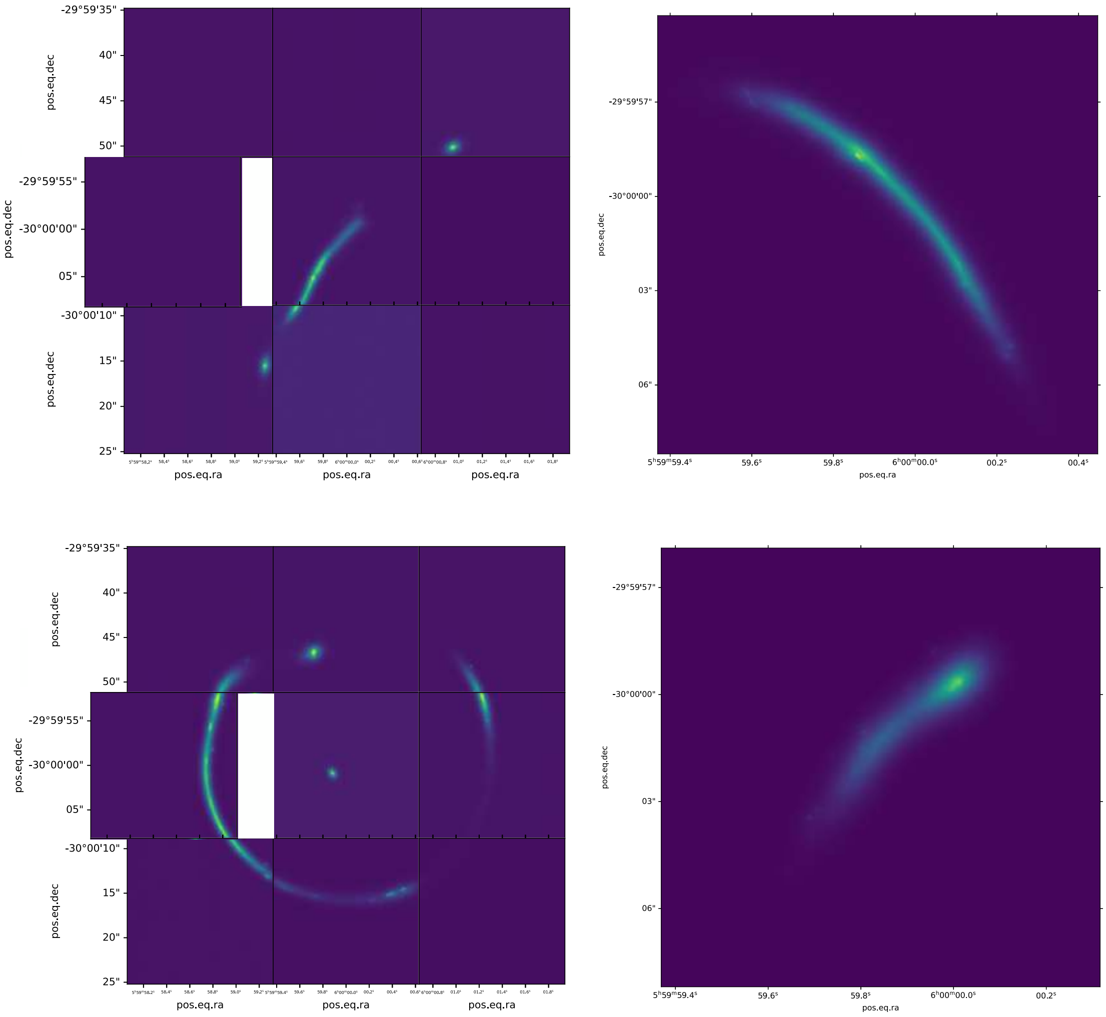

Figure 4.18: Simulations executed with `SimCADO` using the lensed sources E, N, K, and D of our simulations: the two images on the right are generated using only the middle chip of the detector, while those on the left using all the 9 chips. These images are simulated using the filter I and an overall exposure time of 500s.

In Figure 4.18 we show the four outputs obtained with `SimCADO`. In particular, we consider the lensed sources E, N, K, and D of our simulations, characterized by the SED model `Scd_B10.sed` of Figure 3.9. Since E and K cover wider regions of the sky plane, we have to use all the nine chips of the detector, while for N and D the middle chip is perfectly adequate. It is worth noting that the chips' color depends exclusively on the read-out noise, while the clearly visible gap between two chips is meant to hide eventual very bright objects. However, focusing on the gravitational arcs simulated with `SimCADO`, it is clear how the high resolution of MICADO enables a better detection of many substructures, even if, due to its extremely short pixel scale, their surface brightness is spread over a higher number of pixels. This is particularly evident in Figure 4.19, where we show the same zoom-in over a region of source D as seen by HST/ACS, JWST/NIRCAM and E-ELT/MICADO+MORFEO, compared with the high-resolution image.

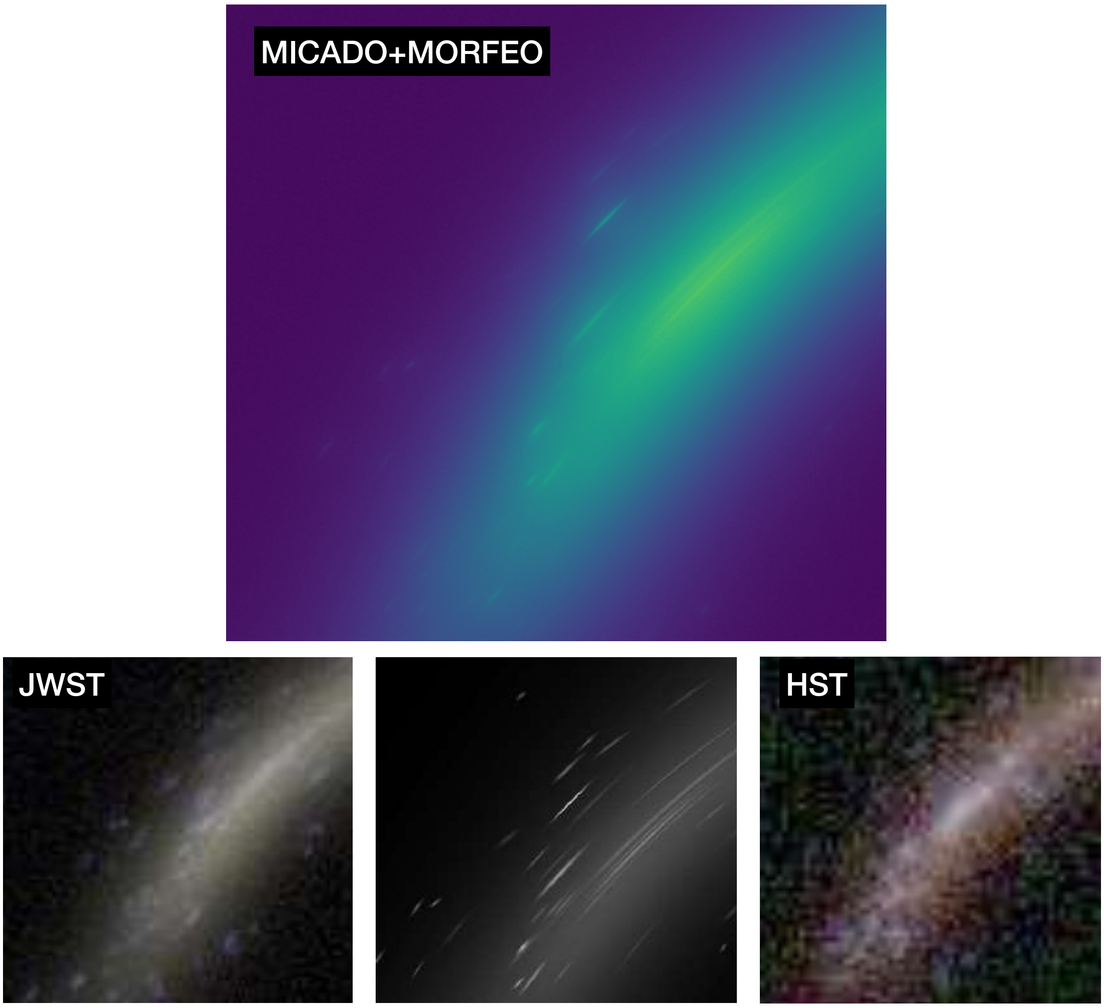

Figure 4.19: Comparison between E-ELT/MICADO+MORFEO, HST/ACS and JWST/NIRCAM. The figures show the same zoom-in over a region of lensed source D. The middle panel in the bottom line represents the high resolution image (0.001 arcsec/pxl).

Chapter 5

Summary and conclusions

In this Thesis, we implement and validate a python-based simulation pipeline designed to produce mock observations of clumpy galaxies gravitationally lensed by galaxy clusters. These simulations are particularly suitable to investigate how well the properties of stellar clumps in high-redshift sources ($z \gtrsim 2$) can be constrained using different instruments, particularly when lensing magnification by cosmic telescopes is at work. Studying these sources is essential to understand the mechanisms that drive galaxy formation and evolution in the early Universe. At present, the sub-kpc structure of such distant galaxies is only accessible with the aid of lensing magnification. Otherwise, even deep space-based or AO-aided ground-based observations do not provide high-enough spatial resolution to observe it. Given that JWST started its operations very recently, and considering the imminent launch of the ESA's mission Euclid, developing a tool that enables forecasting the capabilities of these instruments to observe the smallest details of lensed high-redshift galaxies is timely. In addition, it is interesting to compare these capabilities to those of instruments that are or were used for this kind of study in the past, for example, the HST, or that will be available a bit ahead in the future, such as the ESO's ELT with its MCAO supported imaging instrument MICADO.

The first part of our pipeline is devoted to modeling analytically the clumpy galaxies. These sources are described as a combination of multiple luminous components, namely the host galaxy and the stellar clumps. Each of them is modeled using an elliptical Sérsic surface brightness profile, whose parameters are set individually for the host and for the clumps. In the simulations shown in this Thesis, the host galaxies have exponential disks with Sérsic index $n = 1$, but this parameter can be easily changed. Instead, the clumps are described by a more sophisticated model that includes the following ingredients:

- we assume that the amount of flux in clumps is a fixed fraction of the total galaxy flux. This fraction depends on the morphological type of the host galaxy. For late-type sources, we assume that a fraction $Q = 0.2$ of the host total flux goes into stellar clumps;
- we assign each clump a luminosity, drawing from a generalized Schechter function (eq. 3.1.4), whose parameters can also be customized;

- the clumps' positions inside the host galaxy are determined assuming their spatial distribution follows the surface brightness profile of the galaxy itself;
- to model the clump sizes, we use a relation between the effective radii and the stellar masses of clumps in galaxies measured in the Local Universe. The stellar masses are derived from the clump luminosity assuming a mass-to-light ratio. In the simulations shown in this Thesis, we use a constant mass-to-light ratio $M/L \sim 1$;
- we model the clumps' surface brightness using a Sérsic index $n = 0.5$;
- each clump has an elliptical shape with an axis ratio uniformly distributed in the range $[0.3, 1]$ and a random orientation.

In addition, we enable to the creation of multi-band simulations of the sources by assigning to the host and clumps spectral energy distributions corresponding to sources of different colors and ages.

The second part of our simulation pipeline is a ray-tracing component that enables the inclusion of lensing effects. We focus in particular on the strong lensing effects that can be observed in the central regions of galaxy clusters. To model these effects, we use deflection angles obtained from the strong lensing modeling of five galaxy clusters recently observed in the framework of some programs carried out by HST and JWST. They are the clusters MACS J1206.2-0847, MACS J0416.1-2403, Abell S1063, PSZ1G311.65-18.48, and Abell 2744. To produce large magnifications and distortions, the sources are placed near the caustics of the lens.

The third and last part of our simulation pipeline is a set of functions that allow us to simulate observations with several telescopes. These functions sample the sources at the instrument resolution, add the instrument PSF, compute the background level for a given observational set-up, and finally add photon noise, before saving the images to `.fits` files.

We produce a gallery of simulated observations of three sources per cluster (i.e., we simulate 15 sources in total). For each of them, we simulate multi-band observations with HST/ACS and JWST/NIRCam. We further simulate VIS imaging in *riz* band with Euclid. Visually inspecting them, these simulations let us appreciate the wealth of details that JWST can capture in the clumpy galaxies, which largely improves the capabilities of HST. As expected, due to its relatively coarse spatial resolution, Euclid is not the ideal instrument to observe and characterize the stellar clumps in high-redshift sources.

Nevertheless, it is worth remembering that Euclid will deliver observations of nearly half of all extra-galactic sky. As shown by (8) and (9), Euclid is expected to find of order $\sim 5000 - 10000$ giant gravitational arcs in the wide survey. All these highly magnified sources will be potential targets for follow-up observations with instruments with adequate spatial resolution.

Relevant to this latest point, we also simulate observations with a fourth instrument, E-ELT/MICADO, combining the capabilities of our simulation pipeline with the "official" instrument simulator `SimCADO`, developed by the MICADO team. Indeed, these simulations show that ELT will be the ideal instrument to follow up the lensed sources that Euclid will find and to study their stellar clumps.

In the fourth chapter of this Thesis, we apply our simulation pipeline to test and validate some functionalities of a new software, dubbed `GravityFM`. This code implements the so-called "forward modeling" approach to model the surface brightness distribution of lensed sources. `GravityFM` aims at figuring out the shape of the posterior distributions of those parameters which describe the surface brightness profile of the source, accounting for the lensing distortions. It performs two different processes: the Maximum Likelihood Estimation, performed as a PSO thanks to the python toolkit `pySwarms`, and the Likelihood Sampling, executed through the python module `emcee`. The functionalities of this code will be presented, together with the testing done in this Thesis, in a forthcoming paper by Bergamini et al.

We aimed at understanding how many substructures can be detected in the images simulated with different instruments. We use `GravityFM` to fit only the host parameters, ignoring the stellar clumps. Subtracting the lensed model of the host generated by `GravityFM` from the original image, we obtain a residual map where the stellar clumps can be better identified because of their higher contrast. To automatize the detection, we use a thresholding procedure. The threshold is defined basing on subjective criteria, that have to be adapted to the specific sources. However, a trend emerges: in the lensed images, Euclid detects only 1-2% of the overall number of stellar clumps, while HST hovers at 10-15% and JWST reaches 20-30%.

These percentages result from a preliminary analysis that we plan to extend in the near future. For example, we will use these simulations to quantify how the number of detections depends on several clump properties, such as their mass, luminosity, and size, and what fraction of clumps detected with the different instruments are not single clumps, but unresolved combinations of multiple clumps.

Furthermore, `GravityFM` can be used to fit simultaneously the properties of host and clumps. Fitting the clumps' surface brightness would enable us to measure additional properties, such as the clumps' sizes in the source plane. Our simulations are extremely important to validate the capabilities of `GravityFM` to perform this kind of analysis on real data. Furthermore, the pipeline we have developed will be a valuable tool to support the development of science cases for the next generation of instruments that will be used to investigate in-depth the properties of strong gravitational lenses.

Bibliography

[1] Adamo, A., et al., 2020. *Star cluster formation in the most extreme environments: insights from the HiPEEC survey. MNRAS*, 499(3):3267. doi:10.1093/mnras/staa2380.

[2] Avila, R. J., 2017. *Advanced Camera for Surveys Instrument Handbook for Cycle 25 v. 16.0.* In *Advanced Camera for Surveys HST Instrument Handbook*, page 16.

[3] Bayliss, M. B., et al., 2011. *The Redshift Distribution of Giant Arcs in the Sloan Giant Arcs Survey. ApJL*, 727(1):L26. doi:10.1088/2041-8205/727/1/L26.

[4] Benítez, N., et al., 2004. *Faint Galaxies in Deep Advanced Camera for Surveys Observations. ApJS*, 150(1):1. doi:10.1086/380120.

[5] Bergamini, P., et al., 2019. *Enhanced cluster lensing models with measured galaxy kinematics. A&A*, 631:A130. doi:10.1051/0004-6361/201935974.

[6] Bergamini, P., et al., 2021. *A new high-precision strong lensing model of the galaxy cluster MACS J0416.1-2403. Robust characterization of the cluster mass distribution from VLT/MUSE deep observations. A&A*, 645:A140. doi:10.1051/0004-6361/202039564.

[7] Bergamini, P., et al., 2023. *New high-precision strong lensing modeling of Abell 2744. Preparing for JWST observations. A&A*, 670:A60. doi:10.1051/0004-6361/202244575.

[8] Boldrin, M., Giocoli, C., Meneghetti, M., and Moscardini, L., 2012. *Predicting the number of giant arcs expected in the next-generation wide-field surveys from space. MNRAS*, 427(4):3134. doi:10.1111/j.1365-2966.2012.22120.x.

[9] Boldrin, M., et al., 2016. *Cosmology through arc statistics I: sensitivity to* Ω_m *and* σ_8. *MNRAS*, 457(3):2738. doi:10.1093/mnras/stw140.

[10] Brown, G. and Gnedin, O. Y., 2021. *Radii of young star clusters in nearby galaxies. MNRAS*, 508(4):5935. doi:10.1093/mnras/stab2907.

[11] Calura, F., et al., 2022. *Sub-parsec resolution cosmological simulations of star-forming clumps at high redshift with feedback of individual stars. MNRAS*, 516(4):5914. doi:10.1093/mnras/stac2387.

[12] Caminha, G. B., et al., 2022. *First JWST observations of a gravitational lens. Mass model from new multiple images with near-infrared observations of SMACS J0723.3−7327. A&A*, 666:L9. doi:10.1051/0004-6361/202244517.

[13] Cava, A., et al., 2018. *The nature of giant clumps in distant galaxies probed by the anatomy of the cosmic snake. Nature Astronomy*, 2:76. doi:10.1038/s41550-017-0295-x.

[14] Cava, A., et al., 2018. *The nature of giant clumps in distant galaxies probed by the anatomy of the cosmic snake. Nature Astronomy*, 2:76. doi:10.1038/s41550-017-0295-x.

[15] Cimatti, A., Fraternali, F., and Nipoti, C., 2019. *Introduction to Galaxy Formation and Evolution. From Primordial Gas to Present-Day Galaxies. arXiv e-prints*, arXiv:1912.06216. doi:10.48550/arXiv.1912.06216.

[16] Coe, D., et al., 2013. *CLASH: Three Strongly Lensed Images of a Candidate* $z \approx 11$ *Galaxy. ApJ*, 762(1):32. doi:10.1088/0004-637X/762/1/32.

[17] Coe, D., et al., 2019. *RELICS: Reionization Lensing Cluster Survey. ApJ*, 884(1):85. doi:10.3847/1538-4357/ab412b.

[18] Euclid Collaboration, et al., 2022. *Euclid preparation. I. The Euclid Wide Survey. A&A*, 662:A112. doi:10.1051/0004-6361/202141938.

[19] Giocoli, C., Tormen, G., Sheth, R. K., and van den Bosch, F. C., 2010. *The substructure hierarchy in dark matter haloes. MNRAS*, 404(1):502. doi:10.1111/j.1365-2966.2010.16311.x.

[20] Goodman, J. and Weare, J., 2010. *Ensemble samplers with affine invariance. Communications in Applied Mathematics and Computational Science*, 5(1):65. doi:10.2140/camcos.2010.5.65.

[21] Guy, L. P., et al., 2022. *Rubin-Euclid Derived Data Products: Initial Recommendations.* In *Zenodo id. 5836022*, volume 58, page 5836022. doi:10.5281/zenodo.5836022.

[22] Jullo, E. and Kneib, J. P., 2009. *Multiscale cluster lens mass mapping - I. Strong lensing modelling. MNRAS*, 395(3):1319. doi:10.1111/j.1365-2966.2009.14654.x.

[23] Jullo, E., et al., 2007. *A Bayesian approach to strong lensing modelling of galaxy clusters. New Journal of Physics*, 9(12):447. doi:10.1088/1367-2630/9/12/447.

[24] Kennedy, J. and Eberhart, R., 1995. *Particle swarm optimization.* In *Proceedings of ICNN'95 - International Conference on Neural Networks*, volume 4, pages 1942–1948 vol.4. doi:10.1109/ICNN.1995.488968.

[25] Kneib, J. P., Ellis, R. S., Smail, I., Couch, W. J., and Sharples, R. M., 1996. *Hubble Space Telescope Observations of the Lensing Cluster Abell 2218. ApJ*, 471:643. doi:10.1086/177995.

[26] Kneib, J.-P. and Natarajan, P., 2011. *Cluster lenses. Astron. Astrophys. Rev.*, 19:47. doi:10.1007/s00159-011-0047-3.

[27] Krist, J. E., Hook, R. N., and Stoehr, F., 2011. *20 years of Hubble Space Telescope optical modeling using Tiny Tim.* In M. A. Kahan, editor, *Optical Modeling and Performance Predictions V*, volume 8127 of *Society of Photo-Optical Instrumentation Engineers (SPIE) Conference Series*, page 81270J. doi:10.1117/12.892762.

[28] Leonard, A., Goldberg, D. M., Haaga, J. L., and Massey, R., 2007. *Gravitational Shear, Flexion, and Strong Lensing in Abell 1689. ApJ*, 666(1):51. doi:10.1086/520109.

[29] Leschinski, K., et al., 2016. *SimCADO: an instrument data simulator package for MICADO at the E-ELT.* In G. Z. Angeli and P. Dierickx, editors, *Modeling, Systems Engineering, and Project Management for Astronomy VI*, volume 9911 of *Society of Photo-Optical Instrumentation Engineers (SPIE) Conference Series*, page 991124. doi:10.1117/12.2232483.

[30] Lotz, J. M., et al., 2017. *The Frontier Fields: Survey Design and Initial Results. ApJ*, 837(1):97. doi:10.3847/1538-4357/837/1/97.

[31] Madau, P. and Dickinson, M., 2014. *Cosmic Star-Formation History. ARAA*, 52:415. doi: 10.1146/annurev-astro-081811-125615.

[32] Mahler, G., et al., 2022. *Precision modeling of JWST's first cluster lens SMACSJ0723.3-7327. arXiv e-prints*, arXiv:2207.07101. doi:10.48550/arXiv.2207.07101.

[33] McDermid, R. M., et al., 2020. *Phase A Science Case for MAVIS – The Multi-conjugate Adaptive-optics Visible Imager-Spectrograph for the VLT Adaptive Optics Facility. arXiv e-prints*, arXiv:2009.09242. doi:10.48550/arXiv.2009.09242.

[34] Meneghetti, M., 2021. *Introduction to Gravitational Lensing; With Python Examples*, volume 956. doi:10.1007/978-3-030-73582-1.

[35] Meneghetti, M., et al., 2008. *Realistic simulations of gravitational lensing by galaxy clusters: extracting arc parameters from mock DUNE images. A&A*, 482(2):403. doi:10.1051/0004-6361: 20079119.

[36] Meštrić, U., et al., 2022. *Exploring the physical properties of lensed star-forming clumps at 2 $\lesssim z \lesssim$ 6. MNRAS*, 516(3):3532. doi:10.1093/mnras/stac2309.

[37] Narayan, R. and Bartelmann, M., 1996. *Lectures on Gravitational Lensing. arXiv e-prints*, astro-ph/9606001. doi:10.48550/arXiv.astro-ph/9606001.

[38] Oesch, P. A., et al., 2016. *A Remarkably Luminous Galaxy at z=11.1 Measured with Hubble Space Telescope Grism Spectroscopy. ApJ*, 819(2):129. doi:10.3847/0004-637X/819/2/129.

[39] Pascale, M., et al., 2022. *Unscrambling the Lensed Galaxies in JWST Images behind SMACS 0723. ApJL*, 938(1):L6. doi:10.3847/2041-8213/ac9316.

[40] Pignataro, G. V., et al., 2021. *A strong lensing model of the galaxy cluster PSZ1 G311.65-18.48. A&A*, 655:A81. doi:10.1051/0004-6361/202141586.

[41] Plazas, A. A., Meneghetti, M., Maturi, M., and Rhodes, J., 2019. *Image simulations for gravitational lensing with SKYLENS. MNRAS*, 482(2):2823. doi:10.1093/mnras/sty2737.

[42] Postman, M., et al., 2012. *The Cluster Lensing and Supernova Survey with Hubble: An Overview. ApJS*, 199(2):25. doi:10.1088/0067-0049/199/2/25.

[43] Rivera-Thorsen, T. E., et al., 2019. *Gravitational lensing reveals ionizing ultraviolet photons escaping from a distant galaxy. Science*, 366(6466):738. doi:10.1126/science.aaw0978.

[44] Rivera-Thorsen, T. E., et al., 2019. *Gravitational lensing reveals ionizing ultraviolet photons escaping from a distant galaxy. Science*, 366(6466):738. doi:10.1126/science.aaw0978.

[45] Rosati, P., et al., 2014. *CLASH-VLT: A VIMOS Large Programme to Map the Dark Matter Mass Distribution in Galaxy Clusters and Probe Distant Lensed Galaxies. The Messenger*, 158:48.

[46] Sahu, K., 2021. *WFC3 Data Handbook v. 5.* In *WFC3 Data Handbook v. 5*, volume 5, page 5.

[47] Schechter, P., 1976. *An analytic expression for the luminosity function for galaxies. ApJ*, 203:297. doi:10.1086/154079.

[48] Shi, Y. and Eberhart, R., 1998. *A modified particle swarm optimizer.* In *1998 IEEE International Conference on Evolutionary Computation Proceedings. IEEE World Congress on Computational Intelligence (Cat. No.98TH8360)*, pages 69–73. doi:10.1109/ICEC.1998.699146.

[49] Vanzella, E., et al., 2017. *Paving the way for the JWST: witnessing globular cluster formation at $z > 3$. MNRAS*, 467(4):4304. doi:10.1093/mnras/stx351.

[50] Vanzella, E., et al., 2022. *Early Results from GLASS-JWST. VII. Evidence for Lensed, Gravitationally Bound Protoglobular Clusters at $z = 4$ in the Hubble Frontier Field A2744. ApJL*, 940(2):L53. doi:10.3847/2041-8213/ac8c2d.

[51] Zheng, W., et al., 2012. *A magnified young galaxy from about 500 million years after the Big Bang. Nature*, 489(7416):406. doi:10.1038/nature11446.